Optimization of Tension Leg Buoy with regards to Stabilization Failure

Master's thesis in Structural and Civil Engineering

Department of Civil Engineering
AALBORG UNIVERSITY ESBJERG
Esbjerg, Denmark 2016

AALBORG UNIVERSITY
DENMARK

Master's thesis 2016

Optimization of Tension Leg Buoy Wind Turbine with regards to Stabilization Failure

Master's Thesis Within Structural Engineering and Civil Engineering

Esbjerg, 09/06/2016

(Jesper Trolle)

(Frederik F. Hornbak)

Department of Civil Engineering
Division of Structures, Materials and Geotechnics
Aalborg University Esbjerg
Esbjerg, Denmark 2016

Written by
Jesper Trolle & Frederik F. Hornbak, 2016.

Project Title: Optimization of Tension Leg Buoy with regards to Stabilization Failure
Project Period: 01/09/2015 - 09/06/2016
Supervisor: Lars Damkilde, Professor of Structural Mechanics, Ph.D.
Morten E. Nielsen, Reseach Assistent, M.Sc.

Master's Thesis 2016
Department of Civil Engineering
Division of Structures, Materials and Geotechnics
Aalborg University Esbjerg
DK-6700 Esbjerg

Typeset in LaTeX
Esbjerg, Denmark 2016

Abstract

This thesis is dedicated to further the understanding of Tension Leg Buoys undergoing stabilization failure in the form of a mooring line fracture. To this end, a numerical Finite Element Method based program, utilizing corotational beams and a nonlinear Newmark time integration, in combination with steam function wave theory and the relative version of the Morison equation is applied. The numerical program is validated with experimental results for the Tension Leg Buoy Basic design, and through the Froude scaling method, a full size model is determined. This full size model is used in stabilization failure analyzes, and a new and more stable design of the Tension Leg Buoy Basic is found.

Keywords: *Floating Wind Turbines, Tension Leg Buoy, Wave Theory, Load Determination, Morison, Real Flow.*

Resume

Denne afhandling er dedikeret til at fremme forståelsen for Træk Bens Bøjer udsat for stabilitets sammenbrud if form af fortøjningsbrud. For at opnå dette, er et Finite Element Method baseret program, som udnytter corotational bjælke teori og en ikke lineær Newmark tidsintegration, i kombination med strømfunktions bølgeteori og den relative version af Morisons ligning benyttet. Det numeriske program er valideret med eksperimentelle forsøgsresultater for Træk Bens Bøje Basis design, og gennem Froude skalleringsmetode findes en fuld største model. Denne fuld størrelse model er brugt i stabilitets sammenbruds analyser, og et nyt og mere stabilt design for Træk Bens Bøje Basis er fundet.

Nøgleord: *Flydende Vind Turbiner, Træk Bens Bøje, Bølge Teori, Last Fastlæggelse, Morison, Realistisk Flow.*

Preface

This Master's thesis has been carried out in the period from the 1 September 2015 to the 9 June 2016 at the department of Civil- and Structural Engineering at Aalborg University Esbjerg. The thesis is written to fulfill the requirements for completing the degree of Master's of Science within the area of Structural Engineering.

The thesis investigates stabilization failure and optimization of a Tension Leg Buoy Wind Turbine foundation. For the purpose of including structural- and hydrodynamic non-linearities, all simulations are conducted by use of the developed in-house hydro-elastic time-domain routine at Aalborg University. Through the thesis, the routine is verified against Ocean Command in ANSYS Inc., as well as a comparison with available experimental results, have guarantied the routines ability to reproduce realistic results. As a result the dynamic response is upscaled and used in the investigation of stabilization failure of the Tension Leg Buoy Wind Turbine foundation simulations.

The purpose of the thesis is to gain better insight into floating offshore structures, in particular Tension Leg Buoy Wind Turbine foundations and through the following investigation, contribute to the last decades research within area.

Acknowledgements

As the authors of this scientific Master's thesis, we would like to thank our two supervisors, Prof. Lars Damkilde and Research Assistant Morten E. Nielsen, for all of their guidance throughout the project period.

In an effort to contribute to the further development and validation of offshore wind turbine simulation tools, A. Myhr and T. Nygaard from the University of Life Sciences and the Institute for Energy Technology respectively, have published their experimental work and results of Tension Leg Buoy wind turbines. We appreciate their research and their willingness of publishing achieved results. They have been helpful to underline the considered in-house hydro-elastic routines ability to reproduce realistic results of Tension Leg Wind Turbines.

Finally we have been grateful for help, guidance and encouragement from family and friends during the last year.

Frederik F. Hornbak
Jesper Trolle
Date: 9/6-2016

Reading Guide

The report begins with an introduction to the thesis, which describes the argumentation of utilizing floating offshore wind turbines in the future with regards to the North Sea, followed by a general explanation of the main stabilization principles. The project aim and scope is lastly in the introduction considered.

Chapter 2 is a continuation of the introduction, considering a more detailed specification of the considered problem, as well as previuos work is discussed. Furthermore, a geometric description of the tension leg buoy is given and an analytical evaluation of hydrostatic consequences of pontential mooring line fracture is considered.

The theoretical background for the methods utilized in the software "Simulation Of Floating In Action", started in chapter 3, by describing the wave theories and continued to chapter 4 and 5 considering the hydrodynamic effects of slender frame structures and the structural beam formulation respectivily.

In chapter 6, experimental models are used in the verification of the simulation tool. The results are through chapter 7 upscaled to full size for the purpose of simulationg mooring line fracture analyzes, which is conducted in chapter 8. Finally, a discussion on how the project and the simulated results could be improved is found and followed by a conclusion of all the results and overservation obtained through the thesis.

Along with the thesis an appendix is included in which respective validations and supplying information is stated. Files generated in MATLAB, ANSYS Inc. and Excel are contained in the attached CD.

The litterature used in the report is shown in the bibliography, while the references is denoted with [1].

Nomenclature

Greek Symbols

α	Mass Proportional Damping	$[s^{-1}]$
β	Stiffness Proportional Damping	$[s]$
η	Elevation Height	$[m]$
γ	Peak Enhancement Factor	$[-]$
ω	Oscillation frequency	$[Hz]$
ϕ	Velocity Potential	$[-]$
ψ	Stream Function	$[-]$
ρ	Water Density	$[\frac{kg}{m^3}]$

Latin Symbols

$[C]$	Linear Damping Matrix	$[-]$
$[K]$	Structural Stiffness Matrix	$[-]$
$[K_d]$	Deformation Stiffness Matrix	$[-]$
$[K_{e,R}]$	Rotated Element Stiffness Matrix	$[-]$
$[K_e]$	Element Stiffness Matrix	$[-]$
$[K_r]$	Rotation Stiffness Matrix	$[-]$
$[M]$	Structural Mass Matrix	$[-]$
$[N]$	Shape Function	$[-]$
$[R]$	Element Stiffness Matrix	$[-]$
$[R_e]$	Rotation Matrix	$[-]$
$[S]$	Transformation Matrix	$[-]$
A_f	Fluid Acceleration	$[m]$
A_f	Horizontal fluid velocity	$[m]$
A_f	Horizontal structural velocity	$[m]$
A_s	Structural Acceleration	$[m]$
c	Propagation Velocity	$[\frac{m}{s}]$
C_A	Added Mass Coefficient	$[-]$
c_a	Absolute Propagation Velocity	$[\frac{m}{s}]$
C_D	Drag Coefficient	$[-]$
C_M	Inertia Coefficient	$[-]$

c_r	Relative Propagation Velocity	$[\frac{m}{s}]$
f	Frequency	$[Hz]$
$F_{a,bottom}$	Added mass Force Contribution end cap	$[-]$
$F_{a,con}$	Added mass Force Contribution conical section	$[-]$
F_a	Added mass Force Contribution	$[-]$
F_B	Gravity Force	$[N]$
F_G	Gravity Force	$[N]$
$F_{m,r}$	Relative Morison Force	$[N]$
g	Gravitational Acceleration	$[\frac{m}{s^2}]$
H	Wave Height	$[m]$
h	Water Depth	$[m]$
J	Jacobian Matrix	$[-]$
k	Wave Number	$[-]$
L	Wave Length	$[m]$
N	Stream Function Order	$[-]$
Q	Volumetric Discharge	$[\frac{m^3}{s}]$
R	Bernuilli's Constant	$[-]$
r_{bot}	Radius TLB B bottom section	$[m]$
r_{top}	Radius TLB B top section	$[m]$
T	Wave Period	$[s]$

Mathematical Symbols

[]	Square Matrix or Rectangular Matrix	$[-]$
{}	Row Vector	$[-]$

Acronyms

ALS Accidental Limit State.
API American Petroleum Institute.

COB Center of Buoyancy.
COG Center of Gravity.

DNV Det Norske Veritas.
DOF Degree Of Freedom.

FEM Finite Element Method.
FFT Fast Fourier Transform.
FLS Fatigue Limit State.
FOWT Floating Offshore Wind Turbine.

KC Keulegan Carpenter Number.
KC Reynolds Number.

MIT Massachusetts Institute of Technology.
MSL Mean Sea Level.

NREL National Renewable Energy Laboratory.

SLS Serviceability Limit State.
SOFIA Simulation Of Floaters In Action.

TLB Tension Leg Buoy.
TLP Tension Leg Platform.

ULS Ultimate Limit State.

Contents

List of Figures

List of Tables

1
Introduction

One of today's major challenges is to accommodate the energy demand of the future in a renewable way in order to become more independent of fossil fuels. As a result, the utilization of wind turbines is increasingly becoming more common, in particular offshore wind turbines. Offshore wind turbines have the advantage that they are exposed to higher and more constant winds, as well as a decrease in human noise discomfort.

The total energy requirement of Europe is approximately 3000 TWh each year, a requirement the wind turbine industry currently can provide with 30% of the total available wind energy resources. However 70% of these resources are placed in the sea, where the water depths are more than 50m [52].

Current offshore wind turbines are located in regions with water depths lower than 50m, using bottom fixed foundation principles, such as the well-known monopile and the jacket foundation. The most cost efficient offshore wind turbine design is at the moment using a monopile. This design becomes increasingly more complicated and not feasible at regions with depths deeper than 50m. A more appropriate solution for larger depths is jacket structures, which may be utilized up to depths of 50-80m. The disadvantage is, that they are 3-4 times more expensive per unit weight than monopiles, due to their complex design and installation method [52]. For depths larger than 50m, different Floating Offshore Wind Turbine (FOWT) concepts have been proposed, such as the Semi-submersible Platform, the Spar Buoy, the Tension Leg Platform (TLP) and the Tension Leg Buoy (TLB).

Figure 1.1: TLB concept [41]

The extent of FOWT are widely limited due to the cost, and by the fact that the technology is relatively new and unproven. However, as result of today's further development it is believed, that the cost will decrease even faster than those for bottom fixed foundations. The reason is, that while jackets and monopiles require high precision and low tolerances, as well as advanced jack-up vessels during the installation process, FOWT can become standardized on a turbine or wind park specific level. Subsequently the transportation and installation can be conducted by tug boats, which will increase the weather window for operations and decrease the expenses. The current cost of bottom fixed offshore wind energy is approximately 150 €/MWh, which is planned to be reduced to below 100 €/MWh for both bottom fixed and floating offshore wind turbines [52].

1.1 General concepts of floating wind turbines

The development of FOWT is basically based on three platform stabilization principles inspired from the Oil & Gas industry. The standard platform types are the spar buoy, semi-submersible platform, and the TLP.

Figure 1.2: Spar buoy (left, with catenary mooring lines), Semi-submersible (middle, with catenary mooring lines) and TLP. [52]

The spar buoy is based on ballast stability, and it is therefore required to have heavy ballast located below the platform, to ensure the FOWT will not capsize. The spar buoy is suitable for locations in deep water, due the required draft and its ability to withstand large waves. An example is the Statoil Hywind spar buoy, which has a substructure draft on 110m [48]. For water depths between 50-120m [37] the concepts of the semi-submersible platform and the TLP are preferred.

The semi-submersible concept is based on the principle of buoyancy and can be considered as a barge. Both ballast and buoyancy stabilized structures are self-stable and the mooring system is mainly to keep the platform stationary at the location. The principle of the last concept i.e. the TLP is that the stability is retained by tension in the mooring lines and is therefore classified as a non-self-stabilizing concept. In reality, the concepts are seen as hybrid concepts according to stability, for example when investigating the semi-submersible platform, it is not only stabilized by the buoyancy itself, but it is the

dominating stability factor [13]. Figure 1.3 will give an illustration of stability for hybrid floating concepts.

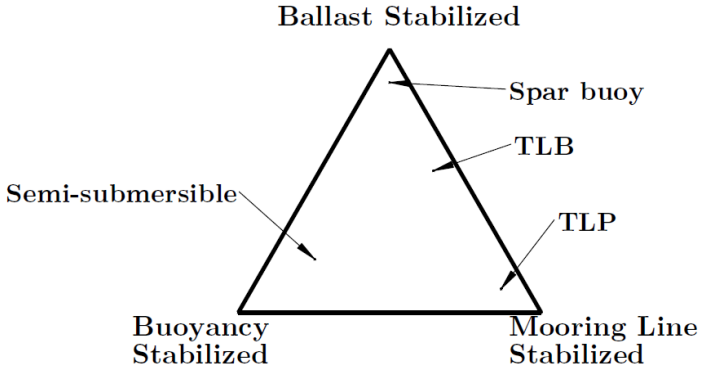

Figure 1.3: Categorization of stability principles (Inspired by [13])

1.2 Floating offshore wind turbines in the North Sea

The area for utilizing FOWT in the present thesis is in the North Sea. The sustainability of the TLB and the reason for addressing the mooring line stabilization principle, is in this section argumented for, with basis in the bathymetry of the North Sea, as well as the foundation costs. Figure 1.4 illustrates the bathymetry of the North Sea.

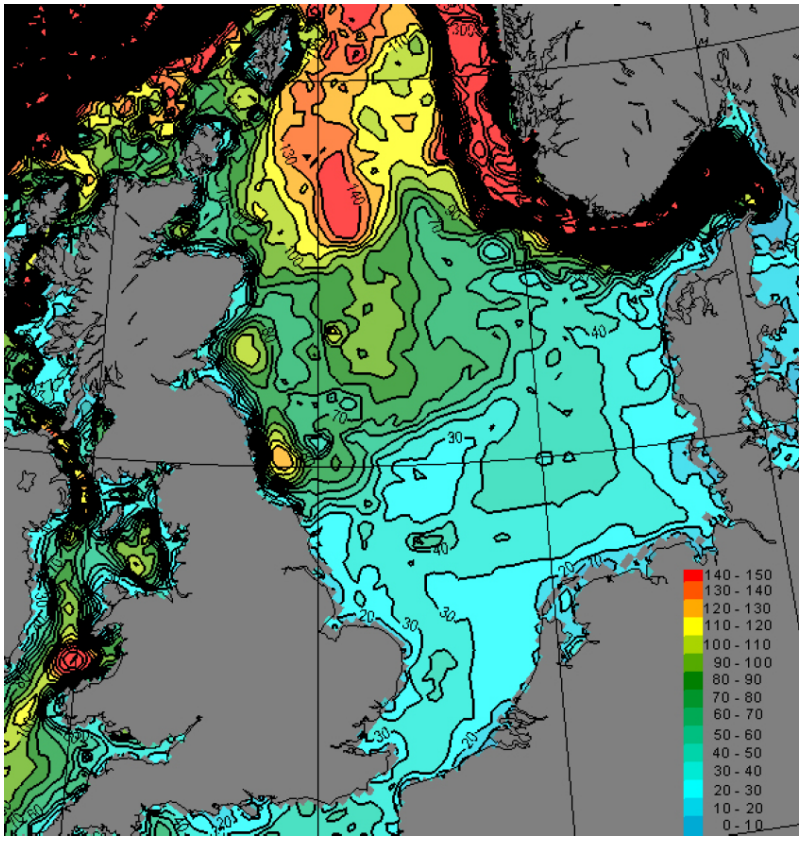

Figure 1.4: Bathymetry of the North Sea [21]

It is by an investigation of the bathymetry, illustrated above, seen that the area between Denmark and England in the southern part of the North Sea is dominated by water depths lower than 50m. However 66% of the depths in the North Sea is located between 50-220m [25]. From that fact, all previously mentioned stabilization concepts may be applicable in the North Sea, but it is clearly seen that FOWT concepts with a low draft i.e. the semi-submersible principle or the mooring line stabilized principles, have the largest potential in the area around Denmark. The spar buoy with a draft on 120m is therefore not further considered in the present thesis.

To argument for the remaining two stabilization principles, a study, where the concepts are cost evaluated by their levilized costs [37] and further compared to bottom fixed foundations, is taken in to consideration. Among these concepts are found, i.a., a semi-submersible platform (WindFloat), a TLP (TLPWT) and a TLB.

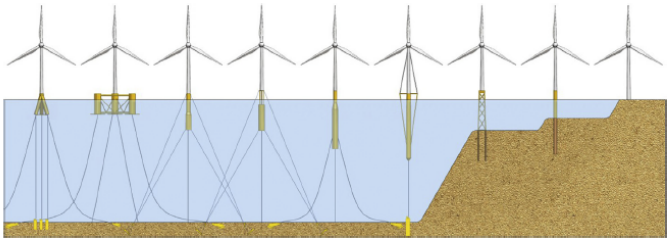

Figure 1.5: Floating and Fixed Wind Turbine Foundation concepts. From left to right: *TLWT*, *Windfloat*, *TLB B*, *TLB X3*, *Hywind*, *SWAY*, *Jacket*, *Monopile* [37].

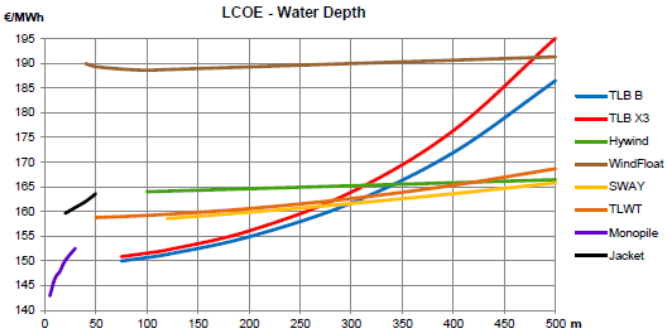

Figure 1.6: Levelized cost of energy for different FOWT concepts [37].

Figure 1.6 illustrates the levilized cost of FOWT with respect to the water depth, and it is as expected seen, that the mooring line stabilized concepts and the semi-submersible are those able to operate in the lowest water depths. Furthermore the analysis shows, that the semi-submersible platform is subjected to the absolute highest costs, due to the complex structure. In contradistinction to the semi-submersible, the tension leg principles ensures the lowest cost and in particular that TLB [37]. A levilized cost matching that for the monopile foundation on shallow water makes it an interesting concept to utilize in the North Sea.

Due to the economic feasibility of the TLB at lower water depths, it is assessed to be a sustainable concept at the location of the North Sea, and is therefore further considered.

1.3 Aim

The aim of the present thesis is to conduct analyzes designated to investigate, and potentially optimize, the TLB concept with regards to a stabilization failure consisting of a mooring line fracture. The study is performed by utilizing and further developing the in-house hydro-elastic routine "Simulation Of Floaters In Action (SOFIA)" computed by Aalborg University. SOFIA is programmed in the programming language MATLAB.

A result of SOFIA being newly developed, in terms of a beta-version, its reliability has not yet been validated numerically. Therefore a comprehensive numerical validation is conducted before any further stabilization failure simulations are evaluated. With experimentally conducted measurements for the considered TLB, in addition to optimizing the TLB concept with respect to a mooring line fracture, the present thesis is also focusing on ensuring the programs ability to reproduce experimental tests. In order to achieve reliable results in the mooring line fracture analysis, the numerically reproduced dynamic response from the experimental tests, are by use of Froude scaling up-scaled. Since correct up-scaling is paramount to achieve correct results, the scaling method and associated assumptions are as well evaluated.

1.4 Scope

To conduct the aforementioned numerical analyzes, SOFIA is utilized. The routine is based on an implicit nonlinear Newmark integration scheme associated with a Newton-Raphson solver. All simulations are conducted in the time-domain and is formulated by means of corotational beam elements.

The simulation of ocean loads is from the programmed beta version possible to simulate from both regular- and irregular time realizations of linear waves. In order to analyze higher order regular wave case scenarios, a stream function wave add-in is developed. The add-in enables a reliable description of all wave theories. Irregular wave realizations may still be simulated by use of the standard wave add-in, but is not further considered in this thesis. To convert particle kinematics generated from the wave add-in to ocean loads, a real flow simplification and the relative form of the Morison equation is used. This is together with buoyancy and gravity representing the forces exposed on the structure.

In order to establish a realistic model of the TLB, a method of modeling the mooring lines and the exerted pretension is further implemented in SOFIA.

The experimental results used to validate SOFIA is conducted by A. Myhr and T. Nygaard, and can be found in the publicly available paper [39]. All performed analyzes are based on conceptualized full size TLB, with the Academic Wind Turbine 5MW on top. In order to establish experiments with easily produced test models and simple implementation in numerical tools, a scaling factor 1:40 was chosen. Since the selection of the model materials becomes unrealistic if the models are up-scaled, an evaluation of the consequences is conducted.

Lastly a mooring line fracture is evaluated in an extreme wave scenario, and alternative ways of modeling are evaluated to better accommodate for the consequences of the mooring line fracture.

2

Design of floating tension leg wind turbines

The two previously presented TLB concepts, are due to their geometrical simplicity, economical beneficial. This accommodates one of the biggest goals for the development, within the offshore wind industry. Seen from the technical aspect, the TLB concept is stabilized completely by the mooring lines, which might result in fatal consequences if a mooring line fracture occurs. To reduce sources of errors, it is for the mooring line fracture analyzes decided to keep the focus on the TLB Basic (B).

Figure 2.1: Tension Leg Wind turbines; TLB B, TLB X3

The TLB B concept is developed by A. Myhr and T. Nygaard with the intend to both further develop the state of the art of FOWT technology, and contribute to the development of numerical simulation tools, by publishing experimental results of 1:40 down-scaled models. In collaboration with a Masters project [7], the experimental results was conducted at IFREMER's test facility in Brest, France.

As a part of the work conducted by A. Myhr and T. Nygaard, their experimental results was used in the validation of the simulation tool 3DFloat, which as SOFIA, is a Finite Element Method (FEM) program based on the method of corotational beam elements, and the real flow approximation Morison equation. However for wave modeling in 3DFloat linear wave theory is used, which is less accurate in finite depths [10].

In order to establish a better understanding of the development of FOWT, previous work is first considered within the topic. Afterwards the structural modeling method is presented, as well as the limit state and load is considered. Lastly in this chapter the stability consequences of a potential mooring line fracture is analytically evaluated .

2.1 Previous investigation of floating wind turbines

Design advantages and disadvantages for FOWT, are through the time widely discussed in scientific papers, Ph.D. and M.Sc. theses, based on numerical or experimental investigation. In particular numerical and parametric studies have been performed by Massachusetts Institute of Technology (MIT) in order to argue for the most suitable foundation design.

In this context it is important to mention an early state project, namely the M.Sc. thesis written by C. H. Tracy [49], covering a comprehensive parametric study. The purpose was to determine the optimal performance of a single column FOWT platform, with a 5MW academic wind turbine mounted on top of it. The simulations where performed in 6- and 10m sea state for different platform dimensions, mooring line systems (TLP and Catenary mooring lines) and water depths at 60m and 200m. The study give an insight in the Static/Dynamic tension of mooring lines, displacement, and nacelle acceleration for the different designs. These values where then used as criteria's in the parametric study [49]. Since Tracy used a frequency-domain analysis described in the study written by Wayman [51], it was not possible for him to include nonlinear effects e.g. nonlinear structural effects and nonlinear hydrodynamics. Therefore D. Martha [34] assessed the results to be unrealistic, and he performed a new study based on NREL's fully coupled time-domain aero-hydro-servo-elastic routine FAST. During the study, Matha discovered flaws in the mass matrix used by Tracy, and after a correction, he compared the time-domain analysis and the frequency-domain analysis, and concluded a significant difference in the results. Likewise he discovered that simulation of the mooring system required a lot of effort, in order to establish a realistic behavior [34].

Figure 2.2: Concept from C. Tracy M.Sc. Thesis [49]

Matha also performed a comparison between the TLP, semi-submersible, and spar buoy. Here he concluded that the semi-submersible platform was very susceptible to roll and pith motions, and therefore also exposed the largest loads on the wind turbine. Roll and pitch were larger for the spar buoy, compared to the TLP, but according to the yaw motion, the TLP was more sensitive [34].

The mentioned studies performed by C. H. Tracy, D. Matha and NREL, are all studies from the early state of the FOWT development. Looking forward until today, still a lot of academic investigation, in particular within simulations of the mooring systems, are performed.

In order to direct the literature study more specific in the direction of TLB, it is unavoidable to mention the "Taught Leg Bouy". In order to focus on a FOWT concept with a lower mass, P.D. Sclavounos, S. Lee and J. DiPietro came up with a new design based on previous research within FOWT and Oil and Gas at MIT [45]. Their work considered design, anchoring, and motion simulation of the TLB, in different sea states and water depths, ranging from 30 to a few hundred meters [45]. Furthermore, they did come up with an idea of how to transport the assembled TLB from the port to the site. The research performed by P.D. Sclavounos, S. Lee, and J. DiPietro is later continued by A. Myhr and T. Nygaard from the University of Life Sciences in Norway, with the purpose of reducing wave loads exposed to the TLB in rough weather conditions. Their investigation resulted in two different TLB designs, both with a reduced surface area around the water surface. The concepts are the aforementioned TLB B and TLB X3 [39].

2.1.1 Physical tests and sea trials

A relatively limited number of tests have been performed for FOWT and even fewer results are publicly available. An example is the Ph.D thesis written by C. Wehmeyer [53] at Aalborg University, which deals with model tests of an industry inspired TLP. Based on the observations from experiments [54], C. Wehmeyer develops a hybrid numerical model, where irregular nonlinear waves with an embedded stream function are implemented. During the experiments gyroscopic effects and elasticity of the blades has been of secondary interest, and a realistic wind turbine is not included due to a mismatch in the Reynold and Froude scaling [53]. By use of the numerical model, it is concluded that the implementation of the nonlinear irregular waves is a new engineering tool for developing FOWT. Likewise C. Wehmeyer discovered "Slack line" events in both his hybrid numerical model and the experiments. However they did occur more often in the experiments [53].

Another physical test that is important to mention, is the physical test performed by A. Myhr, T. Nygaard and J. Berg [39]. Their tests were performed with the aforementioned purpose of investigating the dynamical performance the of TLB concepts, as well as to contribute with publicly available results.

Like for the model test, only a very limited number of concepts have been tested in full scale, but at the moment some of the forerunners are the Statoil Hywind (Located in Norway [47]), WindFloat (Located in Portugal [23]) and Blue H (Located in Italy [9]).

2.2 Method of Consideration

Prediction of loads and dynamic responses of floating wind turbine structures implies, that the method of consideration is important in order to satisfy the balance between accuracy and computational resources. As a result, the present section covers a presentation of the method utilized in this project.

As aforementioned, SOFIA is utilized as simulation tool in this thesis, and is computed by use of the corotational beam formulation, similar to the method mentioned in 3DFloat software. The corotational beam formulation allows a structure to have arbitrarily large displacement and rotations on the global level, which makes it ideal in the simulation of floating structure. The theoretical background is described in chapter 5.

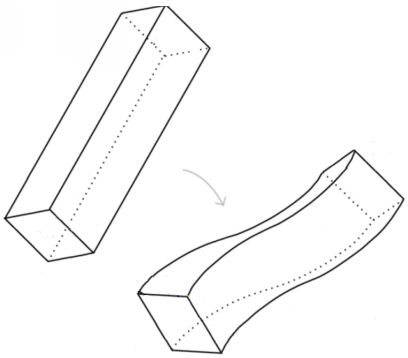

Figure 2.3: Illustration of the corotational beam principle with rigid body motion and local deformation [55]

Wave loads acting on the structure is determined through the stream function wave theory, which is able to describe all wave theories. This advantage makes the theory ideal to be used in the mooring line fracture studies, but will also increase the sustainability of SOFIA. A developed stream function wave add-in is therefore used in the estimation of particle kinematics, which in the process of calculating hydrodynamic loads, are inserted in the real flow approximation, Morison equation.

2.3 Conceptual tension leg buoy design

The TLB B is designed very close to the originally developed Taught Leg Buoy, but instead of having a constant cross section, the geometry is divided into two sections. The dimensions mentioned in the section are based on [39], but up-scaled to full-size by the scale factor 1:40.

The bottom section is designed with a diameter on 11.9m ($D1$) and a top section with a diameter on 6.4m ($D3$), both connected by a tapered section, as shown in figure 2.4. The reduced diameter on the top section is a result of the purpose of reducing the wave loads, since these are dependent on the surface area perpendicular to the propagation direction. As a result it is required to increase the volume of the lower section, in order still to maintain the correct excess buoyancy of the TLB [39].

Figure 2.4: TLB B

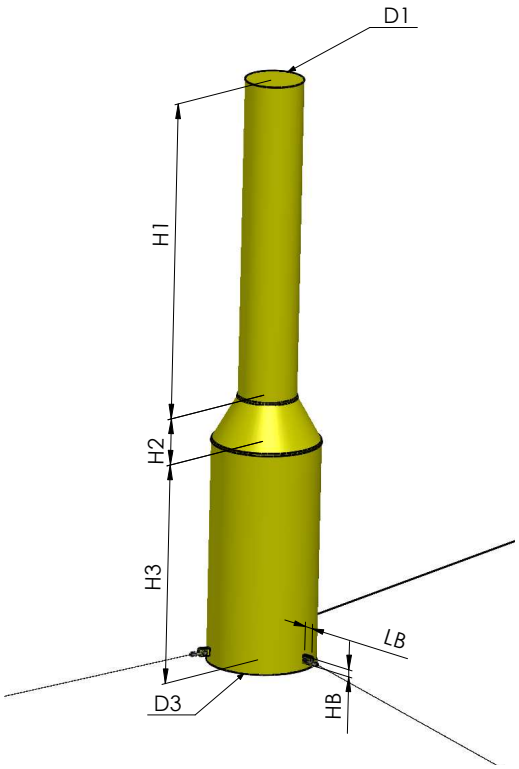

Figure 2.5: Dimensions of TLB B

In the bottom of the TLB B and in the bottom of the wind turbine, mooring line connection points are found for the purpose keeping the TLB B at a stationary position. Since the models are designed for experimental use, a realistic joint between the mooring line and the structure needs to be designed, but this is not in the scope of this project. Each connection point is consisting of a clamp with the length (LB). The coordinates shown in the Table 2.1 defines the anchoring points according to the global coordinate system.

Mooring line coordinates	**Number**	**X[m]**	**Y[m]**	**Z[m]**
Lower line	1	153.4	1.2	-74.72
Lower line	2	-75.64	-133.44	-74.72
Lower line	3	-77.72	132.24	-74.72
Upper line	4	153.4	-1.2	-74.72
Upper line	5	-77.72	-132.24	-74.72
Upper line	6	-75.64	133.44	-74.72

Table 2.1: Mooring line coordinates [39]

Table 2.2 shows the dimensions of the full-scale TLB B.

TLB Dimensions	Unit	TLB B
Top section diameter, $D1$	$[m]$	11.93
Bottom section diameter, $D3$	$[m]$	6.40
Mid-section diameter, $D2$	$[m]$	NA
Height Top-section, $H1$	$[m]$	24.68
Height Mid-section, $H2$	$[m]$	4.92
Height Bottom section, $H3$	$[m]$	35.52
Length mooring line leg, LB	$[m]$	1.2
Draft, T	$[m]$	48.68
Distance from bottom to top mooring point	$[m]$	75.84
Structural thickness (Top, mid, Bottom)	$[m]$	0.2, 0.18, 0.1
Mooring line thickness	$[m]$	0.04

Table 2.2: Properties and dimensions for TLB concepts [39]

The experimental model is produced in aluminum and PVC, as well glued with epoxy-based adhesive. However the glued connections is neglected and is therefore treated as a bonded connection in the later conducted simulations.

2.4 Limit states

When designing offshore wind turbine structures, different load types and load cases should be taken into consideration. Loads cases and design information are found in the Det Norske Veritas (DNV) [19, 20], according to the limit state considered:

- Ultimate Limit State (ULS)
- Fatigue Limit State (FLS)
- Accidental Limit State (ALS)
- Serviceability Limit State (SLS)

Since this project focus on the investigation of the dynamic response of the TLB B foundation, after a stabilization failure in terms of a mooring line fracture, only the ULS is taken into consideration. In the ULS, it is required that a structure must be able to resist the expose of an extreme load [19], but the interest for conducting a mooring line fracture analysis, implies instead that the extreme load, will force one of the TLB B mooring lines to fail.
As the TLB B is highly dynamic it would be of interest to conduct a study considering the cumulative damage and the structural life time, based on for example a misalignment simulation, in the FLS. Due the scope of this project it is delimited but recommended for further work.

2.5 Load Types

Load simulations conducted for the TLB considered in this project, is exposed to permanent loads and environmental loads, while variable functional loads and deformation loads are not taken into account. Variable functional loads is a denotation for e.g. impact loads from ships or pressure loads due to variable ballast. Deformation loads could be loads due to temperature deformations [19]. Permanent loads is in the categorization of steady

loads, such as loads from structural masses. However specific for floating structures, pretension in the mooring lines is seen as a permanent load. Fibre rope mooring lines used in the TLB B setup, may even though relaxation occurs over time, be seen as a permanent load [20]. By considering ULS, the most significant loads are the Environmental loads, that may vary in magnitude, position, and direction during the period of consideration [19]. Environmental loads are defined from

- Waves
- Current
- Ice
- Tides
- Eathquakes

According to the scope of this project, only environmental loads from waves are considered. As a consequence of the focus directed towards ULS, wave loads are estimated from regular wave realizations.

2.6 Hydrostatic stability analysis of TLB B foundation

To give an insight into the stability parameters of the TLB B, a hydrostatic analysis is made. The primary stability factor is the mooring lines, which are in tension in still water. In relation to the body of the TLB B, resulting forces acting in the longitudinal direction of the mooring lines are in equilibrium with the gravitational and buoyancy forces. The mooring lines, unless damaged, will together always act as stabilizing forces. Since displacement in the direction of a mooring line will reduce the tension in that mooring line, while the mooring line opposite the displacement will experience an increase in tension. The mooring lines can be said to uphold a stable equilibrium.
The opposite is the case for the relation between the buoyancy force and the gravitational force. Figure 2.6 show that the center of buoyancy, which is the center of the displaced fluid, is located far below the Center of Gravity (COG) of the structure.

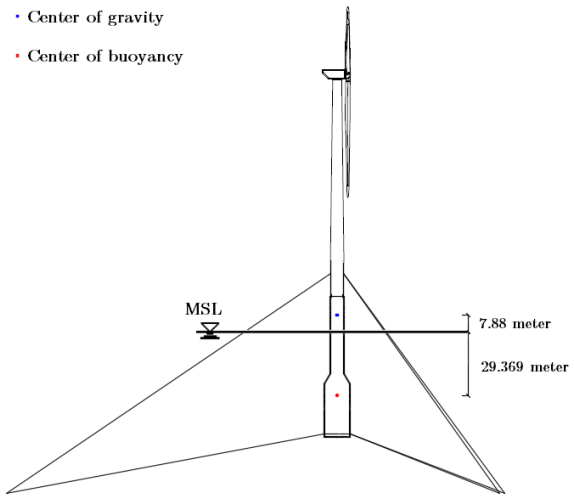

Figure 2.6: COG and COB of the TLB B in still water. Note that due to horizontal symmetry, these are located at the center of the TLB B body.

At an upright position, the resulting forces will reach equilibrium, however if the TLB B were to rotate, the buoyancy and gravity force will work to further increase rotation, meaning they act as destabilizing forces. Only the mooring lines work to counteract the rotation.
The mooring line tension forces are a result of the buoyancy force being larger than the gravitational force. The larger the excess buoyancy, the larger the mooring line tension [14]. This is the another reason for the wide lower section of the TLB B substructure. Even though it increases the distance from COB to the COG, causing the destabilizing force to become larger, the added stability through mooring line tension is causing a net increase in stability [7].

2.6.1 Expected hydrostatic consequences of a mooring line fracture

Given that the current equilibrium position of the TLB B is dependent on all the mooring lines, losing one of the mooring lines due to a fracture, will change the equilibrium position. If one of the lower mooring lines are to fracture, the opposite mooring lines will cause a rotation of the entire TLB B, until the body of the TLB B is parallel to the mooring lines. The rotation will occur around the COG, if no mooring lines are present, but due to the influence of the mooring lines, the center of rotation will have a small offset. An overview of the forces can be seen on Figure 2.7.

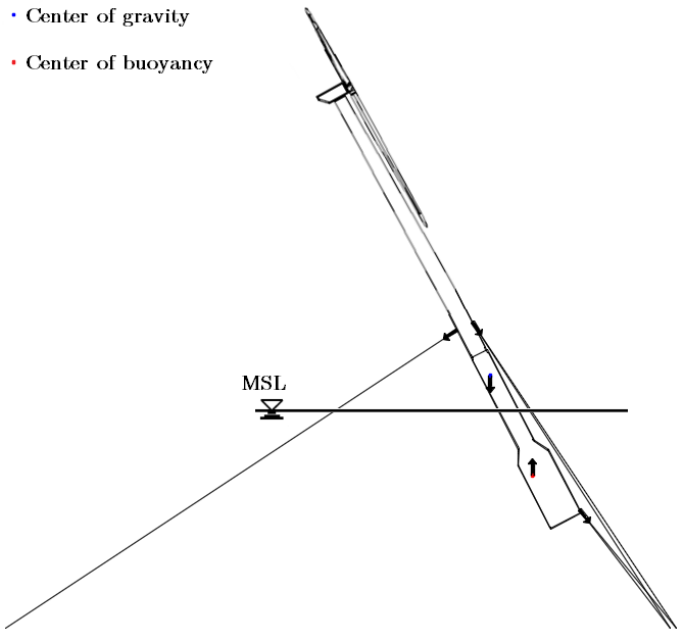

Figure 2.7: Predicted response to fracture of a lower mooring line.

In addition, the TLB B would move towards the intact mooring lines, due to the horizontal equilibrium, and an elevation of the entire TLB B will occur due to vertical equilibrium. The change in equilibrium position, will also change the COB, which with respect to the body moves downwards, due to less fluid being displaced, and in the direction of the fractured mooring line, due to rotation. Similarly the COG will change, however given that it is likely placed close the rotational center, and since the mooring lines are very light compared to the body, this change would be of minor influence.

If instead one of the higher placed mooring lines are to fracture, the response will be a higher elevation equilibrium of the TLB B, since the upper mooring lines are angled to better withstand vertical displacement, than the lower mooring lines. Likewise, the entire TLB B will move horizontally away from the fractured mooring lines, because of the tension in the opposite mooring lines. As for the rotational response, it will find equilibrium in the opposite direction of when fracturing the lower mooring line, since the upper mooring lines are placed above the COG. This rotation and the added elevation causes the COB to move downwards and away from the fractured mooring line. The remaining forces and the resulting rotation can be seen on Figure 2.8.

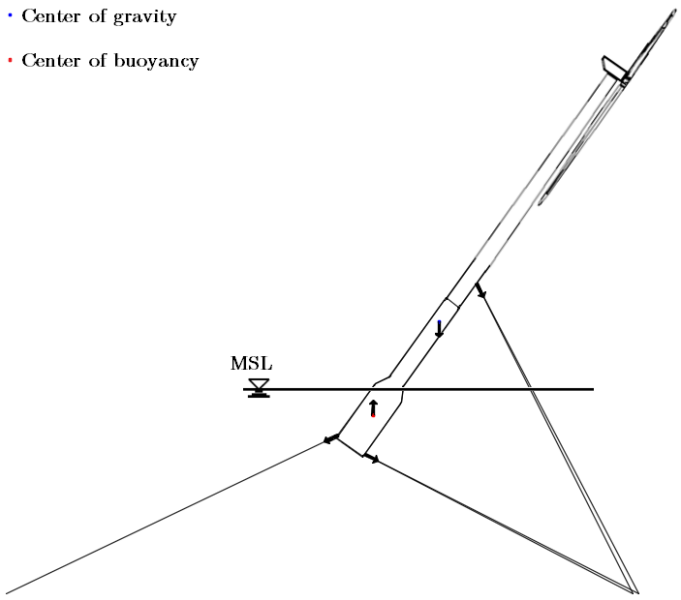

Figure 2.8: Predicted response to fracture of an upper mooring line.

3

Wave modeling

In the design of offshore wind structures, waves are among the most important subjects and as a consequence of the previously specified ULS, only realizations of regular extreme waves are considered. Large waves at finite depths, as what is the design case for the TLB B, imply that more advanced wave theories than the simple linear wave theory should be introduced. The reason is, that the limited depth i.a increases the wave steepness and thereby the nonlinearity in waves, such the assumption of small amplitude waves becomes invalid.

The Fourier based stream function theory is able to describe all wave theories [56]. To conduct reliable load simulations according to those required for the ULS, a stream function add-in is computed and implemented as a further development of SOFIA. Therefore the theoretical background for the following three wave theories will be considered in this chapter:

- Linear wave theory (Airy's wave theory)
- Stokes higher order theories
- Stream function theory

Waves considered in this project will take basis in the following model unless another model is specified:

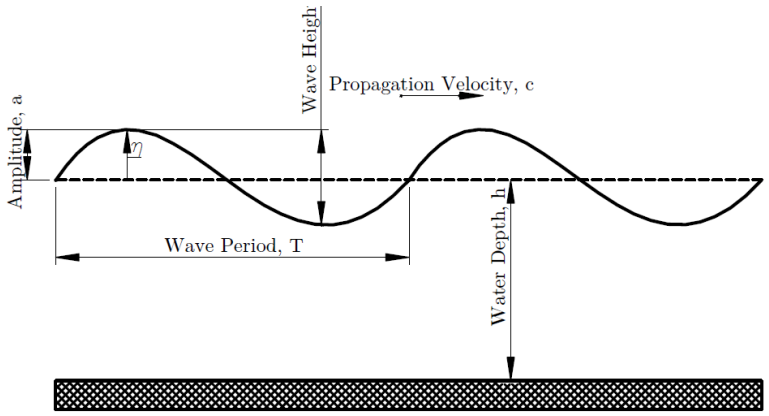

Figure 3.1: General Wave Model

The following chapter is considering the theoretical background required to understand the utilization of regular waves. Furthermore applicability of different wave theories and the stream function are discussed.

3.1 Governing equations and boundary conditions

In order to perform a kinematic description of the waves, it is assumed that the sea is *inviscid* and *incompressible*, while the motion is *irrotational*. Describing the governing equations is in this section done generally with respect to the velocity field, $\vec{V}$. The flow can be assumed to be irrotational if,

$$\omega = \nabla \times \vec{V} \tag{3.1}$$

The assumption of irrotational flow causes that the velocity field can be expressed in terms of the velocity potential,

$$\vec{V} = \vec{\nabla}\phi \tag{3.2}$$

Furthermore, the assumption about that the flow has to be incompressible, is valid if the equation of continuity is fulfilled,

$$\vec{\nabla}\vec{V} = 0 \tag{3.3}$$

If the expression for the velocity potential is substituted in to the equation of continuity, the governing equation is developed, *Laplace equation*.

$$\vec{\nabla}^2\phi = 0 \tag{3.4}$$

Due to that the flow is irrotational and inviscid, the general form of the Navier-Stokes equation can be rewritten to the generalized Bernoulli's equation. The constant shown at the right hand site, means that the pressure is constant along a stream line.

$$gz + \frac{p}{\rho} + \frac{1}{2}(\vec{\nabla}\phi)^2 + \frac{\partial\phi}{\partial t} = C(t) \tag{3.5}$$

Since the Laplace equation is the governing equation for all potential flows, the character of the flow has to be determined by means of boundary conditions. For water waves, the boundary conditions are described kinematic and dynamic. The kinematic boundary condition describes the motion of the water particle, while the dynamic boundary condition describes the forces acting on the particle [1]. The general kinematic and dynamic boundary conditions are listed below:

Kinematic BC (Bottom): The vertical velocity component is zero, since there cannot be a flow through the seabed.

$$\frac{\partial\phi}{\partial z} = 0 \quad z = -h \tag{3.6}$$

Kinematic BC (Surface): Specifies that the flow particle should remain at the water surface.

$$\frac{\partial\phi}{\partial z} = \frac{\partial\eta}{\partial t} + \frac{\partial\phi}{\partial x}\frac{\partial\eta}{\partial x} \quad z = \eta \tag{3.7}$$

Dynamic BC (Surface): The pressure at the surface should remain constant and therefore wind induced pressure variations are neglected [1].

$$gz + \frac{p}{\rho} + \frac{1}{2}(\vec{\nabla}\phi)^2 + \frac{\partial\phi}{\partial t} = 0 \quad z = \eta \tag{3.8}$$

The mathematical derivation can be found in [1].

3.2 Applicability of wave theories

When regular waves are considered regarding an ULS analysis, it is required to establish a realistic wave description by selecting a valid wave theory. The applicability of wave theories is determined by means of the water depth, h, wave period, T, and the wave height, H. The three wave parameters define the wave steepness $S = \frac{H}{L}$, that decides the appropriate wave theory.

Figure 3.2 from the American Petroleum Institute (API) [6], is for the present project used to classify wave scenarios in order to choose an applicable wave theory for the further analyzes. The regions of validity are determined by the two normalized parameters $\frac{H}{gT^2}$ and $\frac{d}{gT^2}$. In the diagram the water depth, h, is defined with a, d.

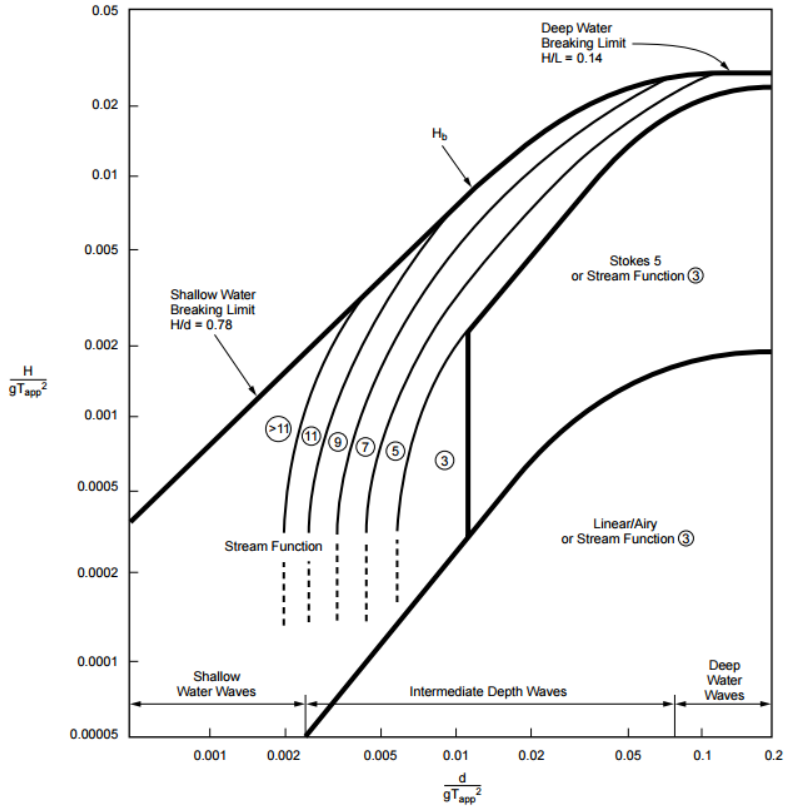

Figure 3.2: Applicability of wave theories [6]

The stream function theory is valid for the complete wave domain, but in the very low end, the easier developed Cnoidal theory can be used [56].

3.3 Linear Wave Theory

The linear wave theory is the simplest applied wave theory, but it is also shown by experiments that this theory leads to unacceptable results in many cases, due to that the linear theory describe the waves as cosine waves as shown in Figure 3.3 [10]. In reality the wave crest is shorter and steeper than the cosine wave, and the wave trough is longer and less steep. To calculate an analytical solution using the linear wave theory the two

boundary conditions at the surface have to be linearized. This is only valid to do in cases where the amplitude of the wave is small compared to wavelength and water depth. This requirement limits the linear wave theory to only be representable in very deep water ($\frac{H}{L} < \frac{1}{20}$). Higher order terms from eq. (3.7) and (3.8), is therefore discarded:

$$\frac{\partial \phi}{\partial z} \approx \frac{\partial \eta}{\partial t} \quad z = 0 \tag{3.9}$$

$$g\eta + \frac{\partial \phi}{\partial t} \approx 0 \quad z = 0 \tag{3.10}$$

Based on the linearized boundary conditions an exact solution for the governing equation can be found and the velocity potential can be written as,

$$\phi = -\frac{ag}{\omega} \frac{\cosh(k(z+h))}{\cosh(kh)} \sin(\omega t - kx) \tag{3.11}$$

The surface elevations is,

$$\eta = \frac{H}{2} \cos(\omega t - kx) \tag{3.12}$$

Particle kinematics will not be mentioned in this section, but can be calculated by differentiation of the velocity potential. In order to calculate an analytical solution by use of the linearization, it is not possible to determine the particle kinematics in the crest unless Wheeler Stretching or Linear Extrapolation is applied [1]. The standard wave add-in in SOFIA is based on the numerical 1st order wave theory approach, where the elevation height is estimated instantaneous to the time. The numerical approach implies that a stretching method is not needed.

3.4 Stokes Wave Theory

In cases with waves propagating on finite depths, it is as aforementioned not valid to assume a small wave amplitude compared to the water depth and wavelength. As a result, it is necessary to include nonlinear terms in the description of the waves. A method of describing nonlinear waves is by use of Stokes wave theory, where it is assumed that all variables can be series expanded. Eq. (3.13) shows the expansion procedure for the velocity potential and the elevation height, but the same expansion procedure may be conducted for the particle kinematics and the pressure field.

$$\begin{aligned} \phi &= \phi_1 + \phi_2 +, ..., +\phi_n \\ \eta &= \eta_1 + \eta_n +, ..., +\eta_n \end{aligned} \tag{3.13}$$

At the same time it is necessary to introduce the order of magnitude,

$$\mathbf{o}(\phi^{i+1}) = \mathbf{o}(\phi^i \frac{H}{L}) \tag{3.14}$$

These expanded series have then to be substituted into the governing equation and the nonlinear boundary conditions. It is in eq. (3.15) shown in general, how each term of the expanded velocity potential are substituted into the governing equation,

$$\frac{\partial^2 \phi^n}{\partial^2 x} + \frac{\partial^2 \phi^n}{\partial^2 z} = 0 \tag{3.15}$$

As in the case for the linear wave theory, the position at the surface is unknown, which is solved by use of a Taylor expansion from $z = 0$ of the dynamic and kinematic boundary condition. All terms of $(\frac{H}{L})^n$ where n is greater or equal to the Stokes order in their order of magnitude, must be discarded. As the linear wave theory is only depended on the linear term in the Taylor expansion, it is for the second order theory necessary to include nonlinear terms,

$$\frac{\partial \phi}{\partial z}(x, \eta, t) = [\frac{\partial \phi}{\partial z}]_0 + \underbrace{\frac{\eta}{1!}[\frac{\partial^2 \phi}{\partial^2 z}]}_{\text{Nonlinear part}} + ..., \tag{3.16}$$

After conducting this operation to both the dynamic and kinematic boundary condition, it is possible to simplify the calculation by eliminating the elevation height in the equations.

$$\frac{\partial^2 \phi}{\partial^2 z} + \frac{1}{g}\frac{\partial^2 \phi}{\partial^2 t} \tag{3.17}$$

Eq. (3.17) is then solved for all the parts in the series expansion and added together. Figure 3.3 shows the parts in the series expansion, as well as the 2nd order stokes wave [10].

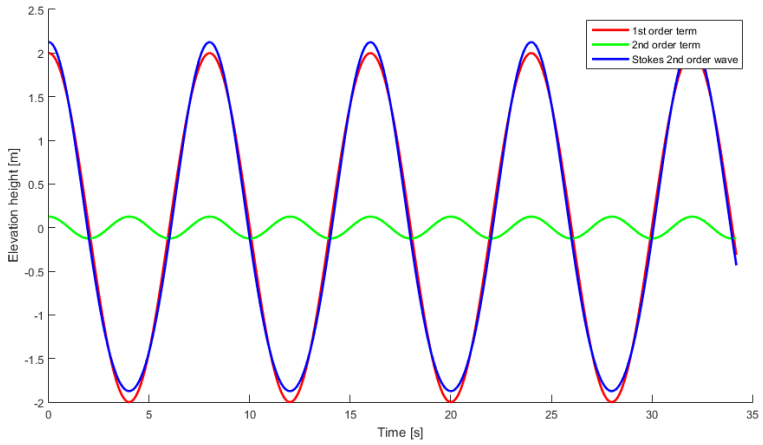

Figure 3.3: 2nd order stokes wave (Red = 1st order term, Green = 2nd order term and Blue = 2nd Stokes wave)

It is from Figure 3.3 shown how the elevation height from the 1st order term and the 2nd order term is added together, in order to establish the elevation height for the 2nd order wave. Simultaneously the effect discussed in section 3.3, where the crest becomes shorter and steeper and the trough longer and less steep, is slightly seen.

3.5 Stream function wave theory

For shallow water conditions ($\frac{h}{L} < \frac{1}{20}$) the waves become very nonlinear and therefore, to describe the waves, a high order is required. Every time the Stokes theory is extended to a higher order, it requires a lot of extra calculations and will slow down the wave simulation. To avoid that, utilization of the stream function wave theory is an advantage, due to that it is possible to determine a solution for the exact nonlinear surface boundary conditions, eq. (3.7) and (3.8), by use of a Fourier expansion. Since the procedure of fulfilling the

boundary conditions is conducted by a numerical iteration, the solution of the governing equation is an approximation. The stream function is not subject to any demands of $\frac{H}{L}$ or $\frac{h}{L}$ and it can therefore as aforementioned be used for describing all wave theories, which is convenient in the scope of this project, as well as it extents the coverage of SOFIA [56].

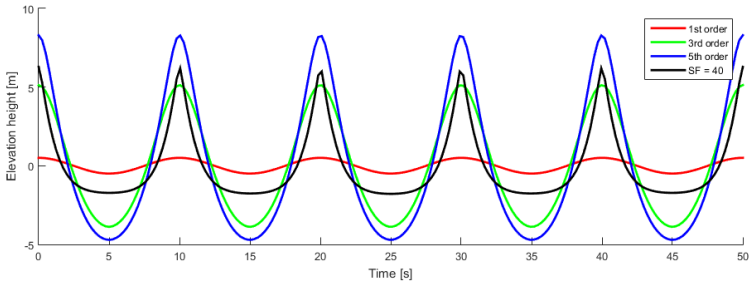

Figure 3.4: 2nd order stokes wave (Red = 1st order waves, green = 3rd order waves, blue = 5th order waves and black Stream function 40 order)

3.5.1 Coordinate systems and current implementation

Before describing the stream function wave theory, it is convenient to discuss wave simulation with simultaneously a uniform current implemented. The implementation introduces three required coordinate systems; (x, y)-coordinate system fixed to the water body, (x_r, z_r)-coordinate system fixed at the wave crest and the (x_a, z_a)-coordinate system, which is the absolute coordinate system fixed to the seabed.

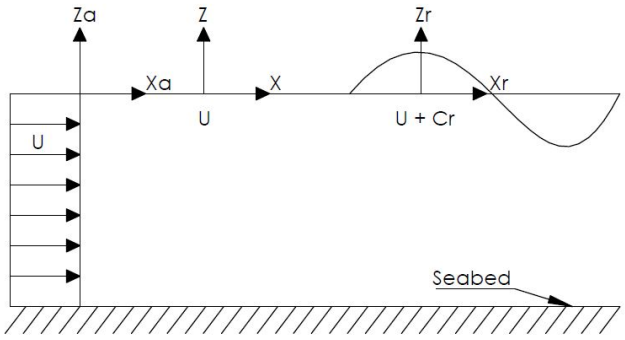

Figure 3.5: Flow observed from (x_a, z_a)–coordinate system. The figure is inspired from [10]

Figure 3.5 shows the flow observed from the (x_a, z_a)-coordinate system. As a result, the (x_r, z_r)-coordinate system is propagating to the right with the wave, having the velocity, c_r. In cases where a current is included in the simulation, the water body is moving with a uniform velocity and is therefore the propagation velocity of the wave, seen from the absolute coordinate system is

$$c_a = c_r + U \tag{3.18}$$

For simulations where current is not included the (x, y)-coordinate system is steady and equal to the (x_a, y_a)-coordinate system [10].

3.5.2 Boundary conditions

The stream function wave theory is as for the earlier mentioned theories, described by use of potential theory assumptions, but in the (x_r, z_r)-coordinate system. The result is that the surface elevation will keep constant and the flow is assumed to be steady. A stream function is defined as:

$$u = -\frac{\partial \psi}{\partial z} \quad v = \frac{\partial \psi}{\partial x_r} \tag{3.19}$$

As a result, the *Laplace equation* is written with respect to the stream functions

$$\frac{\partial^2 \psi}{\partial^2 x_r} + \frac{\partial^2 \psi}{\partial^2 z} = 0 \tag{3.20}$$

Utilization of stream functions implies some convenient definitions that are used to establish the kinematic boundary conditions. (1) A flow will never cross a stream line, since the velocity by definition, always is tangent a stream line. (2) Two closely spaced stream lines produces a volumetric flow in between [36]. The kinematic boundary conditions for the stream function wave theory is stated as,

$$\psi = Q \quad z = -h \quad \text{and} \quad \psi = 0 \quad \text{for} \quad z = \eta \tag{3.21}$$

The volumetric flow between stream lines is expressed in eq. (3.22) and found by integrating the horizontal velocity from the seabed to the elevation height.

$$Q = \int_{-h}^{\eta} u dz \tag{3.22}$$

Due to the assumption of steady flow, the transient part of eq. (3.23) is zero and the equation is reduced to the following.

$$g\eta + \frac{1}{2}[(-\frac{\partial \psi}{\partial z})^2 + (\frac{\partial \psi}{\partial x_r})^2] = R \tag{3.23}$$

In the equation, R is named as the *Bernoulli's constant*. Due to that the stream function is described according to the (x_r, z_r)-coordinate system, the wave is seen symmetrical about the crest, and it is therefore possible set up an approximate solution of the stream function. The approximate solution is based on a truncated Fourier series of an even function.

$$\psi(x, \eta) = c_r(\eta + h) + \sum_{j-1}^{N} B_j \frac{sinh(jk(\eta + h))}{cosh(jkh)} \cos(jkx) + Q \tag{3.24}$$

The approximate solution of the stream function does automatically satisfy the kinematic boundary condition and the governing equation. N is the stream function order and is chosen according to the wave complexity [10].

3.5.3 System of equations

The approximate solution of the stream function has to be substituted in to the boundary conditions and evaluated for the points in (x_r, z_r)-coordinate system. To describe the wave surface, $N + 1$ points are required, and since there is two boundary conditions to each point, $2N + 2$ equations has to be established. Figure 3.6 shows how the points used for describing the free surface are located for the example of $N = 2$:

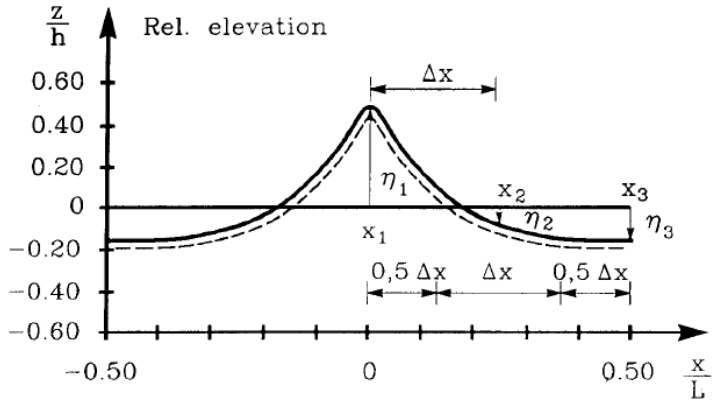

Figure 3.6: Location of points for Stream function wave [10]

Since the unknown's in eq. (3.24) are $\eta(N+1)$,$B_j(N)$,c_r,c_a,Q and R, it is necessary to establish three extra equations, such the number of equations changes to $2N+5$. The extra three equations cover the mean elevation height, the wave height and the wave length [10].

$$\bar{\eta} = \frac{1}{L}\int_0^L \eta dx_r = 0 \tag{3.25}$$

$$H = \eta_{max} - \eta_{min} \tag{3.26}$$

$$L = c_r T \tag{3.27}$$

Solving procedure
To solve the system of nonlinear equations, an extended version of the Newton-Raphson iteration method, designed for handling multivariable systems is used. The Newton-Raphson problem is stated as:

$$\delta x = -J^{-1}(x) f(x) \tag{3.28}$$

$$x_{n+1} = x_n + \delta x \tag{3.29}$$

The iteration is derived by use of a Taylor expansion in order to establish a linear approximation, used to solve the nonlinear system of wave equations. $[J(x)]$ is the Jacobian matrix:

$$[J(x)] = \begin{bmatrix} \frac{\partial f_1}{\partial x_1} & \cdots & \frac{\partial f_1}{\partial x_n} \\ \vdots & \ddots & \vdots \\ \frac{\partial f_n}{\partial x_1} & \cdots & \frac{\partial f_n}{\partial x_n} \end{bmatrix} \tag{3.30}$$

To start the Newton-Raphson solving procedure a starting guess is required. In the programmed stream function add-in following guess, based in the linear wave theory is used [10]:

$$
\begin{aligned}
L &= L^1 \\
c_r &= \frac{L}{T} \\
c_a &= c_r \\
Q &= -c_r h \\
R &= 0.5{c_r}^2 \\
\eta_i &= \frac{H}{2}\cos(kx_i) \quad for \quad i = 1, 2, ..., N+1 \\
B_1 &= -\frac{\pi H}{kT\tanh(kh)} \\
B_{i+1} &= 0
\end{aligned}
\tag{3.31}
$$

The first B coefficient is found by setting the vertical particle velocity from the 1st order theory equal to $w = \frac{\partial \psi}{\partial x}$, while the remaining coefficients are set to zero due to that the Fourier coefficients are decreasing, when the frequency is increasing [10].

3.5.4 Elevation height and particle kinematics

The elevation height is found by use of finite Fourier series based on the N+1 η-values.

$$
\eta(x) = 2\sum_{j-1}^{N-1} a_j \cos(jkx_r) + a_N \cos(Nkx_r) \tag{3.32}
$$

Particle velocities is as for the earlier mentioned wave theories found by differentiating of the velocity potential with respect the direction. The particle accelerations are found by use of the material derivative, and since the waves are propagating with a constant form stated as following:

$$
\begin{aligned}
\frac{du}{dt} &= (-c_a + u)\frac{\partial u}{\partial x} + w\frac{\partial u}{\partial z} \\
\frac{dw}{dt} &= (-c_a + u)\frac{\partial w}{\partial x} + w\frac{\partial w}{\partial z}
\end{aligned}
\tag{3.33}
$$

The particle kinematics for the stream function (and for all previously mentioned theories) are distributed as in Figure 3.7, with maximum horizontal velocity in the crests and minimum velocity in the trough [10].

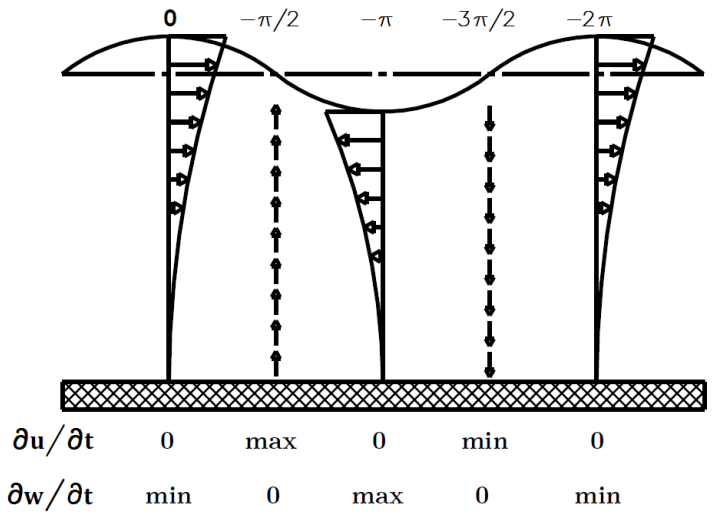

Figure 3.7: Particle kinematics for regular wave. The figure is inspired from [1].

The previously mentioned discharge, which is also named Stokes drift, is automatically included when steep waves at finite depth are evaluated. As a result of the steepness, the particle trajectories are no longer enclosed, and a horizontal net transport is occurring in the same direction as the waves, as seen in figure 3.8. If no current is applied in the analysis it is described by: $U_{Stokes} = \frac{\overline{q_{wave}}}{h}$ [10].

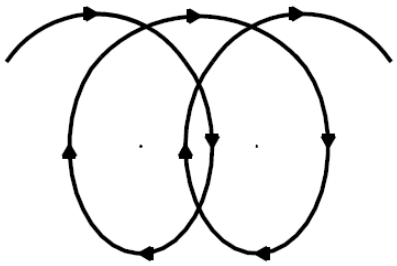

Figure 3.8: Horizontal particle trajectory of a wave at finite depth

3.5.5 Simulation of wave cases close to the limit of validity

Although the stream function theory is applicable for describing all wave theories, extreme wave load cases can cause convergence problems for the Newton-Raphson solver. The convergence problem is a result of the wave scenario becoming to nonlinear. To solve the problem, it is required to establish an incremental increase of the wave height, where a step size of $\Delta H = \frac{H}{8}$ or smaller is recommended [10]. In order to control the incremental step size in the developed stream function add-in, an initial wave height and a desired wave height must be defined. This means for extreme wave cases close to the limit of the Newton-Raphson solver (for the wave add-in an order higher than $N = 50$ are assumed to be close to the limit of the Newton-Raphson solver) the initial wave height must be set low, compared to the desired wave height. Before starting a simulation, the number of maximum iterations, as well as the number of incremental steps of the wave height, must be defined.

3.5.6 Validation and implementation in SOFIA

To ensure the validity of the developed stream function add-in, validations against the in-house software Wavelab and Ocean Commands in ANSYS inc., has been performed before and after implantation in SOFIA. The validation has focused on the Newton-Raphson iteration procedure, as well as the particle kinematics, which has shown successful results.

In order to fit the stream function add-in to the structure of SOFIA, it has been changed from 1-dimension to 2-dimension, by replicating the wave realization.

Change in propagation direction
As a result of the extension in to 2D, the possibility of changing the wave and current propagation direction has been implemented. For both the wave and current, an angle of 0 deg implies propagation from negative to positive.

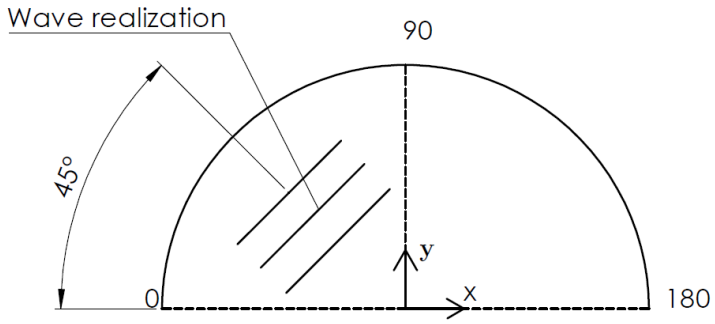

Figure 3.9: Wave and current propagation angle

4

Hydrodynamic effects of slender frame structures

When the water motion from the waves and current is determined through potential theory, the forces exerted on a submerged structure can be found. If the submerged structure is a slender cylinder with a diameter less than 20 % of the wave length, then the real flow approximation e.g. Morison equation, is applicable.

To establish an understanding of selecting a flow theory appropriate for the simulation of the TLB B concept important hydrodynamic effects are considered. As aforementioned SOFIA is based on the real flow approximation, the relative form of the Morison equation, by which the corresponding motion equation is derived.

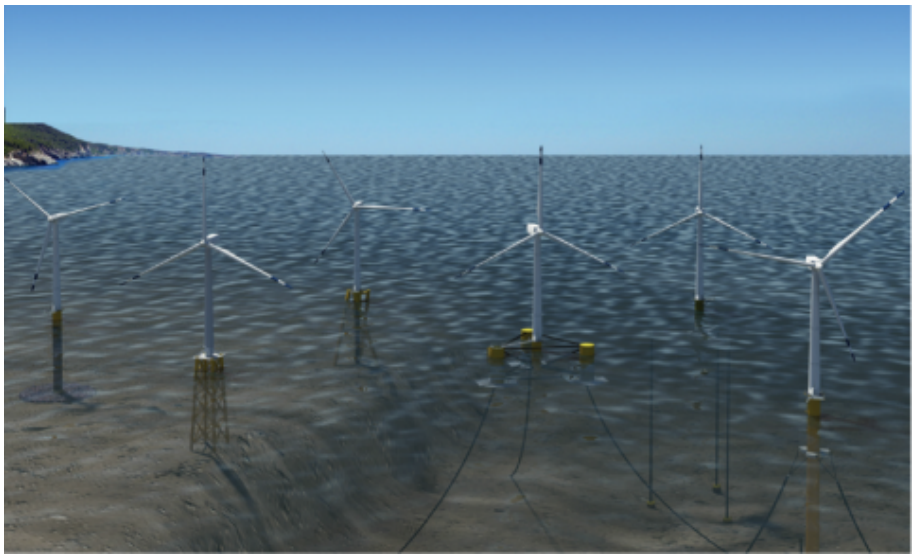

Figure 4.1: Illustration of FOWT concepts [22].

The chapter is developed in a way that first introduces the real flow theory, and explains the technical differences in proportion to the potential flow theory. Subsequently the construction of the Morison equation and the derivation of the equation of motion for the TLB B is explained. Lastly the chapter is considering the theoretical background for the later considered experimental results.

4.1 Consideration regarding slender frame structures and large volume structures

In order to correctly describe the motions of a floating structure, it is required to determine, whether the structure is defined as a Large Volume Structure or a Slender Frame Structure. Depending upon the flow in the vicinity of the structure, the wave load contribution can either be inertia force or drag force dominated. For large volume structures e.g. semi-submersibles and ships, the incident waves are reflected and scattered from the structural surface. As a result, the wave loads are inertia force dominated and may be determined by use of potential theory, where diffraction should be included to account for the scattered waves [14]. For large volume floating structures, the structure apply loads to the sea, which leads the creation of waves. The phenomena is named radiation and it should be implemented in simulations [30].

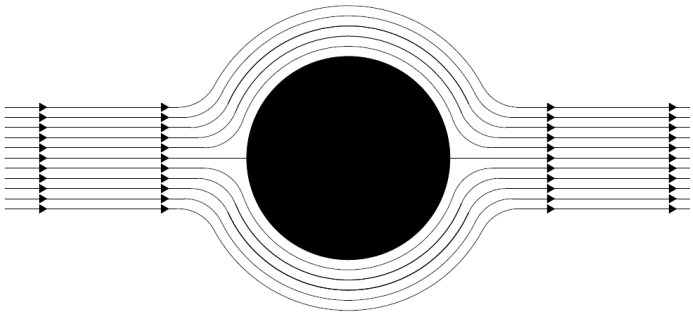

Figure 4.2: Illustration of potential flow around a cylinder.

For slender frame structures, the contribution from the reflected and scattered waves are small compared to the contribution from shear forces. Shear forces can be noted as drag occurring over the structural surface, which for slender frame structures is increasingly relevant, due to occurrence of flow separation. Since it is not possible to account for flow separation using potential theory, it is for slender frame structures needed to determine wave loads by use of the real flow approximation e.g. Morison Equation [30].

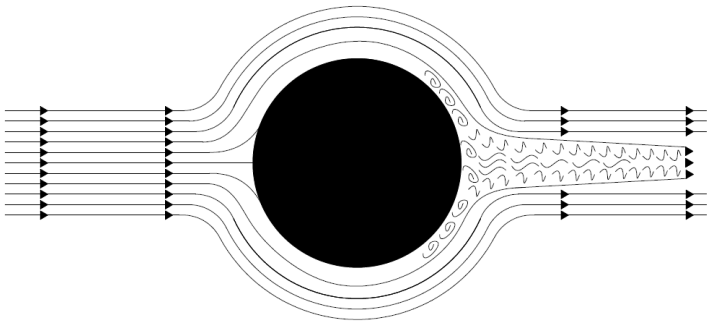

Figure 4.3: Illustration of real flow around a cylinder.

4.2 Morison equation

When considering slender cylinders, it is assumed that the motion of the fluid around the cross section is the same, only changing along the length of the cylinder. This simplification reduces the amount of forces that must be taken into consideration. When considering submerged structures then force contributions comes from gravitational forces, viscous forces, and inertia forces. Gravitational forces are not incorporated in the Morison equation, but the viscous forces and inertia forces are. The viscous forces are reduced to only be a function of the undisturbed stagnation pressure, and are physically the drag forces created when the fluid flow and structure separate. As for the inertia forces, these are reduced to not incorporate second order effects or diffraction, and is only a sum of the Froude Krylov force and the force created form disturbance of the flow by the structure. The resulting inertia and drag forces can be found in the Morison equation, here illustrated as eq. 4.1.

$$F(t) = \frac{\pi}{4}\pi C_M D^2 \dot{u}(t) + \frac{1}{2}\rho C_D D u(t)|u(t)| \tag{4.1}$$

Originally the Morison equation does not consider the motions of the structure, which for a FOWT can be significant. In order to take these motions into consideration, the relative form of the Morison equation can be used. This is a modified version of the Morison equation, where the difference between wave particle motions and structural motions are incorporated instead of only the wave particle motions [30].

$$F(t) = \frac{\pi}{4}\pi C_M D^2 \dot{u}_{rel}(t) + \frac{1}{2}\rho C_D D u_{rel}(t)|u_{rel}(t)| \tag{4.2}$$

4.2.1 Inertia and drag coefficients

C_M and C_D are the inertia coefficient and drag coefficient respectively. The inertia coefficient is introduced to consider the pressure field and the flow disturbances that occur when the fluid and body collide. The contribution from the pressure field is easily determined from potential theory, but the disturbance cannot be determined theoretically. Instead an experimental approach has been used to determine the inertia coefficient [30].

$$C_M = 1 + C_A \tag{4.3}$$

C_A is the added mass coefficient, which describe how the mass of the fluid move around the submerged body, as a force pr. unit acceleration. A precise determination of the added mass coefficient is often very hard, as is the case for the drag coefficient C_D. Determination often requires use of model tests, and even then the result yields coefficients with large tolerances. [30] DNV has produced a guidance as to what the coefficients could be set to, which is dependent on the Keulegan Carpenter Number (KC), the Reynolds Number (KC), and the relative roughness. Table 4.1 to 4.2 shows the interval of which the coefficients can be expected to be [19].

C_D	Surface of structural member	
KC	Smooth	Rough
$KC < 2$	0	0
$2 < KC < 6$	0.65	1.05
$6 < KC < 13$	Linear variation from 0.65 to 0.85	Linear variation from 1.05 to 1.5
$13 < KC < 30$	Linear variation from 0.85 to 0.65	Linear variation from 1.5 to 1.05
$KC > 30$	0.65	1.05

Table 4.1: C_D intervals proposed by DNV [19].

C_M	Surface of structural member	
KC	Smooth	Rough
$KC < 6$	2.0	2.0
$6 < KC < 30$	Linear variation from 2.0 to 1.65	Linear variation from 2.0 to 1.2
$KC > 30$	1.65	1.2

Table 4.2: C_M intervals proposed by DNV [19].

The reason for this uncertainty is due to the nature of the Morison equation. It is designed to be accurate when considering inertia force and drag force separately, meaning one of the forces is dominant. If neither force is dominant uncertainties occur, but because no better alternative exist, the Morison equation is still used in these cases. Whether drag or inertia is dominant can be determined from the KC. For low values ($KC < 3$) inertia is dominant, and for high values ($KC > 45$) drag is dominant. In practice, if one force is dominant, then only that part of the Morison equation is used. With relatively low contributions from drag ($3 < KC < 15$) the quadratic drag term can be linearized for simplification, however for ($15 < KC < 45$) then the full Morison equation has to be used [30].

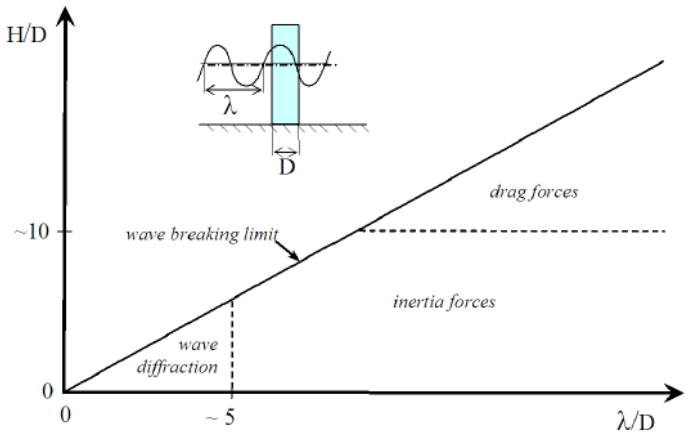

Figure 4.4: Illustration of the relative importance of inertia, drag and diffraction [19]

4.2.2 Determining inertia and drag coefficient when neither is dominant.

Many approaches have been made to experimentally determine the inertia and drag coefficients. Morison himself suggested that the wave force was measured at maximum particle

velocity, meaning the particle acceleration would be zero. Then the only force present would be the velocity dependent drag force. The same would be true for the inertia force at maximum acceleration, where the velocity would be zero. The method is simple, but it lacks accuracy, since the force curve is steep when measuring maximum velocity.

Other methods have been proposed, like using Fourier series, which takes every measurement of force, velocity, and acceleration into consideration, and the least square method, which finds and approximated solution through numerical computation. Though each method is an appropriate way to determine the coefficients, a comparison of the results made from the same measurements will show that each method will yield a different result [30].

4.3 Motion dynamics of floating small volume structures

With basis in the previous mentioned definition of whether a structure is a large volume structure or a slender frame structure, the TLB B may be described as a slender frame structure. This means the wave excitation force can be derived from the relative form of the Morison equation. Equally to a motion analyzis for a large volume structure, the rigid body motions are described by six independently degrees of freedom; three translational (surge, sway and heave) and three rotational (pitch, roll and yaw) [30]. Due to that small volume structures are often consisting of long flexible members, it is needed, also to include the contribution from the internal deflection in the analysis [14].

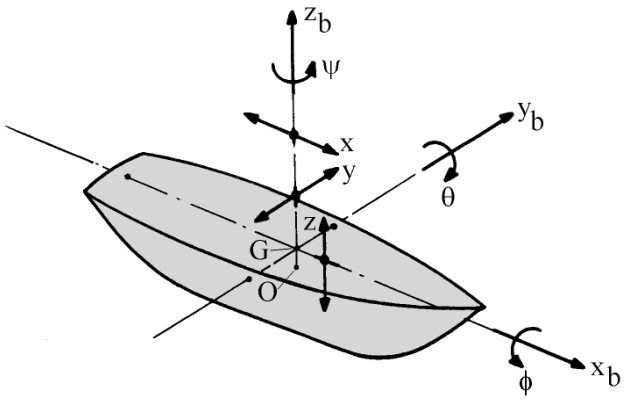

Figure 4.5: Illustration of degrees of freedom for a floating structure [30].

4.3.1 Responses in regular sea state

By investigating the response of a floating structure and in particular a the TLB B, it will often only be exposed to small motions, and can therefore be modeled linear, by the motion equation known from a damped mass-spring system [50].

$$[M]\ddot{\vec{x}} + [C]\dot{\vec{x}} + [K]\vec{x} = \vec{F}(t) \tag{4.4}$$

In eq. (4.4) $[M]$ is the structural mass matrix, $[C]$ is the linear damping matrix and $[K]$ is the structural stiffness matrix, while $\vec{F}(t)$ is the external force.

$$[M]\vec{\ddot{x}} + [C]\vec{\dot{x}} + [K]\vec{x} = \vec{F}(t) \tag{4.5}$$

In order to use the mass-spring formulation for describing floating structures, it is necessary to introduce the hydrodynamic stiffness matrix on the left hand side of the equation and rewrite the right hand side, to contain wave forces and gravitational force.

$$[M]\vec{\ddot{x}} + [C]\vec{\dot{x}} + ([K] + [K_h])\vec{x} = \vec{F}_{m,r}(\vec{\dot{u}}, \vec{\ddot{x}}, \vec{u}, \vec{x}) + \vec{F_G} \tag{4.6}$$

The hydrodynamic stiffness occurs as a result of the hydrostatics for the floating structure and is therefore consisting of the buoyancy, restoring forces, and moments. For the sake of simplicity the hydrodynamic stiffness is moved to the right hand side such it acts, as an external buoyancy force [4].

$$[M]\vec{\ddot{x}} + [C]\vec{\dot{x}} + [K]\vec{x} = \vec{F}_{m,r}(\vec{\dot{u}}, \vec{\ddot{x}}, \vec{u}, \vec{x}) + \vec{F_G} + \vec{F_B}(\vec{x}) \tag{4.7}$$

4.4 Frequency considerations of FOWT

Investigation of FOWT, as well as bottom fixed foundations implies, as aforementioned, that the structure is exposed to different dynamic loads and not only the wave loads considered in this project. In particular wind loads and mechanical loads from the wind turbine, is important to take into consideration, as they contribute to induce free and damped oscillations, in the wind turbine and the foundation structure [40]. As a consequence of the induced oscillations, critical frequencies will occur, by which the structure must be designed such its eigenfrequencies are located outside the critical areas. Figure 4.6 show the general critical frequencies.

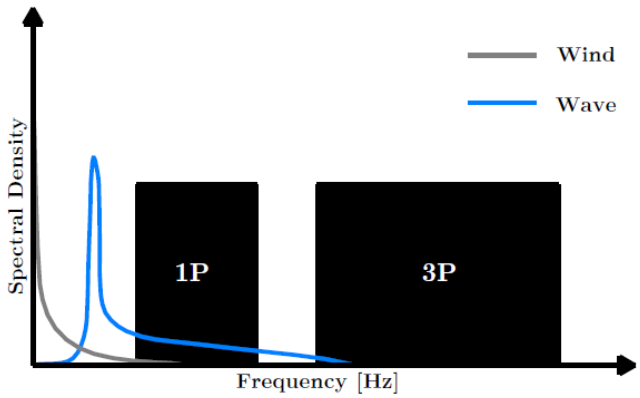

Figure 4.6: Frequency spectrum of a wind turbine system. Inspired by [18].

The excitations found in the lower end of the spectra are based on the aero- and hydrodynamic loads from wind and waves. The two excitation ranges named 1P and 3P are based on mechanical loads from the wind turbine, where the 1P excitation range is the forced frequency from the rotor, when the wind turbine is in operation. The 3P excitation range is the frequency corresponding to the shadowing effect each time a blade passes the tower. The integer 3 defines that it is a 3-bladed wind turbine. Since it is not possible for the control system of the wind turbine to ensure a completely constant rotor revolution speed, the mentioned excitation ranges are extended $\pm 10\%$ around the 1- and 3P frequencies [40].

With basis in the academic wind turbine from National Renewable Energy Laboratory (NREL), the critical excitation ranges are located from 0.115-0.220 Hz (1P) and from 0.345-0.660 Hz (3P) [29]. The excitation frequencies is used to classify the wind turbine foundation structure; below 1P is in the soft-soft region, between 1P and 3P is soft-stiff and above is classified as stiff-stiff [18].

4.5 Model Test

Even tough if it is ships, floating wind turbines, or floating oil and gas structures that are considered, a highly complex and dynamic system is investigated, and may therefore not be completely understood theoretically at the moment. Model testing is therefore an effective tool to investigate and understand the response of the floating structure, but is simultaneously costly procedure [15]. The model tests considered through this project is limited to following:

- Decay test
- Seakeeping test

4.5.1 Decay Test

When a frequency analysis is conducted for a floating structure, it is important to account for the influence from the surrounding water. A method is to utilize an experimental decay test, from where it is possible to determine the structural eigenfrequency and calibrate the added mass coefficient. Decay tests are conducted by exposing the floating structure to a forced oscillation in the previously mentioned six degrees of freedom (See section 4.3.1) [31, 39]. Clean oscillations are produced by applying forces and moments in the COG. The experimental decay tests are considered in chapter 6.

4.5.2 Seakeeping Test

The second model test that is considered in chapter 6 is the seakeeping test established to investigate the dynamic response of a floating structure, when it is exposed to wave loads. Since it as previously mentioned, is not possible to theoretically determine the hydrodynamic coefficients (normal drag, tangential drag and inertia mass), in the Morison equation, seakeeping tests are an important tool [30, 12]. They are as the decay tests important, in order to calibrate numerical tools to correctly describe the wave loads and thereby the dynamic response.

4.6 Froude scaling

In order to test the dynamic response of a full size FOWT concept, a smaller test model can be used, though correct scaling is important. To ensure that the test model is dimensioned correctly, the Froude scaling can be used. Froude scaling is applicable when hydrodynamic and gravitational forces are dominant, and it works by upholding geometric, kinematic, and dynamic similarity between test model and full size model.

Geometric similarity means that the linear dimensions of the test model and full size structure are scaled equally. Kinematic similarity refers to the wave kinematics, and it requires that the ratio between accelerations and velocities of the test model wave is the same as

that of the full size wave, in the vectorial directions.
Dynamic similarity ensures that the response between wave and structure is the same for the test model and the full size structure. This means that the ratio of masses and vectorial forces must be equal between the test model and the full size structure. [27]

These similarities are uphold using the scaling ratios found in Table 4.3.

Characteristic	**Dimension**	**Scale ratio**
Geometric		
Length	$[L]$	N_L
Area	$[L^2]$	N_L^2
Volume	$[L^3]$	N_L^3
Kinematic		
Time	$[T]$	$N_L^{1/2} N_\rho^{1/2} N_\gamma^{-1/2}$
Velocity	$[LT^{-1}]$	$N_L^{1/2} N_\rho^{-1/2} N_\gamma^{1/2}$
Acceleration	$[LT^{-2}]$	$N_\gamma N_\rho^{-1}$
Discharge	$[L^3T^{-1}]$	$N_L^{5/2} N_\rho^{-1/2} N_\gamma^{1/2}$
Kinematic Viscosity	$[L^2T^{-1}]$	$N_L^{3/2} N_\rho^{-1/2} N_\gamma^{1/2}$
Dynamic		
Mass	$[M]$	$N_L^3 N_\rho$
Force	$[MLT^{-2}]$	$N_L^3 N_\gamma$
Mass Density	$[ML^{-3}]$	N_ρ
Specific Weight	$[ML^{-2}T^{-2}]$	N_γ
Dynamic Viscosity	$[ML^{-1}T^{-1}]$	$N_L^{3/2} N_\rho^{1/2} N_\gamma^{1/2}$
Volume Elasticity	$[ML^{-1}T^{-2}]$	$N_L N_\gamma$
Stress	$[ML^{-1}T^{-2}]$	$N_L N_\gamma$

Table 4.3: Froude scaling ratios [27].

5
Structural modeling

As mentioned in chapter 4, the TLB B can correctly be modeled as a slender frame structure in regards to hydrodynamic forces, which makes the FEM based corotational beam formulation in SOFIA applicable as a structural modeling method.
A structure floating on the sea will, unless it is somehow constrained to avoid it, undergo large displacements and rotations. This is a problem for regular beam elements, since they do not allow large rigid body motions. A beam theory that does allow large rigid body motions is the corotational beam formulation. In addition, the corotational beam theory incorporates nonlinear column effect and shortening due to bending, which require a nonlinear solver. As a for time-integration, the non-linear Newmark method is used in SOFIA, with a Newton-Raphson formulation as a linear apprioxmiation method.

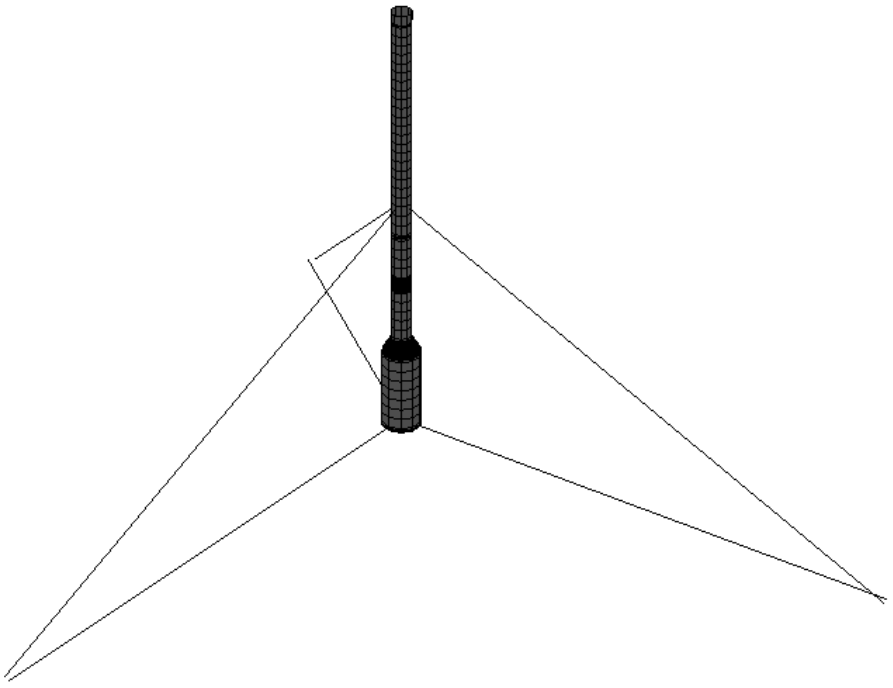

Figure 5.1: Illustration of TLB B model. Note that the use of surface elements are for illustrative purposes only.

The chapter will focus on the theoretical understanding of the numerical concepts of the corotatioanl beam theory, the non-linear Newmark integration method, the Newton-Raphson method, and other structural aspects of SOFIA. For further theoretical explanation of the methods see Appendix C and for a validation of the structural section of SOFIA see Appendix D.

5.1 Corotational beam theory

Unlike regular beam theories where deformations and rotations are defined with reference to the global coordinate system, the corotational beam theory uses element based local coordinate systems. The deformations and rotations of each element is a sum of the rigid body motions in the global coordinate system, and the local deformations of each beam element within the local reference coordinate system, as illustrated in Figure 5.2. **(1)** is the undeformed element. **(2)** shows the element after rigid body translations and rotations. Note that the local reference coordinate system is always located with an equal distance to the element ends A and B. **(3)** illustrates the local deformations of the element in the local reference coordinate system. These deformations are the strain inducing deformations [32].

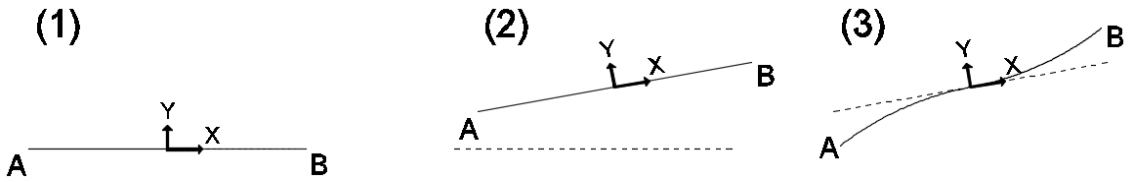

Figure 5.2: Deformation and rotation concept of the corotational beam theory, shown in 2D for illustrative simplicity [32].

5.1.1 Element stiffness

The element stiffness matrix consists of input from two different kinds of stiffnesses. One is the stiffness responsible for the change of length and the rigid body motions. This is called the rotation stiffness matrix $[K_r]$. The other is the stiffness responsible for bending and torsion of the beam, and is a combination of the constitutive stiffness and the geometric stiffness. This stiffness is called the deformation stiffness $[K_d]$. Adding the rotation stiffness and the deformation stiffness as shown in eq. (5.1) results in the element stiffness.

$$[K_e] = [K_r] + [S][K_d][S]^T \tag{5.1}$$

$[S]$ is the transformation matrix for corotational beams.
The rotation stiffness matrix is derived using the principal of virtual work, which initially means the matrix is not symmetric, but with some adjustments from the deformation stiffness matrix, it becomes symmetric, which is computationally faster. As for the deformation matrix, the constitutive stiffness matrix is multiplied with the contributions from the geometric stiffness matrix, and is therefore also symmetric [32].

5.1.2 Global stiffness

As for regular beam theory, the global stiffness matrix is made by assembling the local element stiffness matrices with respect to their respective Degree Of Freedom (DOF), which has been converted to fit the global coordinate system. The conversion to the global coordinate system is established in eq. (5.2).

$$[K_{e,R}] = [R_e][K_e][R_e]^T = \begin{bmatrix} [R] & 0 & 0 & 0 \\ 0 & [R] & 0 & 0 \\ 0 & 0 & [R] & 0 \\ 0 & 0 & 0 & [R] \end{bmatrix} \tag{5.2}$$

$[R]$ is a 3x3 matrix which is determined through an incremental formulation, where the rotations at each time step is described linearly, which is true at sufficiently small time steps. The advantage of this method is that it is simple to describe mathematically and that no knowledge of the accumulated nodal rotation is needed [32].

5.1.3 Consistent mass

The mass matrix in the corotational beam theory equal to the consistent mass matrix of regular beam theories. It is obtained by integrating the deformation matrix, which contains the shape functions.

$$[M] = \int_0^L [N]^T [N] \rho A dx \tag{5.3}$$

The mass matrix is then rotated and assembled to the global mass matrix like the stiffness matrix [16]

.

5.2 Nonlinear Newmark integration

As for the linear Newmark beta-method, the nonlinear Newmark integration is an implicit method, where the motion of the beam elements are calculated through the mass, stiffness, and damping, the degrees of forward weighting, and the forces acting on the beam. Because the nonlinear effects are deformation related, it is preferable to find the initial deformation through the equation of motion, and make predictions of the initial acceleration and velocities. Since the equation of motion is satisfied in the time increments, the forces on the beam elements can be found through eq. (5.4).

$$f_{n+1} = [M]\ddot{u}_{n+1} + g(u_{n+1}, \dot{u}_{n+1}) \tag{5.4}$$

Where $[M]\ddot{u}_{n+1}$ represents inertia forces, and $g(u_{n+1}, \dot{u}_{n+1})$ is an expression for the internal forces. To solve the nonlinear equations the Newton-Raphson's iterative linear approximation method is used [32].

5.2.1 Newton-Raphson method

When encountering nonlinear dynamics, it is in many cases appropriate to consider an iterative linear approximation. Such an approximation can be obtained using the Newton-Raphson method. It works by applying the desired loads incrementally, and solve the equilibrium equations in each iteration, which can be done by using a linearized set of equations as seen on Figure 5.3.

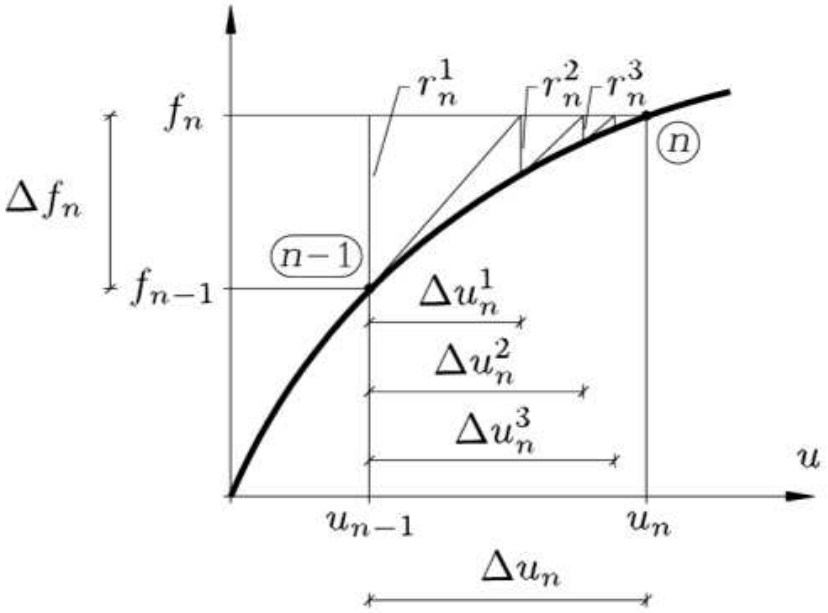

Figure 5.3: Illustration of the approximation method used in the Newton-Raphson method [32].

The linear approximation of the force, results in a deviation in the force, compared to the deformation, and this deviation is called the residual force.

$$r = f_{n+1} - [M]\ddot{u}_{n+1} - g(u_{n+1}, \dot{u}_{n+1}) \tag{5.5}$$

In each iteration it becomes smaller until a limit is reached and the iterations stop. Due to the nature of the method, common problems are numerical inefficiency, and the risk of infinite iterations, even with a limit on the residual [32].

5.2.2 Determination of motion components

In each iteration the linear increment of the physical forces are found with an ever decreasing residual. As eq. (5.5) shows, the residual determined from the equation of motion, and through differentiation the modified tangent stiffness matrix can be determined.

$$[K_{eff}] = -\frac{dr}{du} = [K] + \frac{\gamma}{\beta\Delta t}[C] + \frac{1}{\beta\Delta t^2}[M] \tag{5.6}$$

Rearranging eq. (5.6) yields the change of displacement happening in each iteration.

$$\delta u = [K_{eff}]^{-1}\delta r \tag{5.7}$$

With the displacement increment determined, a new motion component can be determined through eq. (5.8) to (5.10).

$$u_{n+1} = u_{n+1} + \delta u \tag{5.8}$$

$$\dot{u}_{n+1} = \dot{u}_{n+1} + \frac{\gamma}{\beta\Delta t}\delta u \tag{5.9}$$

$$\ddot{u}_{n+1} = \ddot{u}_{n+1} + \frac{1}{\beta\Delta t^2}\delta u \tag{5.10}$$

These are the new motion components to be used in the next time step, unless the residual is determined to be too large. Then the new motion components are used again in eq. (5.5) in a new Newton-Raphson iteration, until a sufficiently small residual is achieved [32].

5.3 Implementation of structural damping

To accommodate for the loss of energy due to friction, and to avoid numerical instabilities, damping is introduced in SOFIA. This is done through Rayleigh damping, and numerical damping.

5.3.1 Rayleigh damping

Viscous damping, which Rayleigh damping is categorized as, is proportional to the velocity of the structure. It represents the dissipation of energy from vibrations in a fluid or gas, and it is implemented in SOFIA as part of the internal forces when calculating the residual in eq. (5.5). Rayleigh damping is sometimes also called proportional damping, since it is proportional to the global mass matrix and global stiffness matrix of the structure as shown in eq. (5.11).

$$[C] = \alpha[M] + \beta[K] \tag{5.11}$$

α and β are the mass proportional and stiffness proportional damping coefficients respectively, and together with the structural eigenfrequencies establish the damping ratios of the corresponding eigenmodes.

$$\eta = \frac{1}{2}\left(\frac{\alpha}{\omega} + \omega\beta\right) \tag{5.12}$$

It is clear from eq. (5.12) that mass proportional damping has a greater influence at low modes, and that stiffness proportional damping has a greater influence at higher modes. This is important to keep in mind when considering corotational beams and the incorporated rigid body motions. Rigid body motions with regards to offshore structures typically oscillate at low frequencies, which means for such motions the mass proportional damping is dominant. Stiffness proportional damping is however also important if the offshore structure is supported by tension legs, which without damping might behave like a guitar string and oscillate at very high nonphysical frequencies [16].

5.3.2 Numerical damping

Many numerical solution methods, like the nonlinear Newmark integration, incorporate numerical damping. This type of damping is nonphysical and therefore should not have any effect on the general behavior of a structure, when conducting dynamic analyzes. It can however be used to dampen numerically infused nonphysical oscillations and unimportant higher order eigenmodes, which otherwise would disturb the computation process. It is introduced, as shown in eq. (5.8) to (5.10), to determine the new motion components of the next time step through the integration parameters β and γ. The values for β and γ can greatly influence the stability of the numerical integration if they are chosen too low, however this source of error is easily avoided when using an implicit solver, which define lower limits for these parameters.

$$\gamma \geq \frac{1}{2} \qquad \beta \geq \frac{1}{4}\left(\gamma + \frac{1}{2}\right)^{\frac{1}{2}} \tag{5.13}$$

The result of increasing the integration parameters above the lower limit is the effect of numerical damping. In SOFIA, as is equal to the method in the commercial software ANSYS Inc., numerical damping is introduced by adding a numerical damping ratio to the integration parameter γ. Care should be taken when using this sort of damping, since misuse can cause errors in both oscillation amplitudes and periods [16].

5.4 Structural design of mooring lines

Unlike regular beam elements, which through its twelve DOF incorporates axial, bending, and torsional stiffness, the mooring lines are modeled as a bar with no compressional stiffness. This is in SOFIA implemented by using corotational beams with moments of inertia set equal to zero. This negates bending stiffness, and by using a sufficient amount of elements, cause the mooring lines to fold together, due to the lack of bending stiffness between elements.
At the connection between structure and mooring line, the translational DOF are coupled, as done for any other connected elements, however the rotational DOF are kept decoupled. This is to avoid unrealistic rotations of the mooring line elements connected to the structure. Physically this means that each mooring line is connected to the structure through a hinge.

6

Experimental validation

The development of SOFIA, as well as the associated stream function theory add-in, has as aforementioned successfully been validated against Ocean Commands in ANSYS Inc., with the purpose of ensuring the reliability. To demonstrate utilization in realistic scenarios, the following chapter is dealing with numerical simulation of experimental seakeeping tests.

All conducted numerical simulations are based on experimental models associated with the TLB B foundation. Since the considered experiments are made with the requirement of making all the experimental models big enough to easy be produced and verified by numerical simulations, a scaling factor of 1:40 is used as mentioned in chapter 2.

As a part of the numerical calibration, a parametric study of the hydrodynamic coefficients is considered for the purpose of investigating their influence on the dynamic response.

Figure 6.1: Test facility IFREMER, France [41].

The chapter is divided in to three main sections, where the first part is considering numerical modeling of the experimental models. The second part is considering a pre-study with the purpose of investigating the influence of the hydrodynamic coefficients. The last section is considering the verification study.

6.1 TLB Simple (S) and TLB B

Besides the experimental models of TLB B, a reference model namely the TLB S (Simple) has been developed.

TLB S is made as a pipe, produced in PVC, with a constant cross section of 250mm and a wall thickness on 5mm. The geometry, only consisting of substructure, simplify the model and reduce the sources of error. The model is therefore ideal to be used in the parametric study and in the verification of the routine, as it is deemed numerically easier to achieve a reasonable fit with the experimental results [39].

Since the TLB S is only designed as a reference model it cannot be used for further full-scale simulations, required for the mooring line fracture analysis. As a result, the knowledge obtained from the parametric study and the verification of the TLB S, is used in numerical calibration of the TLB B.

Experimental TLB B
As mentioned and shown in chapter 2, the TLB B is circular shaped as the TLB S, but in order to reduce the wave loads, it is designed with a narrower section around the Mean Sea Level (MSL). Since the experimental TLB B model is identical to the already mentioned full-scale model, it is not explained in details in this section. In general the lower diameter is 0.29m, the upper diameter 0.15m, and with a conical section to connect the upper and lower section. The lengths of the three sections are from the top 0.88m, 0.12m and 0.62m [39].

Experimental wind turbine
On top of the experimental TLB B foundation is an experimental wind turbine located. The wind turbine is designed with a view to the academic 5 MW NREL wind turbine, but down-scaled and simplified for the purpose of easier comparing experimental results to numerical results. The wind turbine is therefore consisting of a tower with an lumbed mass on top, to simulate the weight from the rotor and nacelle [39].

Numerical modeling of the TLB S and the TLB B

In order to reproduce the experimental results, the two structures equal to their experimental counterparts are numerically modeled. Figure 6.2, shows a nodal discretization of the two models and the wind turbine. The numbering in Figure 6.2 is therefore defining the number of the node. From the discretization of the two foundation models, it is seen that the nodes around the top and the bottom is placed close to each other, which is for taking the top and bottom cap in to account [39].

Since the wave elevation is time dependent, a fine beam discritization is needed in the area of the wave elevation, in order to ensure accurate depiction of the buoyancy/gravity force relation. As the particle kinematic magnitude decrease exponentially with the depth, and since local deformations of the entire TLB is considered, a sufficient discretization is also needed along the entire body of both TLB.

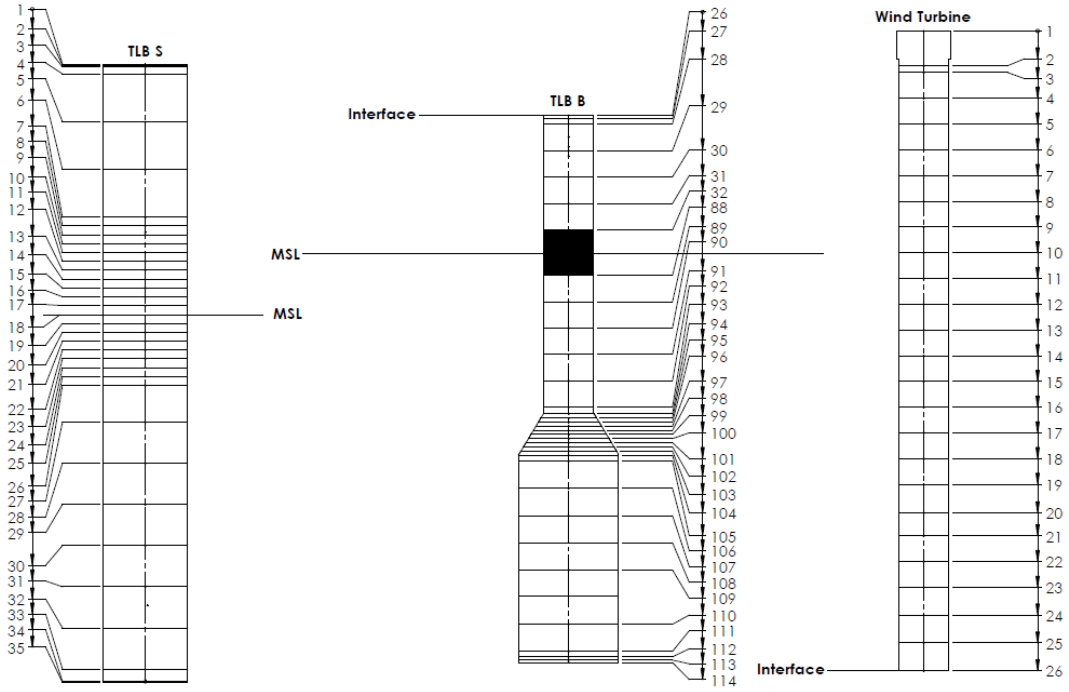

Figure 6.2: Nodel discretization of TLB S, TLB B and the Experimental Wind Turbine.

In the digital version an Excel document is found, which connects nodes and elements with the dimensions of the foundations.

6.1.1 TLB S and TLB B simulation parameters

Table 6.1 are used to give an overview in the model parameters.

Properties	Units	TLB S	TLB B
Foundation Density	$[\frac{kg}{m^3}]$	1138	1550 (D1), 3100 (D2), 2900 (D3)
Wind Turbine Density	$[\frac{kg}{m^3}]$	-	1200
Mass Proportional Damping	$[s^{-1}]$	0.5	0.05
Stiffness Proportional Damping	$[s]$	0.005	0.005
Numerical Damping	$[-]$	0.1	0.1
Timestep	$[s]$	0.004	0.004

Table 6.1: Model parameters.

As previously mentioned, the TLB B is designed such it is divided into three sections. The bottom section (D3) and the conical section (D2) is made in aluminum and the top section (D1) in PVC. The experimental wind turbine is produced Poly carbonate with the density stated in 6.1.
The damping coefficients are determined in the later verification of SOFIA, it should be noted that the numerical damping is set high as the necessity to avoid numerical instabilities.

6.1.2 Numerical modeling of experimental setup

The TLB experiments are performed in the deep water wave basin at IFREMER's facilities in Brest, France. The dimensions of the basin are 50x12.5m and a depth range from 10 to 20m.

Due to the need for absolute control of mooring points and the opportunity of fixing the mooring lines at a significantly shallower depth of a few meters, a surface mounted and pretensioned structure has been used in the experiments [39]. To simplify the numerical model, dynamic effects from the pretensioned structure, are not taken in to account and the focus area is therefore delimited to the red square in Figure 6.3. As a result the properties of the mooring line setup it included in the numerical modeling of the mooring lines.

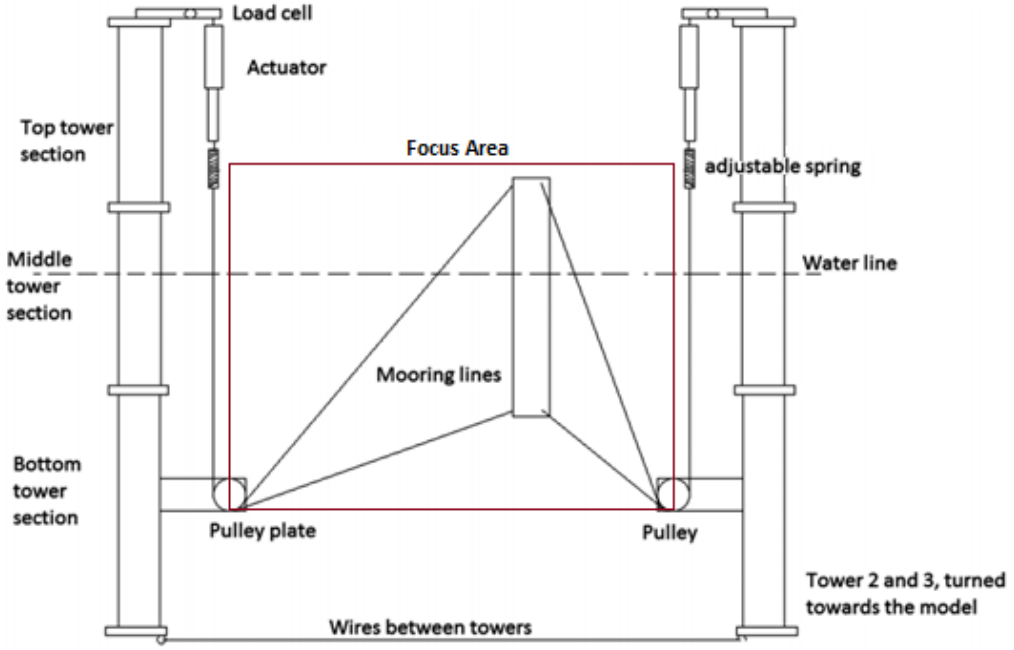

Figure 6.3: Test facility setup.

Both foundations are kept stationary through six mooring points (three in the top and three in the bottom) mounted around the cylinder with an equally space of 120° in between. The mooring points are located as shown in Table 6.2.

Mooring Points	Node No.		Distance from MSL [m]	
	TLB S	TLB B	TLB S	TLB B
Upper	4	23	0.717	0.679
Lower	33	111	-1.054	-1.184

Table 6.2: Numerical mooring points.

It should be mentioned that experimentally, the mooring point is consisting of a bracket in which carabiners connect the mooring line and the foundation structures. The brackets will lead to eccentricity, but since the distance from the center axis to the mooring

point is small compared to the rest of the structure, it is assumed that the influence is negligible. To give a correct description of the mooring point connections consisting of carabiners, which are modeled as hinges. The structural behavior is discussed in chapter 5.

The mooring lines between the mooring points and the pretensioned structure are consisting of a 1mm steel wire and an adjustable spring, which in the end is connected to a linear actuator. To numerically describe this setup, the mooring lines are modeled with an axial stiffness corresponding to those shown in Table 6.3, consisting of the resulting stiffness of the wire and the spring.

Since the mooring line setup is consisting of three top and bottom mooring lines, two pulleys in each column are mounted side by side, to guide wires to the support in the linear actuator. This implies a small difference in support coordinates as shown in Table 6.3. The mooring line stiffness written in Table 6.3 is equal for the two concepts.

Mooring line coordinates	Number	X[m]	Y[m]	Z[m]	Line stiffness TLB B & S[N/mm]
Lower line	1	3.835	0.030	-1.868	2.899
Lower line	2	-1.891	-3.336	-1.868	2.842
Lower line	3	-1.943	3.306	-1.868	2.870
Upper line	4	3.835	-0.030	-1.868	2.341
Upper line	5	-1.943	-3.306	-1.868	2.320
Upper line	6	-1.891	3.336	-1.868	2.299

Table 6.3: Mooring line coordinates and mooring line stiffness [39].

To avoid an offset in the numerical model, as consequence of that the buoyancy elevates the foundation structure when the analysis starts, pretension in the mooring lines are implemented. The pretension is estimated by a simple simulation, where only gravity and buoyancy are the present loads. The observed displacements are converted to internal forces always present in both TLB. This also ensures that the correct equilibrium position is kept in still water.

Further experimental details about the test facility, error sources, and results obtained by use of the test facility, can be seen in the associated paper [39].

6.2 Parametric study of time step size

By conducting a transient simulation it is necessary to weight accuracy and analysis time against each other. A high time step size will reduce the number of simulation points and the simulation time, but simultaneously produce a poor result [44]. To ensure enough simulation points to produce valid results, an adequate discretization must be chosen.

Through conducted simulations it has been experienced, that the time step size is influenced by the hydrodynamic coefficients, and therefore a time step size of 0.004 seconds is assumed. The time step size is used in the parametric study of hydrodynamic coefficients and in the verification study of the TLB S and TLB B. To check if the time step size is valid to use, a convergence study is conducted with the hydrodynamic coefficients estimated in the verification study.

The convergence study of the time step size is based on the structural displacements in the top node in surge, sway, and heave respectively. All simulation properties are equal to those used in the verification study of the TLB S and TLB B.

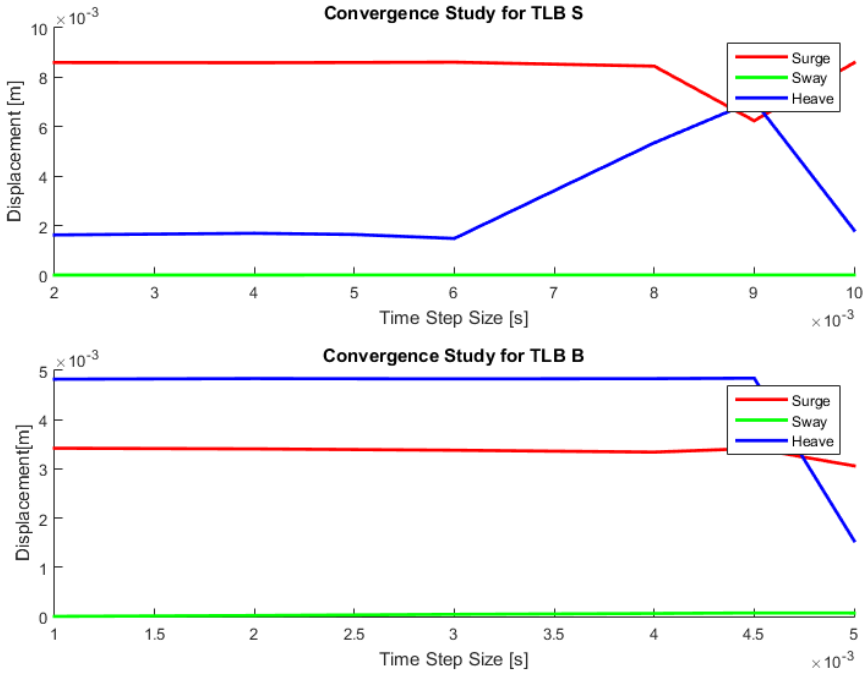

Figure 6.4: Time step convergence study.

From the convergence plots it is seen, that utilization of the assumed time step size of 0.004 seconds, or lower produces valid results.

6.3 Influence of hydrodynamic coefficients

The Morison equation is semi-empirical, dependent of the hydrodynamic coefficients; drag, inertia, and added mass respectively. The coefficients are typically determined by use of experiments. To better understand the hydrodynamic coefficients influence, a parametric study through response behavior is established.

The parametric study is conducted with basis in the TLB S, due to that the simple geometry reduces possible sources of error that might influence the study. The study considers the two different analyzes:

- An analysis wherconducted, where an external force of -15N or -35N is applied on top of the TLB S. The displacement caused by the 15N force is applied separately in the vertical direction, while the 35N force is applied in the horizontal direction.
- The second conducted analysis is considering the influence of hydrodynamic coefficients, while its dynamic responses are influenced by waves. The investigated wave scenario has a period of 1.58s, a wave height of 0.13m, and a water depth of 10m, resulting in a KC of 1.72.

6.3.1 Initial setup and hydrodynamic coefficients

To establish a study that is as wide as possible, the hydrodynamic coefficients on the structure and the mooring lines can be adjusted separately. Figure 6.5, defines how the hydrodynamic coefficients are investigated.

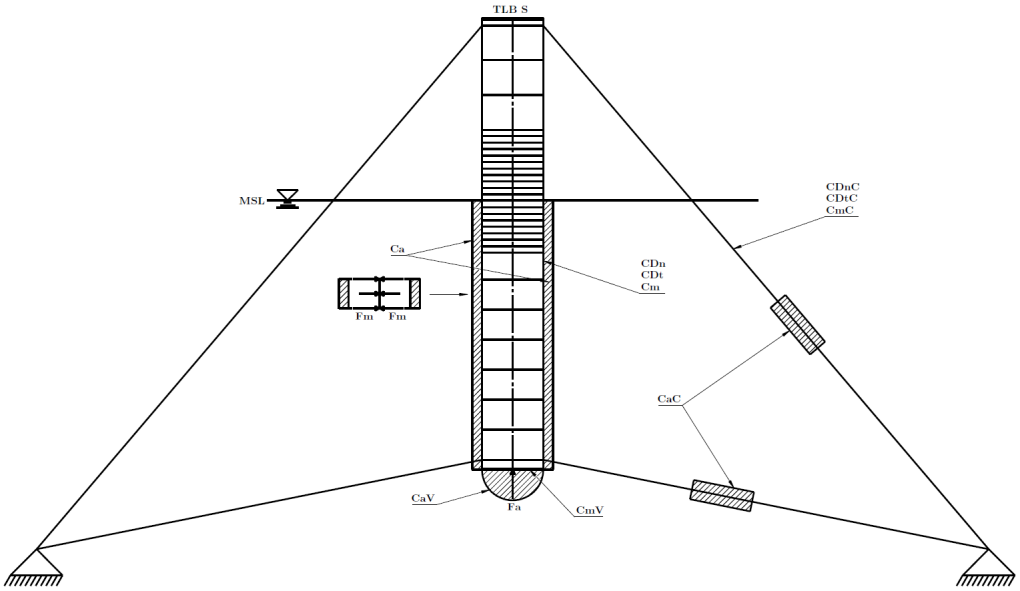

Figure 6.5: Setup of hydrodynamic coefficients for the TLB S.

The added mass is applied to account for the motion of the surrounding water, due to structural accelerations. To reduce the complexity, it is assumed that the surrounding fluid is moving with the structure [50]. The added mass is along the structure applied as a distributed force, normal to each element and on the bottom cap, as a point force in the bottom node. Instead of adding the added the mass in the mass matrix, it is multiplied with the structural acceleration, in order to establish a force contribution as shown in eq. (6.1) [4, 42].

$$\begin{aligned} F_a &= \rho C_a \pi r^2 L \\ F_{a,bottom} &= \rho C_a \frac{2\pi}{3} A_s \end{aligned} \tag{6.1}$$

The added mass contribution in the horizontal direction is described as a cylindrical shaped area around the structure, which together with the other hydrodynamic forces i.e. drag and inertia mass, is calculated in the nodes and in the integration points, as shown in the detail of Figure 6.5. The volume of the surrounding fluid at the bottom cap is described as a hemisphere [42].

Hydrodynamic coefficients are on the mooring lines applied in the same manner as for the main structure. Before the analysis is started, arbitrary initial hydrodynamic coefficients are chosen as seen in Table 6.4.

CDn	**CDt**	**Cm**	**CaV**	**Ca**	**CmC**	**CDnC**	**CDtC**	**CaC**
0.5	0.005	1	0	0	1	0.5	0.005	0

Table 6.4: Initial hydrodynamic coefficients.

6.3.2 Inertia coefficient influence

First investigated coefficient through the present study is the inertia coefficient, and since the inertia is dependent on the fluid velocity, it is only of influence while waves are included in the analysis.

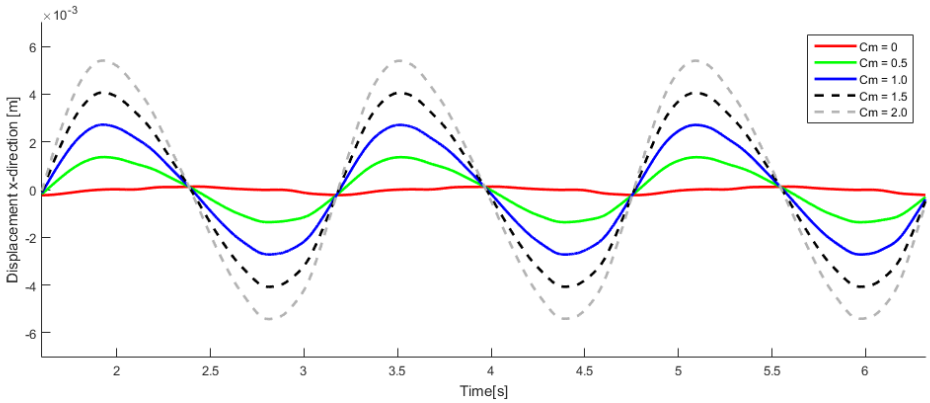

Figure 6.6: Influence from the inertia coefficient

By evaluating Figure 6.6, it is seen that the inertia coefficient have quite a large influence on the dynamic response, which corresponds well with the calculated KC of 1.72 and the Figure 4.4 in chapter 4. Due to that the wave load case is inertia dominated and the inertia coefficient is of large influence, the influence of inertia is investigated in the vertical direction. The inertia force is applied as a vertical point load like the added mass. In contradistinction to the added mass, inertia is as aforementioned dependent of fluid velocity, which have that consequence that it is only influencing the structure, while the particle kinematic is pushing upwards on the end cap. Figure 6.7 shows the influence of inertia in the vertical direction.

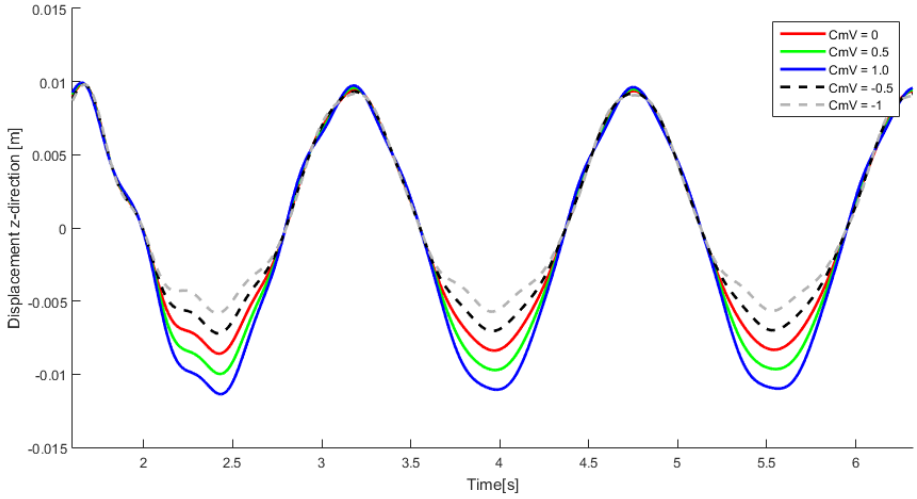

Figure 6.7: Influence from vertical inertia coefficient.

It can be observed from Figure 6.7, that inertia as in the horizontal direction has quite a large influence on the dynamic response. The influence increases the negative amplitude corresponding to the time, where the structure is in the wave through, unless the inertia

coefficient is set negative, which is opposite to the expectations. As mentioned in the model setup, the vertical inertia contribution is applied as a point load on the bottom cap as the added mass, when the particle acceleration exposed to the cap is positive. It therefore seems strange that the amplitudes are increasing. Although this study shows the opposite results than expected, the contribution will be implemented in the further validation studies, as it may be important in order to fit the results to those measured in the experiment.

6.3.3 Drag coefficient influence

As mentioned in the model section, drag is applied both normal- and tangential to the element.

Due to the horizontal motion, the structure is exposed to normal drag, but as a consequence of that the wave load case is inertia dominated, the drag should be of minor influence. This is also shown in Figure 6.8, where the amplitude is only changing slightly. Note that due to the velocity dependents, the response plot becomes steeper in the middle. This accommodates the expectation that the drag coefficient is dependent on the structural roughness.

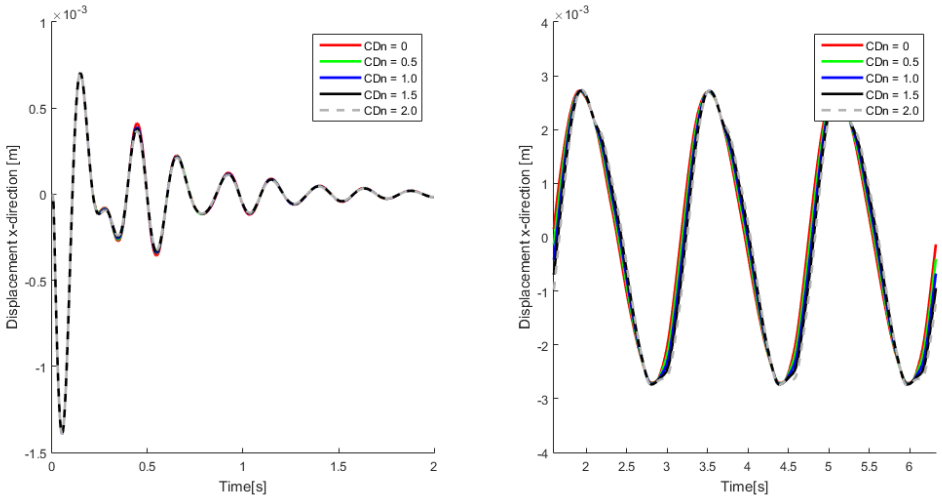

Figure 6.8: Influence from the normal drag coefficient.

Similar analyzes of the drag coefficient is made in decay tests. Since inertia has no influence in the decay tests only drag and added mass can be used in the calibration, which makes it possible to better determine they values, when inertia is dominant. As expected the effect of drag is a decrease in amplitudes.

It is experienced that a high tangential drag coefficient causes the model to be unstable, which is expressed by the spikes in the wave response plot in Figure 6.9 to the right. Because of this, tangential drag was set very low, and instead damping was used to replace the reduction in amplitudes.

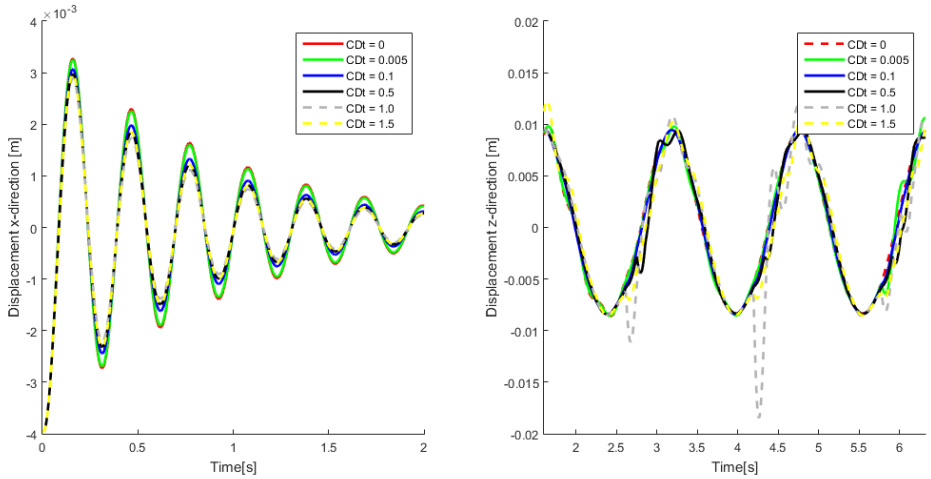

Figure 6.9: Influence from tangential drag.

6.3.4 Added mass coefficient influence

In order to include the added mass contribution, the Morison equation is rewritten to the three parted version. The following equation is stated per unit length only for the horizontal directions [4].

$$\{\frac{F}{L}\}_{y,z} = \rho C_a A(-a_a) + \rho C_m A a_f + \frac{1}{2}\rho C_d D(v_f - v_s)|(v_f - v_s)| \tag{6.2}$$

Since the added mass force contribution is dependent on the structural accelerations, the added mass coefficient is expected to be out of influence when waves are applied. If waves are applied, the structural acceleration will be dominated by the motions of the waves. Therefore it is mostly interesting to investigate the influence of the added mass coefficient in the decay test. To ensure that the expectations are correct Figure 6.10 is evaluated.

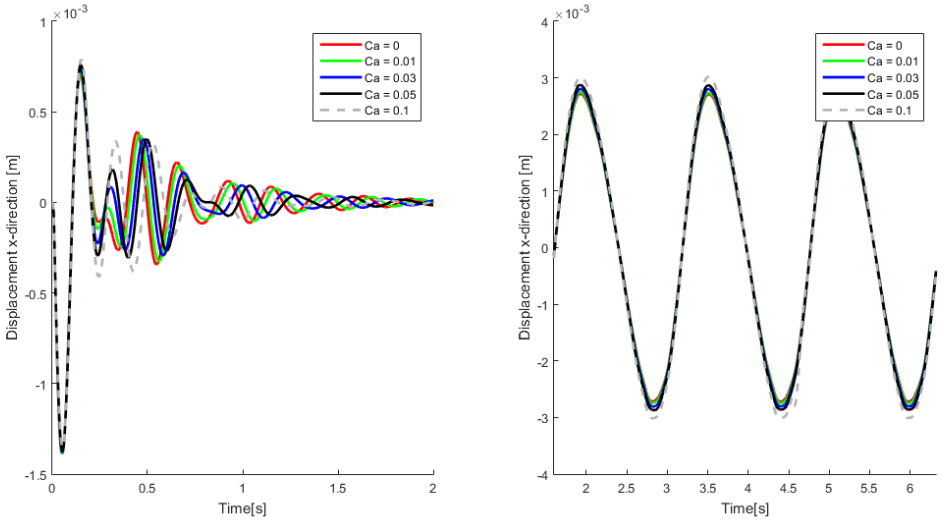

Figure 6.10: Influence from the horizontal added mass coefficient.

Figure 6.10 to the left, shows the influence from added mass in the horizontal direction by

conducting a decay test. The surge response behavior is not as expected, due to the shifting amplitudes. However the added mass influence shows that the periods are extended as a result of a higher added mass coefficient. The same effect is occurring vertically and due to the more clean oscillation it is easier to see. Figure 6.10 to the right show that the only relevant effect of added mass is the influence on the amplitudes.

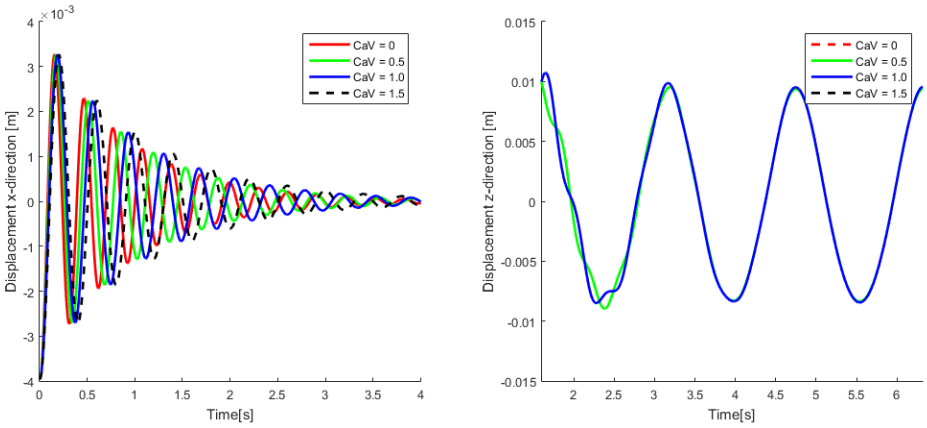

Figure 6.11: Influence from the vertial added mass coefficient.

The reason for the increased periods, is that the added mass coefficient changes the structural eigenfrequency. Normally when structural eigenfrequencies are considered, it is in dry conditions, but due to the investigation of offshore structure, the influence from the water has to be taken in to consideration. Decay tests are conducted in two phases. Phase one in dry conditions and phase two in wet conditions, which implies the possibility to estimate the stiffness and the oscillation frequency.

$$\omega_d = \sqrt{\frac{k_{dry}}{m_{dry}}} \tag{6.3}$$

$$\omega_w = \sqrt{\frac{k_{wet}}{m_{submerged} + m_a}} \tag{6.4}$$

Eq. (6.3) is the oscillation frequency of the structure in dry conditions and eq. (6.4) in wet conditions, where k_{wet} is the stiffness of the structure in water and $m_{submerged}$ is the mass of the submerged body [31].

Therefore if the added mass coefficient is increased, the oscillation frequency in water is decreased, as is the structural eigenfrequency. This implies larger periods in the decay tests.

6.3.5 Influence from hydrodynamic coefficients on mooring lines

Associated with the parametric study, it is investigated whether it is necessary to decouple the hydrodynamic load calculations on the mooring lines and calibrate separate hydrodynamic coefficients. All results showed no or minor influence, and it is there chosen not to focus further on the hydrodynamic coefficients in the mooring lines. In further

simulations, hydrodynamic coefficients will be adjusted equally with those from the structure. The digital version contains the results and properties associated with the conducted study.

6.4 Verification of SOFIA

The experimental results from the two experiments were obtained by using a PDF digitizer, which could accurately evaluate the coordinate system and therefore pinpoint the correct coordinates of the data. This was for the TLB S and the TLB B done through the paper [38].

6.4.1 Considered experimental load cases

Through the following verification study, it is decided to focus on one experimental wave load case from the previously mentioned [38], namely load case 9. Experimentally both the TLB S and TLB B are exposed to load case 9. The wave load case is consisting of a regular waves with a wave height of 0.13m, a period on 1.58s and a water depth equal to depth of the test basin, 10m.

Experimental wave load case	$\frac{h}{gT^2}$	$\frac{H}{gT^2}$	Required wave theory
9	0.407	0.0053	Stokes 5th order or stream function 3rd order

Table 6.5: Wave Validity Properties.

Based on the gravitational acceleration and the input values from load case 9, the wave may valid be described by Stokes 5th order theory or stream function 3rd order wave theory, as shown in the wave applicability plot Figure 6.12.

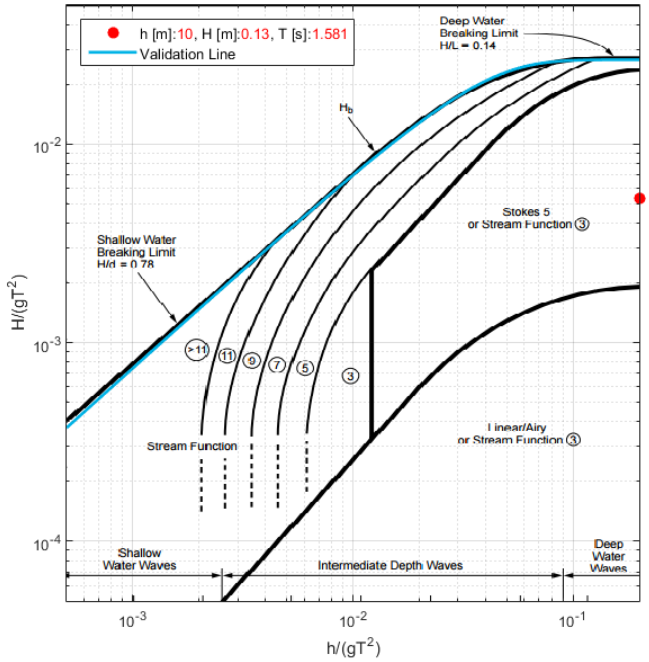

Figure 6.12: Wave theory applicability of load case 9

When the wave data is inserted in the figure, it is according to the x-axis out of the range. To still show the location on the y-axis, the x-coordinate is set equal to the maximum value on the x-axis, 0.2.

6.4.2 Hydrodynamic setup of TLB B

The present section is considering the hydrodynamic model setup with regards to the verification study. The model setup for the TLB S is previously mentioned in section 6.3, associated with the parametric study of the hydrodynamic coefficients. Since the study is a prestudy to this section, the hydrodynamic model setup is already based on the experimental model, and is not explained here. As a result the present section will only consider the hydrodynamic model setup of the TLB B.

The hydrodynamic loads acting on the TLB B are applied in almost the same manner as for the TLB S, due to the similar geometry. Figure 6.13 shows in which areas, the hydrodynamic coefficients can be adjusted in order to calibrate the associated loads.

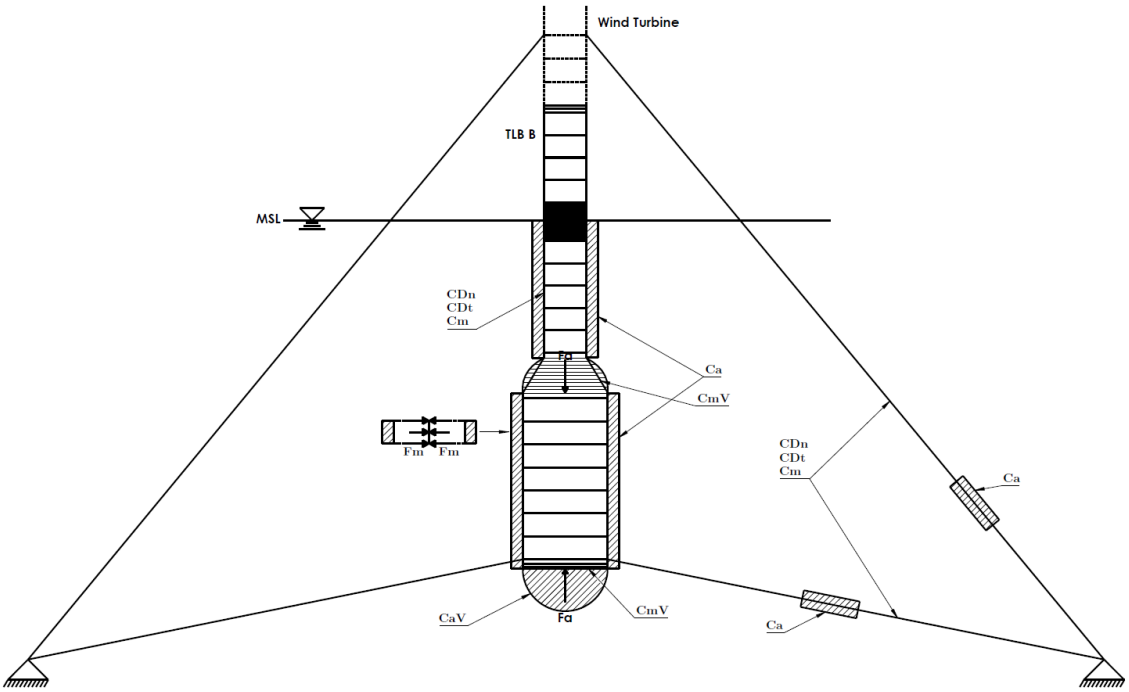

Figure 6.13: TLB B model setup.

Differently from the TLB S model, the TLB B has as aforementioned a conical section between the upper and lower section, which implies some changes in the hydrodynamic model setup. For this model the added mass is applied as a point force in node 106, which is the lowest point in the conical section. The added mass force is described as

$$F_{a,con} = C_a \rho (\frac{2\pi}{3} {r_{bot}}^3 - \pi {r_{top}}^2 r_{bot}) A_s \tag{6.5}$$

It means that the added mass is described as a hemisphere, where the volume of the TLB B upper section is subtracted from the added mass volume, as seen on Figure 6.14. As for the bottom of the TLB B, the added mass was implemented in the same way as for the TLB S.

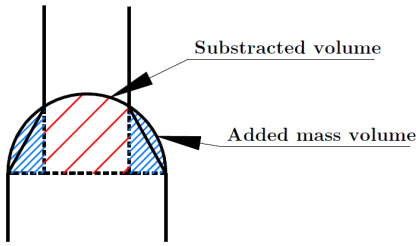

Figure 6.14: Added mass volume of the conical part of the TLB B.

Since inertia had a great contribution in the vertical direction in the TLB S parameter study, this is also taken into consideration in the TLB B model. The vertical inertia load contribution is as the added mass acting on the conical section, due to that it is dependent on the vertical fluid acceleration. This is as well acting on the bottom. To establish the correct distribution on the conical section, it is necessary to only include the distribution, when the particle acceleration is negative, and positive for the bottom cap.

6.4.3 TLB S comparison

The results from the experiments with the TLB S include two decay tests, as seen in section 6.3, and wave case 9, as seen in section 6.4.1.
In order to calibrate the numerical model to both fit the experimental results, damping and hydrodynamic coefficients were adjusted to create the lowest error. The hydrodynamic coefficients can be seen in Table 6.6.

Parameters	Units	Value
Added mass coefficient	[−]	0.2
Vertical bottom added mass	[−]	0.6
Normal drag coefficient	[−]	0.5
Tangential drag coefficient	[−]	0.005
Inertia coefficient	[−]	3.3

Table 6.6: TLB S hydrodynamic coefficients.

The results from both experiment and simulations is seen on Figures 6.15 to 6.18.

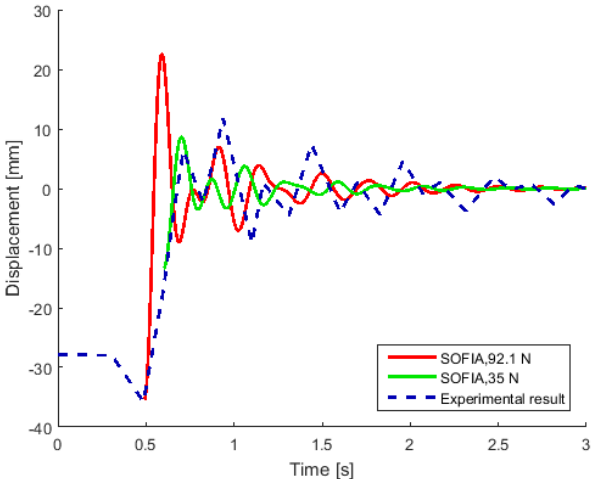

Figure 6.15: TLB S horizontal free decay test.

The horizontal free decay test yielded poor results. As it is clearly seen, the use of 35N is not enough to create an initial displacement of 35 mm, and the following response only fit in the very first period. The required force to create the correct initial displacement was found to be 92.1N. This, however, created an initial response which does not at all fit the experiment. Interestingly, the following response from the 92.1N seem to follow the experimental decay test to a lesser degree, and it may fit better if larger amplitudes could be achieved. Though this is not possible, because the displacements are very small, which allow the numerical instabilities to have a significant effect on the result.

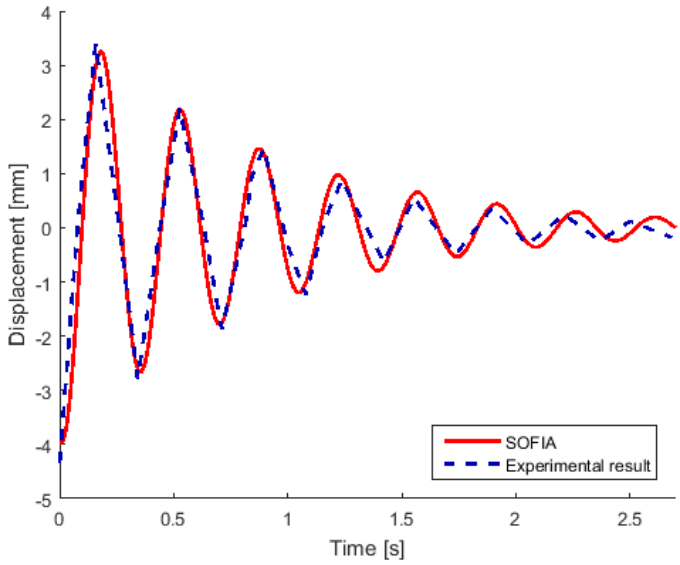

Figure 6.16: TLB S vertical free decay test.

A very good fit is found in the vertical decay test. The amplitudes are almost perfect throughout the analysis and the oscillation periods only deviate in the end.

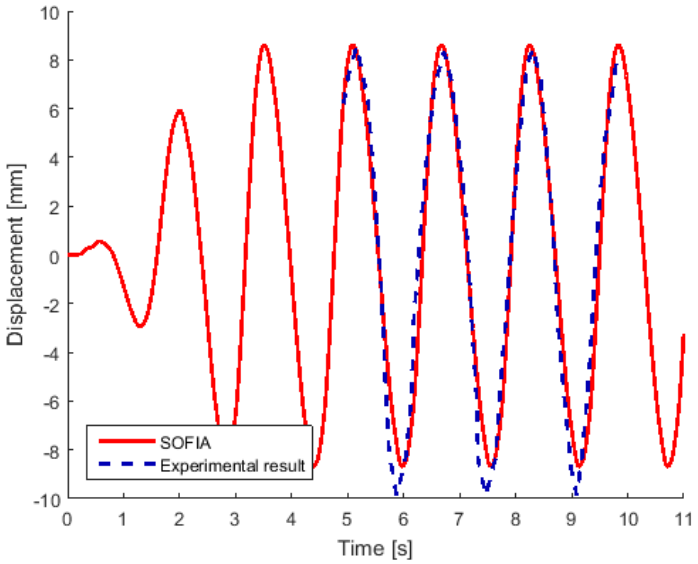

Figure 6.17: TLB S surge displacements in wave load case.

The surge displacements fit fairly well. Only a slight deviation in amplitude is present due to the experimental results exhibiting a large displacement in the direction of the wave, which could not be replicated in SOFIA.

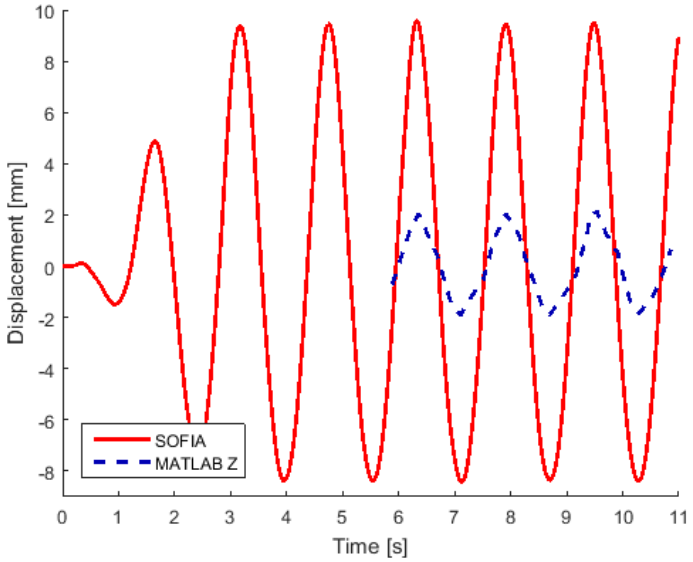

Figure 6.18: TLB S heave displacements in wave load case.

The heave displacement is for the TLB S by far the largest source of error in the numeric analysis. The displacements are very small, which is hard to replicate due to the dominant forces being gravity, buoyancy, and the internal forces in the mooring lines, all of which are unchangeable factors. When no hydrodynamic forces are present, the surge displacements yield about the same results as seen on Figure 6.18. The only thing which could reduce the displacements were damping, added mass, and tangential drag, but the magnitudes necessary were so high that all other displacements were irreversible reduced to such an extend, that they became incomparable with their respective experimental results.

6.4.4 TLB B comparison

The TLB B concept was tested the exact same way as the TLB S, with two decay tests and the load case 9 wave scenario.
In order to calibrate the numerical model to both fit the experimental results, damping and hydrodynamic coefficients were adjusted to create the lowest error. The hydrodynamic parameters can be seen in Table 6.7.

Parameters	Units	Value
Added mass coefficient	[−]	0.1
Vertical bottom added mass	[−]	1.5
Normal drag coefficient	[−]	1
Tangential drag coefficient	[−]	0.005
Inertia mass coefficient	[−]	3.6
Vertical bottom inertia mass coefficient	[−]	0.2

Table 6.7: TLB B hydrodynamic coefficents.

The results of the experiments and the comparison with numerical analyzes can be seen in Figures 6.19 to 6.22.

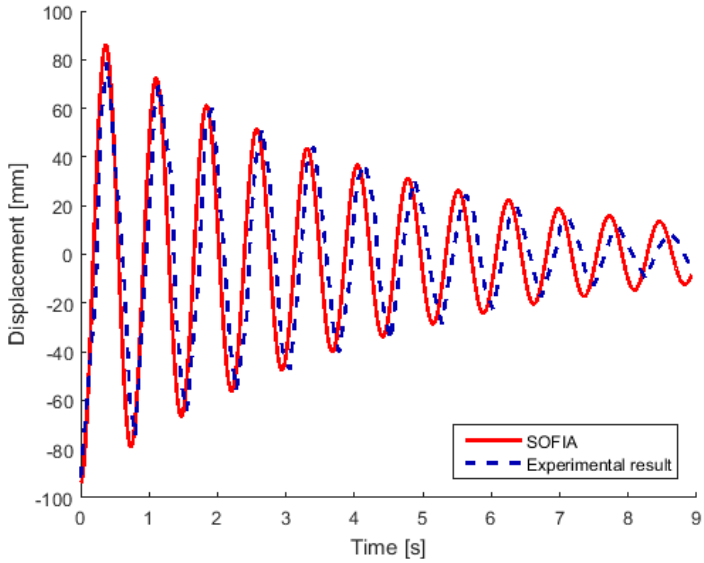

Figure 6.19: TLB B horizontal free decay test.

As is the case for the TLB S, the TLB B required a larger force, than that specified in the experiment. The force used was set to 87N. However with this force, the horizontal decay test for the TLB B, yielded a very good result. Only a very slight amplitude error occur in the end of the analysis and the oscillation period decrease a bit too slowly.

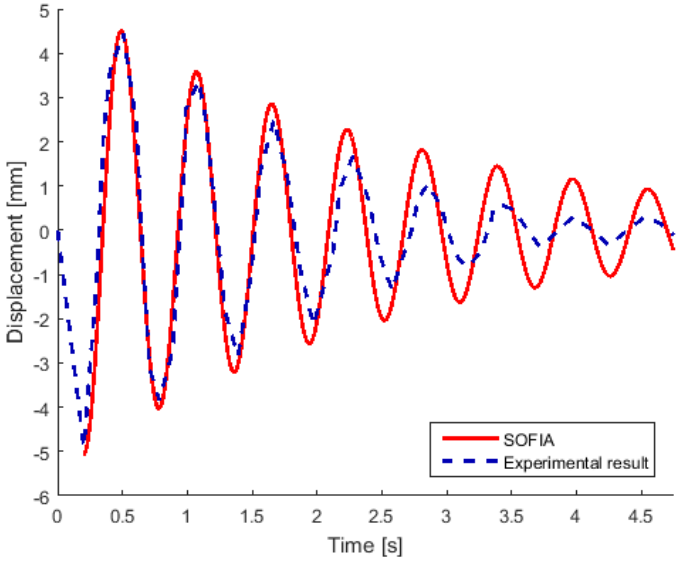

Figure 6.20: TLB B vertical free decay test.

The periods of the vertical decay test fit very well, but the amplitudes decrease too slowly. A better fit could be made by increasing the damping, but this causes errors in the horizontal decay test. Alternatively the tangential drag could have been increased, however this caused instability in the analyzes.

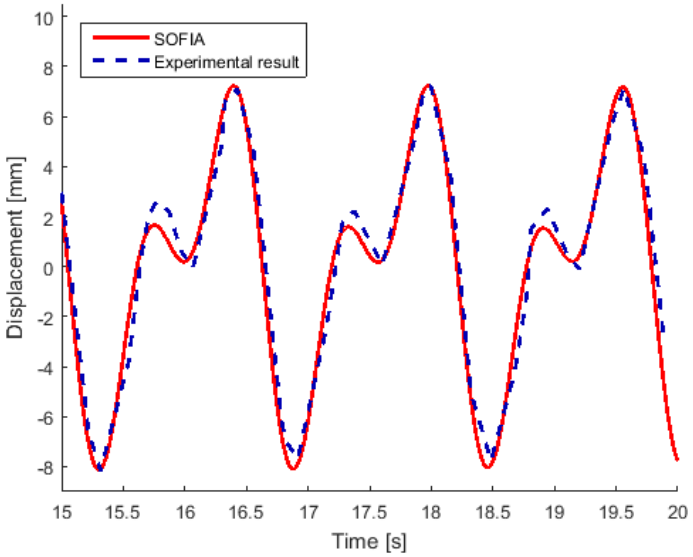

Figure 6.21: TLB B horizontal displacements in wave load case.

A very good fit is achieved in the surge displacements. Only slight errors occur in the amplitudes of the smaller top peaks and the bottom peaks.

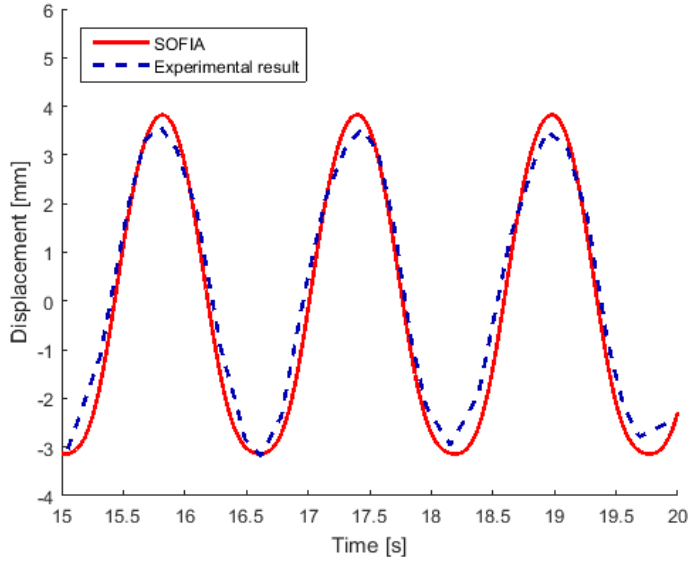

Figure 6.22: TLB B vertical displacements in wave load case.

Unlike the case for the TLB S, the vertical bottom inertia coefficient behaved predictably and reduced the amplitudes. Since the period still follows the change of buoyancy and gravity, which are the dominant forces, a good fit is found in the heave movements of the TLB B.

6.4.5 Comments on Routine Verification

It is clear that the TLB B yield a far better result than the TLB S, despite that the TLB S was supposed to be a simplified version of the TLB B. In the case of the horizontal decay

test, this is because the TLB S is more affected by numerical instabilities. For the heave displacements, the error between having no kinematic forces and the experimental results are much smaller for the TLB B, and in addition the effect from vertical added mass is larger due to the large circumference of the lower section.
Since only slight errors occur in the modeling of the TLB B concept, the numerical model is applicable for further numerical analyzes.

7
Full scale modeling

Using Froude scaling as mentioned in chapter 4.6, the geometry of the conceptualized full size TLB B, which the test model is based on, can be determined. This full size model, if correctly scaled, will behave like its test model counterpart, and since the test model, can be accurately modeled in SOFIA, so can the full size model.

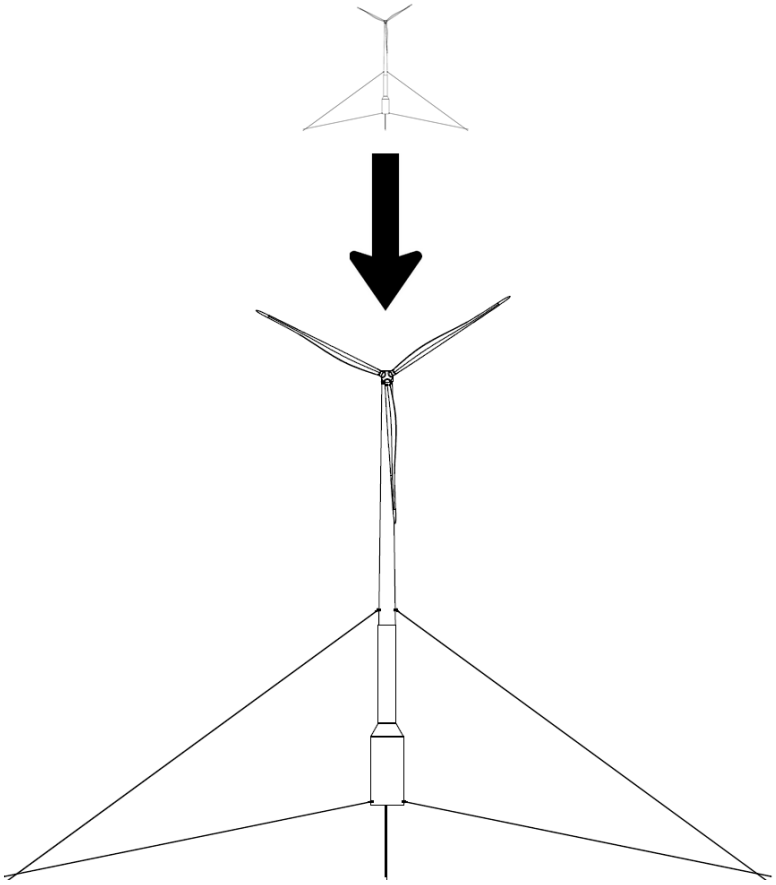

Figure 7.1: Illustration of geometric scaling method

This chapter contains the validation of the scaling method, as well as comments on the geometric composition and choice of modeling materials, which was determined by the experimenters.

7.1 Froude scaling of TLB B test model

The TLB B test model is a downscaled version of a conceptualized wind turbine foundation, with the Academic Wind Turbine 5MW seen in Appendix A, and thus the scaling factors are already set. The geometrical scaling factor is set to 1:40 in both horizontal and vertical direction. Mass density and specific weight are both scaled 1:1. In order to upscale the TLB B test model the scaling factors given in Table 7.1 must be used.

Characteristic	**Dimension**	**Scale ratio**
Geometric		
Length	$[L]$	$1:40$
Area	$[L^2]$	$1:40^2$
Volume	$[L^3]$	$1:40^3$
Kinematic		
Time	$[T]$	$1:40^{1/2}$
Velocity	$[LT^{-1}]$	$1:40^{1/2}$
Acceleration	$[LT^{-2}]$	1
Discharge	$[L^3T^{-1}]$	$1:40^{5/2}$
Kinematic Viscosity	$[L^2T^{-1}]$	$1:40^{3/2}$
Dynamic		
Mass	$[M]$	$1:40^3$
Force	$[MLT^{-2}]$	$1:40^3$
Mass Density	$[ML^{-3}]$	1
Specific Weight	$[ML^{-2}T^{-2}]$	1
Dynamic Viscosity	$[ML^{-1}T^{-1}]$	$1:40^{3/2}$
Volume Elasticity	$[ML^{-1}T^{-2}]$	$1:40$
Stress	$[ML^{-1}T^{-2}]$	$1:40$

Table 7.1: Froude scaling ratios for the TLB B concept

7.2 Validation of scaling method

A major point in conducting small scale model testing is that the full size counterpart will act the same way to the same forces, given that the forces has also been correctly scaled. To see whether the scaling has been done properly, a comparison of the model deflections and full size deflections is made. Load case 9 is used for comparison, which with a 1:40 Froude scaling gives a load case with a wave height of 5.2m, peak period 10s, and a water depth of 400m. The simulation results can be seen in Figures 7.2 and 7.3, where the displacements has been normalized i relation to the maximum deflection of the individual model.

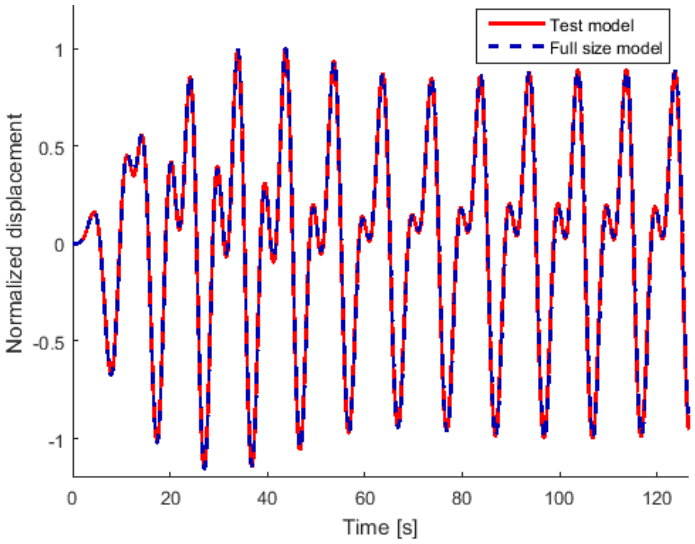

Figure 7.2: Comparison of normalized surge displacements between the test model and full size model, using the upscaled load case 9

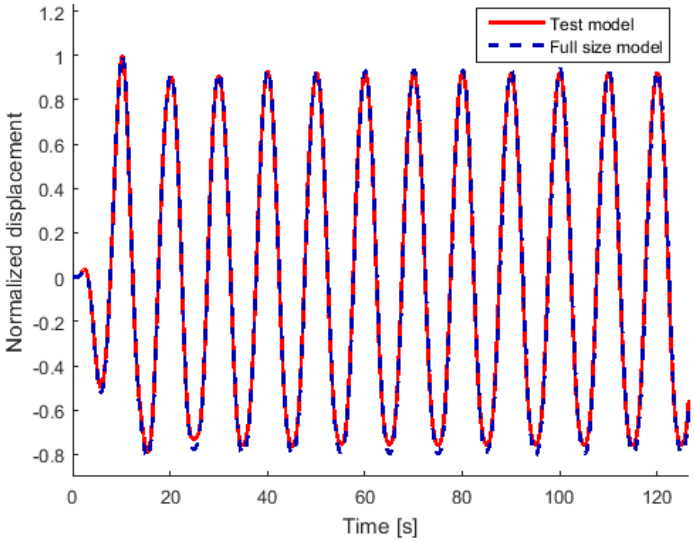

Figure 7.3: Comparison of normalized heave displacements between the test model and full size model, using the upscaled load case 9

It is clear that both heave and surge displacements are approximately the same, and that the Froude scaling method is a valid method. A similar analysis will be made for the eigen frequencies, which can be seen on Figures 7.4 and 7.5.

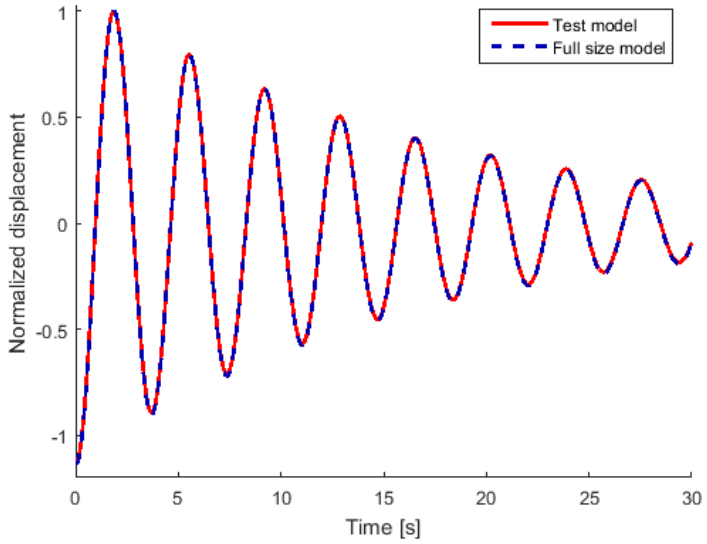

Figure 7.4: Comparison of normalized surge decay tests between the test model and full size model

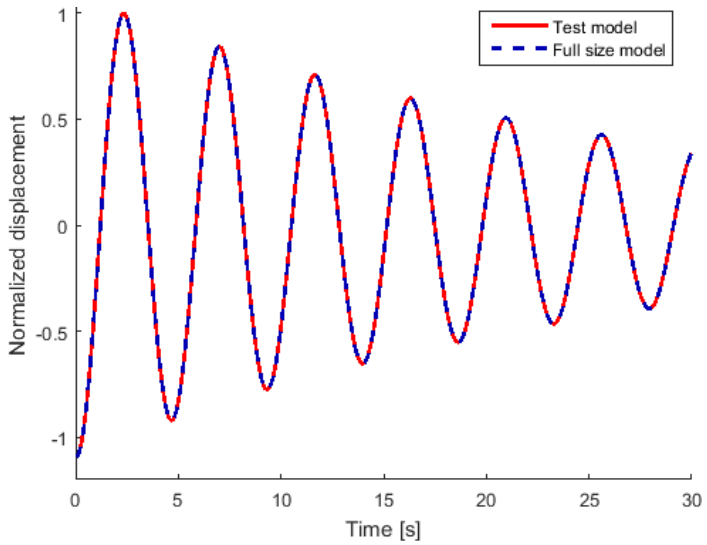

Figure 7.5: Comparison of normalized heave decay tests between the test model and full size model

As with the wave case, the Froude scaling method is an accurate way of upscaling to a full size model.

7.3 Considerations regarding scaling method

Though the behavior of the full size model can be correctly predicted from the downscaled model, problems arise if the full size model were to be build. The TLB B is supposed to be constructed in light weight steel [41], however the test model is constructed in aluminum, polycarbonate, and PVC. Neither of these materials resemble steel in density or Youngs modulus in relation to the test model or the full size model. This selection of materials does however make sense if the full size model were to be made of aluminum.

The parts of the test model made of aluminum, namely the nacelle, the transition pieces, and the bottom section of the TLB B all have the correct mass. Though the stiffnesses are 40 times too high, the effect can be assumed to be negligible, since these parts either should be considered stiff, as is the case for the transition pieces, or because these parts wont experience significant deformation. As for the parts made of polycarbonate and PVC, these will not have the correct density, but they do have approximately 40 times lower Youngs modulus than aluminum, and therefore have approximately the correct stiffness when upscaling the geometry. In the case of the mooring lines, a spring was used in combination with the mooring lines to give both the correct stiffness and density.

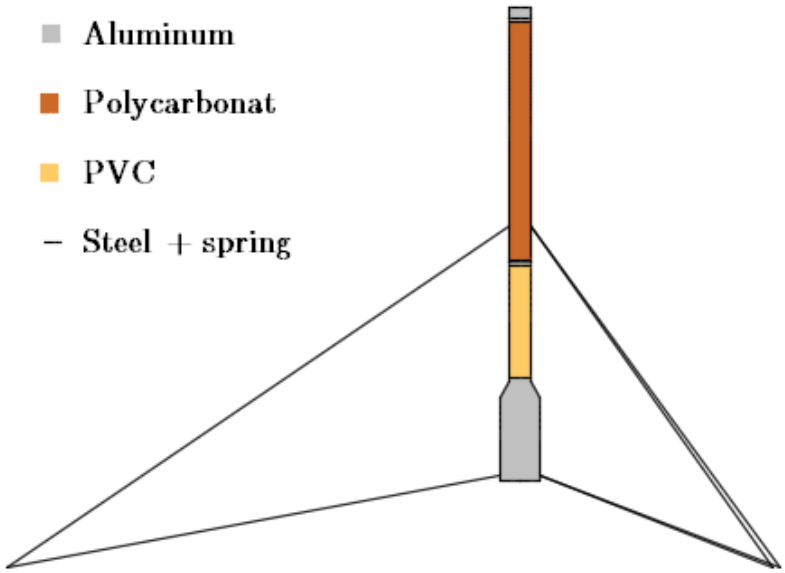

Figure 7.6: Material composition of TLB B FOWT.

The effect of only using aluminum for the TLB B substructure and wind turbine can easily be numerically tested. Figures 7.9 and 7.10 show the difference between the full size model experimentally tested and an aluminum model.

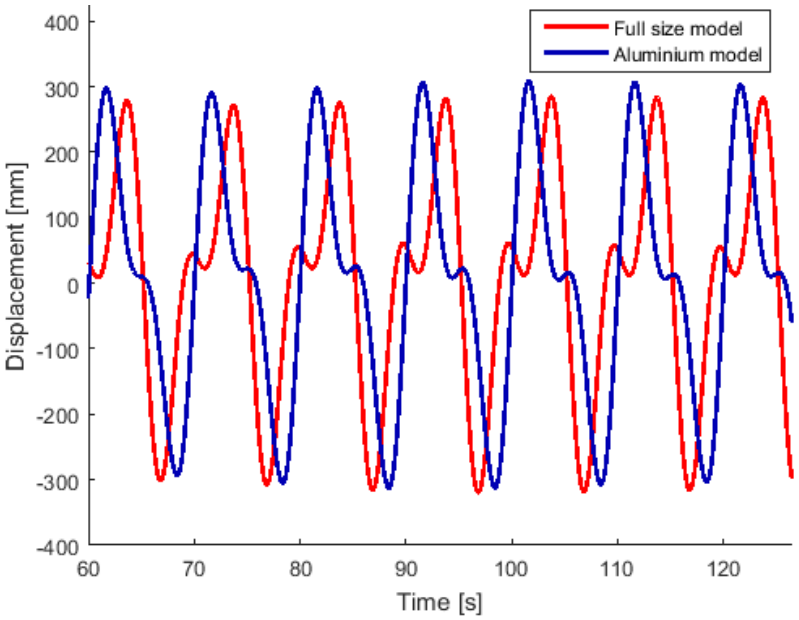

Figure 7.7: Comparison of surge displacements between full size model and aluminum model

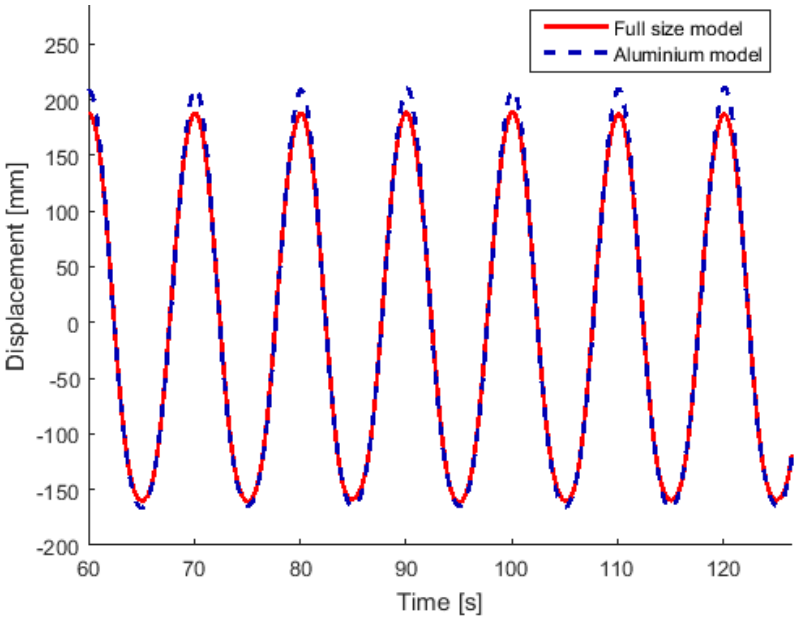

Figure 7.8: Comparison of heave displacements between full size model and aluminum model

Figure 7.10 show what is expected, the added weight of using more aluminum causes small deviations in heave displacements. Interestingly, the maximum amplitude of the horizontal displacements does not change despite the lower tower stiffness, but the displacements pattern has shifted. The reason for this was evaluated by changing stiffness and density between the models separately and the result showed that the change shift in surge pattern was due to the change of stiffness.
Since the eigenfrequency is paramount in analyzing FOWT a Fast Fourier Transform

(FFT) of the free decay tests has been made for both the full sized test model and the corresponding aluminum model. It should be noted that the aluminum model required more damping to avoid instability, which is the reason for the lower spectral density. This did not affect the eigenfrequencies.

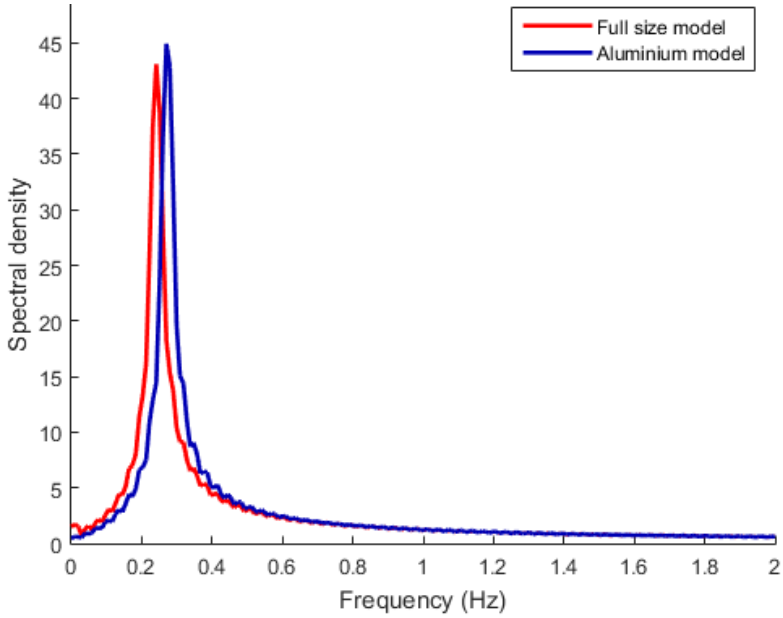

Figure 7.9: Comparison of FFT between full size model surge displacements (0.24 Hz) and aluminum model surge displacements (0.27 Hz)

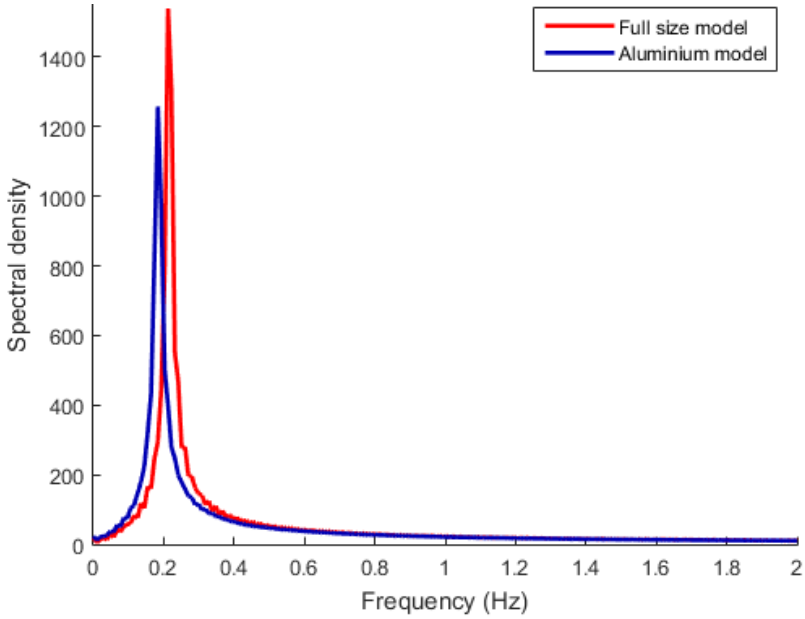

Figure 7.10: Comparison of FFT between full size model heave displacements (0.21 Hz) and aluminum model heave displacements (0.18 Hz).

It is clear that the eigen frequencies change. As mentioned in chapter 4, the critical excitation range is between 0.115-0.220 Hz as well as 0.345-0.660 Hz. Both models avoid these ranges in surge, and neither model avoid it in heave. It should be noted that applying a

nacelle and blades will further effect the eigen frequencies.

The experimenters reason to use aluminum and scalewise similar materials instead of light weight steel is not known, since the paper containing arguments for the scaling method is unavailable. However if the full size model were to be made of steel, it would sink even if the density could be reduced to $6500\frac{kg}{m^3}$. To reduce the mass, the volume must be reduced as well. To avoid change of the outer geometry, which relates to the forces acting on the structure, and must be unchanged, for the model test to make sense, the thickness of the model must be reduced. This changes the cross sectional area and moment of inertia, which relates to stiffness. Fortunately the Youngs modulus of steel is larger than aluminum, and in fact the ratio between density and Youngs modulus for the two materials are approximately the same, namely 2.9. Reducing the thickness of the model by 1:3 gives approximately the correct mass, and bending and axial stiffnesses, since the thickness is much lower than the radius for a majority of the model, which means the ratio between area and moment of inertia follow that of the thickness. Eq. (7.1) to (7.4) show the ratios that the area and inertia change, compared to the reduction of thickness, and compare the mass and stiffnesses of the aluminum and reduced thickness steel model.

$$t_{al} = 3t_{steel} \rightarrow A_{al} = 2.9A_{steel} \wedge I_{al} = 2.8I_{steel} \tag{7.1}$$

$$A_{al}\rho_{al} = 2.9A_{steel}\frac{1}{2.9}\rho_{steel} = A_{steel}\rho_{steel} \tag{7.2}$$

$$A_{al}E_{al} = 2.9A_{steel}\frac{1}{2.9}E_{steel} = A_{steel}E_{steel} \tag{7.3}$$

$$I_{al}E_{al} = 2.8I_{steel}\frac{1}{2.9}E_{steel} = 97\%I_{steel}E_{steel} \tag{7.4}$$

The only part of the model, which cannot be converted to steel with a reduction of the thickness is the nacelle, since it is solid. However due to the importance of having the correct mass at the top of the turbine, and since the stiffness of the nacelle is of little interest, it can be assumed that the correct mass is used.

It is clear form eq. (7.1) to (7.4) that the test model can be converted from an aluminum model to a steel model by reducing the wall thickness. A probable reason why the test model was not made of steel, as its full size counterpart, could be the lack of a material with the correct downscaled properties, or it could be that the lower necessary wall thickness increased the risk of model impression, since the approximate 5 mm wall thickness is reduced to about 1.7 mm. Further analysis with the actual light steel model is not made, due to the lack of information about the precise mass and stiffness.

8

Analysis of a full size tension leg buoy exposed to mooring line fracture

A major concern when dimensioning TLB are the risk of mooring line fracture. The reason for this is obvious, the mooring lines are the main stabilizing factor and losing one or more may result in capsizing. Since physical model tests are impractical, a numerical approach is better suited for analyzing such cases.
This chapter concerns the method used, when analyzing mooring line fracture, as well as a study to possibly find a better way to arrange the mooring lines in order to avoid fracture. As in chapter 7, the concept to be analyzed is the TLB B.

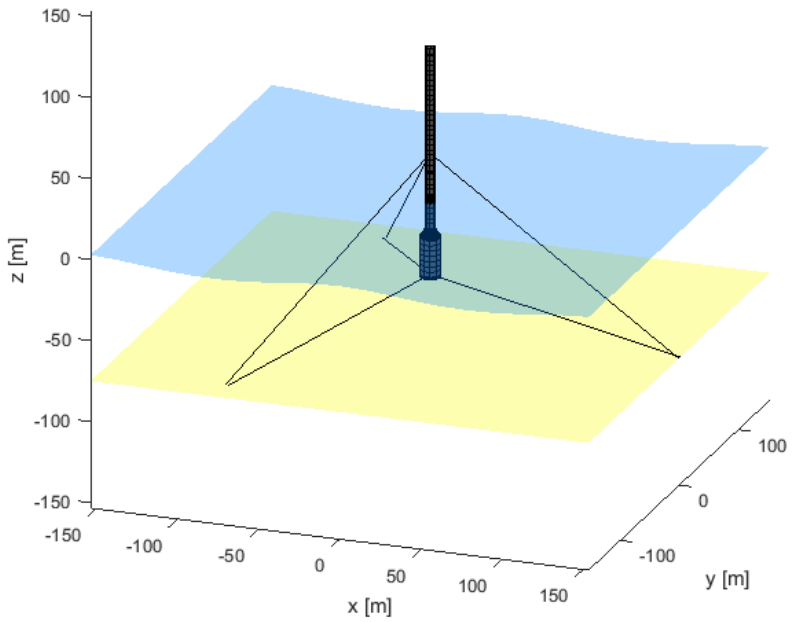

Figure 8.1: TLB B in the ocean environment before mooring line fracture.

This chapter contains the procedure and results in analyzing mooring line fracture. The ocean loads are specified through an embedded extreme wave, which is thought to cause the mooring line fracture at the wave top. The following fracture is analyzed in the expected worst case scenario, for both an upper placed and lower placed mooring line. The analysis leads to a new design of the TLB B, which consequently is analyzed in regular conditions.

8.1 Investigated load scenario

The stream function wave theory and the development of the wave add-in are in details explained in chapter 3, to give the reader a theoretical background to this section.

The relatively low draft of the full scale TLB B implies that the optimal installation water depth is around 75m [39]. As seen from the upscaling of the wave parameters in the experimental wave load case, the experimental water depth at 10m is upscaled to 400m. To accommodate the optimal water depth, the influence of changing the water depths from 400m to 75m has been investigated.

Compared Properties	**Unit**	**75 [m]**	**400[m]**	**Ratio**
Wave length	[m]	157.2	157.9	0.996
Wave number	[m]	0.040	0.040	1.000
Discharge	[m]	2.111	2.101	0.995
Max particle vel.	[m]	1.815	1.804	0.995
Max particle acc.	[m]	1.009	1.004	0.993

Table 8.1: Comparison of load case 9 waves in 75 m and 400 m water depth.

Since the differences in Table 8.1 are small, a water depth of 75m is utilized in further analyzes.
The implementation of the stream function add-in in SOFIA enables, as mentioned earlier, to correctly simulate all wave theories. Due to the interest of investigating the dynamic response of the structure after a possible mooring line fracture, a regular wave realization only consisting of extreme waves will produce an unrealistic scenario. To conduct a realistic simulation that causes a mooring line fracture, and at the same time a realistic dynamic response, an extreme wave is instead embedded in the wave realization of load case 9.

8.1.1 Extreme wave based on FINO data

A statistical determination of a design basis made from MetOcean data is not in the scope of the project. Instead is referred to the [46], where a comprehensive design basis is made from FINO1 measurements. From the design basis is a significant and maximum wave height estimated, with a return period on 50 years.

$H_{s,50}$	$H_{max,50}$	T_{Lower}	T_{Upper}
10.33	19.22	11.40	14.68

Table 8.2: ULS waves based on FINO1 data [46].

To the right in Table 8.2 is listed two corresponding design wave periods, which delimit a range defined by the following eq. (8.1), dependent on the significant wave height and the acceleration of gravity [28].

$$11\sqrt{\frac{H_{s,50}}{g}} \leq T_{design} \leq 14.3\sqrt{\frac{H_{s,50}}{g}} \tag{8.1}$$

The design wave period, that implies the highest loads, should be used in the further simulations. Since no certain load case is chosen in [28], it is decided to use the significant wave

height ($H_{s,50}$) and the upper period in the further mooring line fracture simulations, as this results in the lowest jump in hydrodynamic loads, when in extreme wave is embedded in load case 9.

In order to give a correct description of the waves, it is investigated which theory that is required. Table 8.3 shows the estimated values of the axes of the wave applicability diagram.

Wave Load Case	$\frac{h}{tg^2}$	$\frac{H}{gT^2}$	Wave theory
Embedded extreme wave	0.0354	0.00488	Stream function 3rd order
Load case 9	0.0763	0.00529	Stream function 3rd order

Table 8.3: Required wave theory.

By inserting the determined values for the axes in the wave applicability diagram, both load case 9 and the extreme wave is located in the region of Stokes 5th order waves or stream function 3rd order.

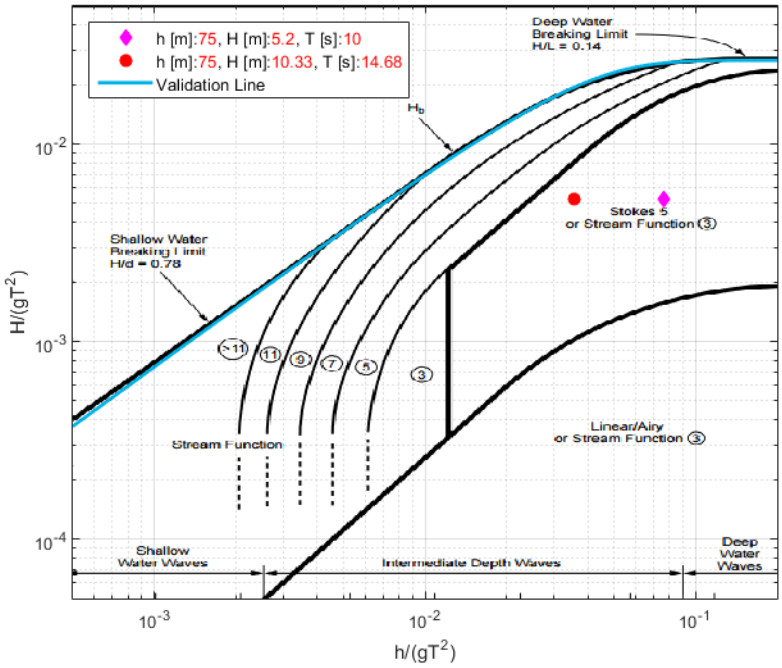

Figure 8.2: Applicability diagram. The purple point is the load case 9 and the red point the extreme wave.

8.1.2 Implementation of an embedded stream function wave

To describe the correct wave scenario, the previously selected extreme wave is embedded into the regular wave realization, upscaled from the experimental wave load case in chapter 6. Normally, when design waves are included in load simulations, they are embedded into realization of irregular waves.However, the scope of this project is to only consider the ULS, irregular waves are delimited and the design wave is embedded in a realization of regular waves [28].

The method utilized to embed the chosen extreme wave, is directly through SOFIA, where an arbitrary zero down-crossing in the wave realization is chosen. To the associated time, the realization is split apart and the extreme wave is embedded in between. As shown in Figure 8.3, the extreme wave is embedded between point 1 and point 2 and, as previously mentioned, with a shift, that is as smooth as possible.

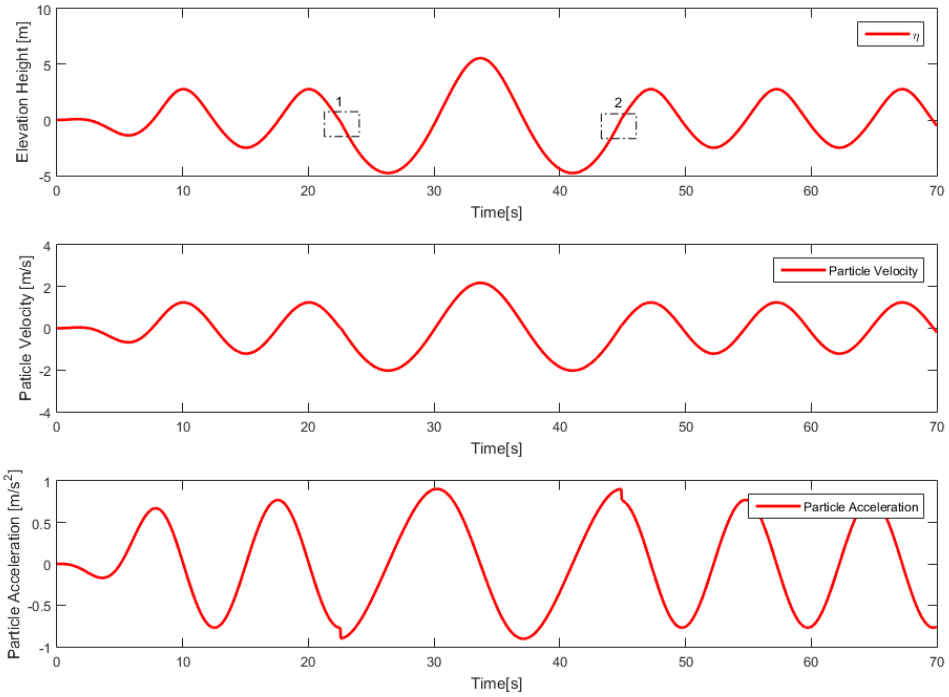

Figure 8.3: Embedded stream function wave with associated horizontal particle kinematics.

Utilization of this method implies that discontinuity in the particle acceleration, in the horizontal direction, is impossible to avoid, since the shift is conducted at the location of its maximum. The same tendency is observed in the vertical particle velocity, which also corresponds to what is shown on Figure 3.7. The consequence is expressed in the evaluation of drag and inertia loads, which is directly dependent on the particle kinematics.

To avoid the discontinuities, and thereby spikes in the hydrodynamic loads, blending formulas may be used to establish a correct weighting of the particle kinematics in the shifting regions [43].

8.2 Mooring line load analysis

Before conducting the simulation of a mooring line fracture, it is investigated which mooring line is exposed to the highest loads, and thereby probably collapse first, if an extreme wave is applied.

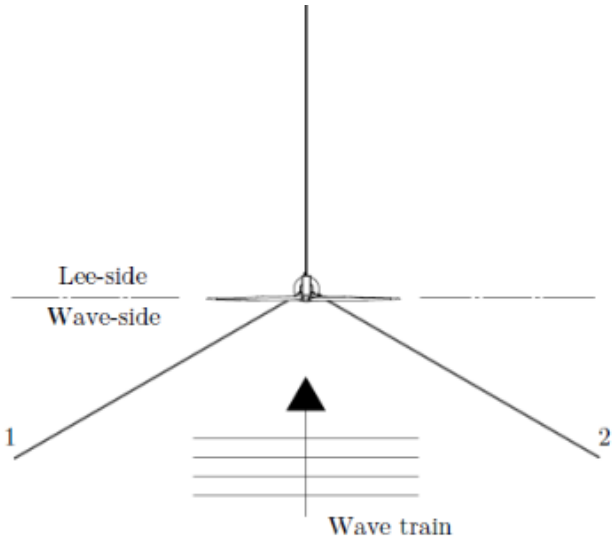

Figure 8.4: TLB B in relation to wave direction, and the distribution of wave- and lee-side mooring lines.

Due to that tension forces are the only represented forces in the mooring lines, the one that is obtaining the largest amplitude in normal forces is likely to be the first to collapse. However, as a result of fatigue, the mooring lines and their connection clamps weaken with time, and thus are more susceptible to break, which adds the consideration of normal force variations.
A simulation to determine which mooring lines break is conducted with basis in the upscaled experimental load case, without the extreme wave implemented, in order to avoid noise from the small jump in particle kinematics. To achieve better comparability when conducting later analyzes, all mooring line forces (Fd) are normalized with regards to the pretension forces in the original upscaled full size model (Fi). Since the normal forces in the upper and lower mooring lines differ, the upper mooring line forces are compared to the initial upper mooring line force, and likewise the lower mooring lines are compared to the original initial lower mooring line forces. The normal forces seen in Figure 8.5 shows the tension forces in each mooring line, during the upscaled load case 9.

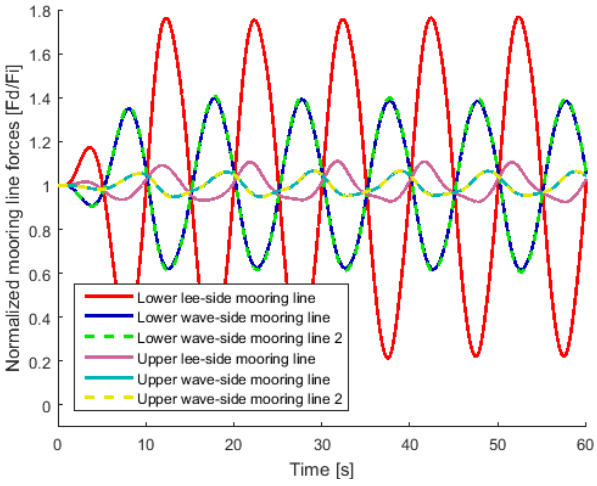

Figure 8.5: Normalized mooring line forces in full size model in load case 9.

It is clear that the lee-side mooring lines experience both the largest force amplitudes and variations, and they are therefore deemed to be the ones to fracture, in situations where an extreme wave is applied.

8.3 Numerical mooring line fracture method

When two elements are separated in a numerical analysis, they no longer share DOF. This means that every matrix and vector needs to grow additionally in respect to the added DOF. In the case of fracturing the lee-ward mooring line, three translational DOF must be added, since the rotational DOF are already decoupled. As this addition of DOF will occur in the middle of the numerical analysis, it is preferable to expand the matrices and vectors before starting the analysis. This is done by allocating 3 rows and columns of 0's to the matrices and vectors, which does not affect the analysis.

$$\begin{bmatrix} x_1 \\ \vdots \\ x_n \end{bmatrix} \rightarrow \begin{bmatrix} x_1 \\ \vdots \\ x_n \\ 0 \\ 0 \\ 0 \end{bmatrix} \qquad \begin{bmatrix} K_{1.1} & \cdots & K_{1.n} \\ \vdots & \ddots & \vdots \\ K_{n.1} & \cdots & K_{n.n} \end{bmatrix} \rightarrow \begin{bmatrix} K_{1.1} & \cdots & K_{1.n} & 0 & 0 & 0 \\ \vdots & \ddots & \vdots & \vdots & \vdots & \vdots \\ K_{n.1} & \cdots & K_{n.n} & 0 & 0 & 0 \\ 0 & \cdots & 0 & 0 & 0 & 0 \\ 0 & \cdots & 0 & 0 & 0 & 0 \\ 0 & \cdots & 0 & 0 & 0 & 0 \end{bmatrix} \tag{8.2}$$

When the mooring line fracture occur, these rows and columns will be replaced with the stiffnesses, masses, deflections etc. of the translational DOF of the fractured mooring line. This is done by redefining how SOFIA compose the structure in the time step where the mooring fracture occur.

8.4 Mooring line fracture analysis

The main concern with regards to a stabilization failure is that the TLB B will capsize, meaning either the nacelle will reach the wave crest, which may result in major damage to the internal mechanics. Furthermore the wind turbine blades risk being exposed to ocean loads, which may result in blade fracture. To evaluate whether this happens, the displacements of the lumbed mass on top of the TLB B model, representing the nacelle, will be recorded and compared to the wave elevation. As mentioned in section 2.6, the wind turbine is expected to experience large rotations after the fracture, which will cause large horizontal displacements of the nacelle. For that reason the position of the nacelle is compared to the relative wave elevation, which is the wave elevation at the displaced position of the nacelle.

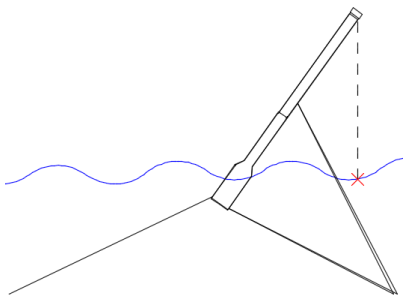

Figure 8.6: Relative wave elevation

Another critical criteria is whether an additional mooring line will fail, which is evaluated from their normal forces.

Due to instabilities present when conducting mooring line fracture analyzes, it is necessary to use reduced hydrodynamic coefficients. A vertical added mass of 0.8 instead of 1.5, a horizontal added mass of 0 instead of 0.1, and a stiffness proportional damping coefficient of 0.005 instead of the upscaled version of 0.0316 is used. In addition, a reduction of the time step is needed. Since inertia forces are dominant and the coefficient unchanged, the change in dynamic response is deemed to be negligible.

Capsizing and mooring line forces are checked through the fracture analyzes, which are conducted through subjecting the TLB B wind turbine to the embedded extreme wave described in chapter 8.1. The fractures are set to occur at the top of the extreme wave, since this point is deemed to be the worst case scenario, at which the fracture can occur. Figure 8.7 and 8.8 show the nacelle compared to the wave elevation for fracture of upper and lower lee-side mooring lines, as well as horizontal displacement and rotation.

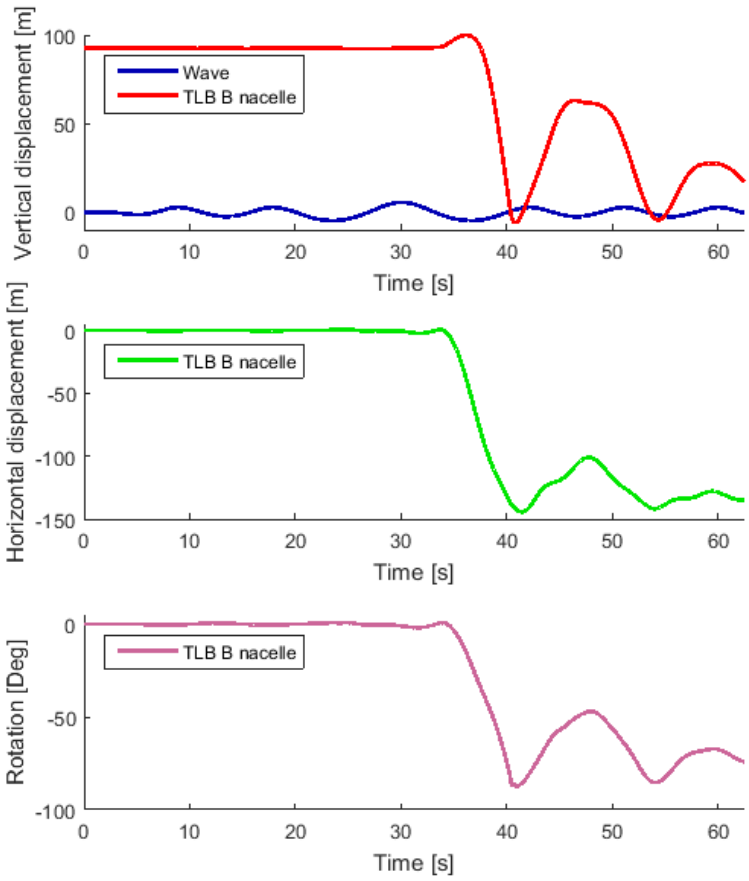

Figure 8.7: Nacelle displacement, when fracturing upper lee-side mooring line.

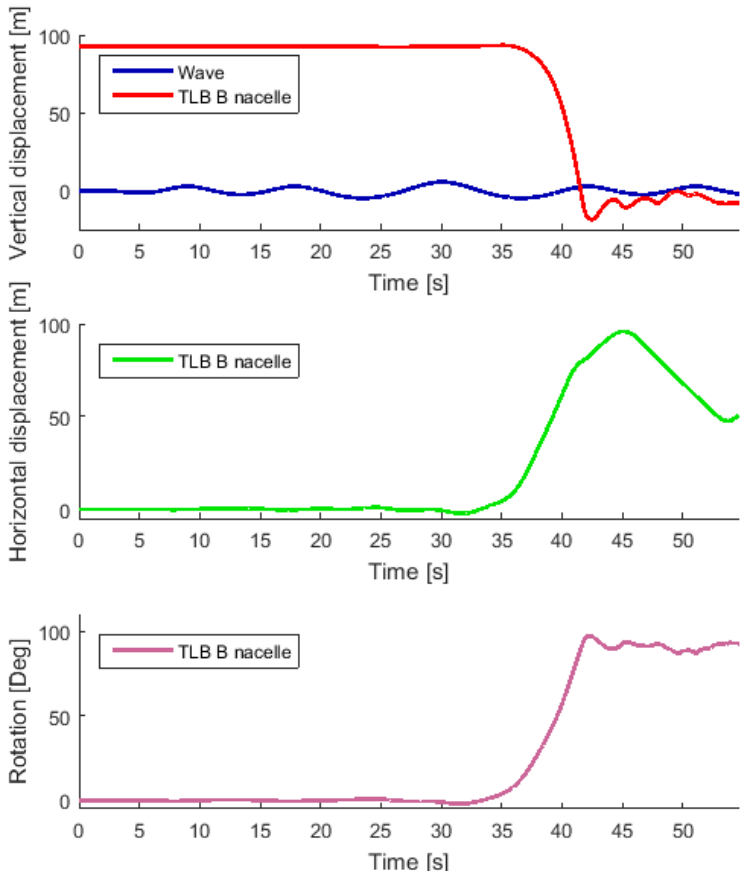

Figure 8.8: Nacelle displacement, when fracturing lower lee-side mooring line.

It can be seen that capsizing occur with both concepts.
Figure 8.9 and 8.10 show the normalized mooring line forces after mooring line fracture. Note that the slight increase in force at 22.5s is a result of the shift to extreme wave.

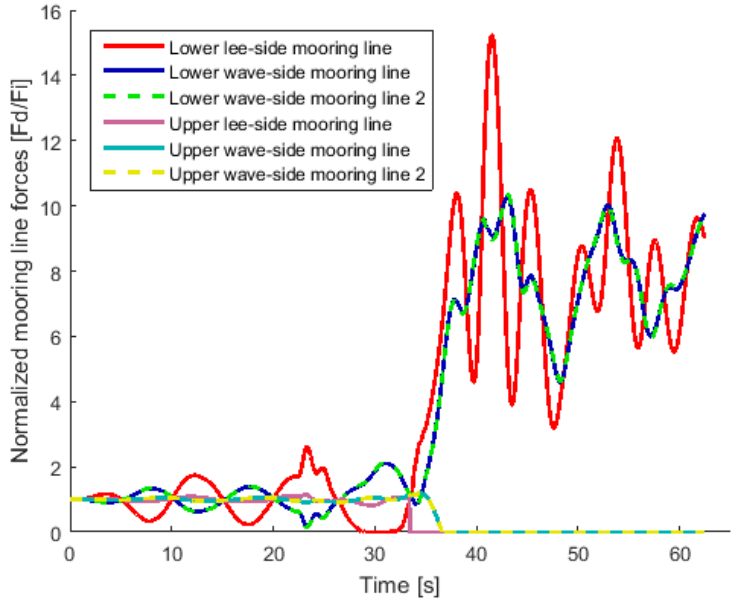

Figure 8.9: Mooring line forces after fracture of upper lee-side mooring line.

Figure 8.9 shows a major increase in the lower mooring line forces. The maximum force in the lower lee-side mooring line is increased fifteen-fold as a result of the TLB B trying to find a new equilibrium position. This must be a consideration if mooring line fracture is to be allowed. The other two lower mooring lines experience a similar response, with a tenfold increase in normal force. Interestingly the remaining upper mooring lines go slack due to the large rotation towards their direction. As expected the force in the fractured mooring line goes towards zero.

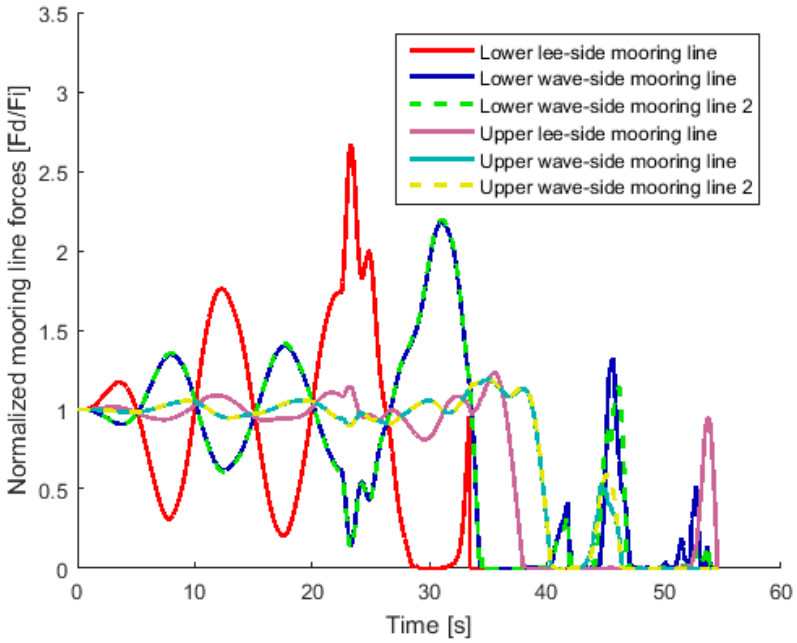

Figure 8.10: Mooring line forces after fracture of lower lee-side mooring line.

As is can be seen on Figure 8.8 the TLB B capsize with fracture of the lower lee-side mooring line, and in fact end up floating sideways. As no tension is present in the mooring lines as seen on 8.10 the TLB B moves freely with the waves until small tension forces reappear.
The final positioning of the TLB B after fracture can be seen on Figure 8.11 and 8.12.

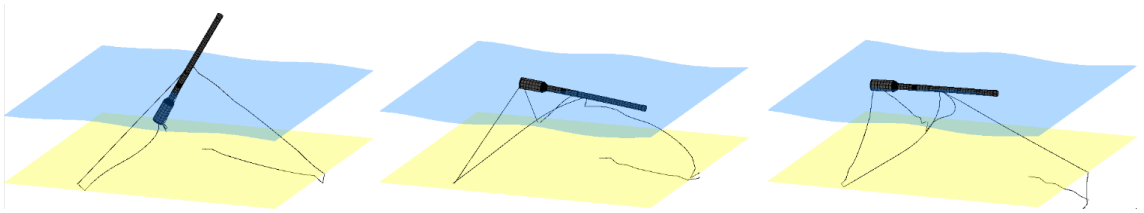

Figure 8.11: Development of lower lee-side mooring line fracture. To the left, the initial response just after mooring line fracture. In the middle, the nacelle being submerged, equal to capsizing. To the right, the new equilibrium position.

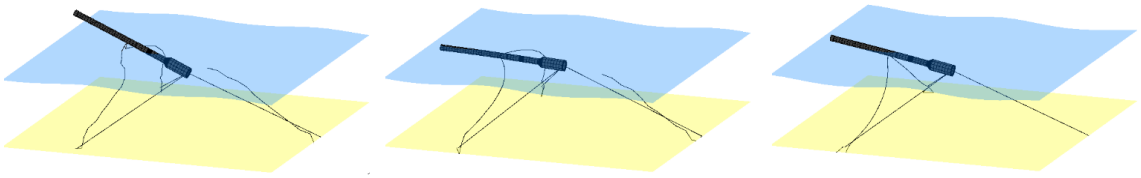

Figure 8.12: Development of upper lee-side mooring line fracture. To the left, the initial response just after mooring line fracture. In the middle, the nacelle being submerged, equal to capsizing. To the right, the new equilibrium position.

It is clear that mooring line fracture is not allowed with the current geometry. Therefore it is of great interest to evaluate whether a better mooring line configuration of the TLB B can be found. This thesis search to find such improvement through a geometric parameter study of the mooring line setup.

8.5 Parametric study of the TLB B geometry

As shown in the previous results a potential mooring line fracture forces the structure to capsize. In order to investigate the possibility of changing the mooring line setup, such that capsizing can be avoided, the following parametric study is conducted. The study is an early stage study used to elaborate on which parameters, that are important to consider, if an optimization of the TLB B stability is desired.

Through the study the influence of changing the mooring points on the TLB B, the wind turbine, and in the seabed is investigated. The study considers four different combinations:

- Upper mooring points at the wind turbine are moved 3m upwards.
- Upper mooring points at the wind turbine are moved 10m downwards.
- Lower mooring points at the TLB B are moved 3m upwards
- The radius of the lower mooring line footprint is reduced from 153.4m to 100m.

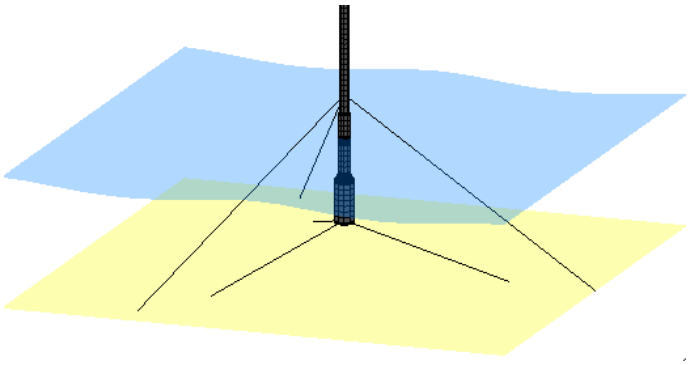

Figure 8.13: Optimized TLB B mooring system

8.5.1 Displacement results

First the vertical displacements are analyzed to evaluate whether capsizing can be avoided. Figure 8.14 and 8.15 show the vertical displacement of the nacelle after fracture.

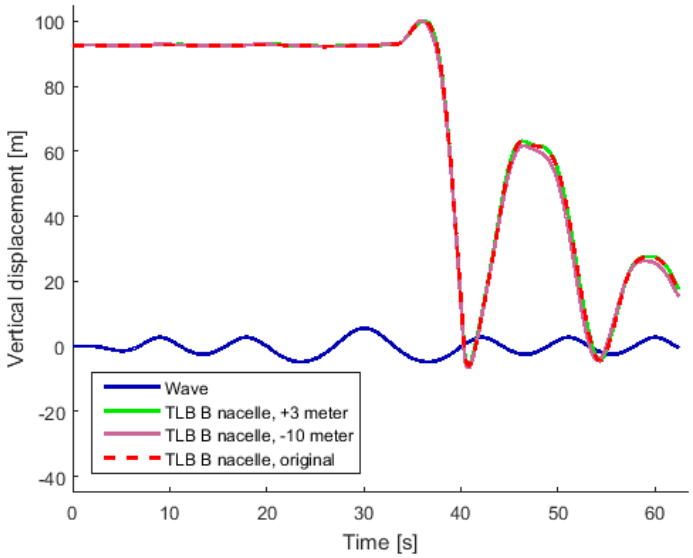

Figure 8.14: Comparison of nacelle displacement, with different upper mooring line configuration, and upper lee-side mooring line fracture.

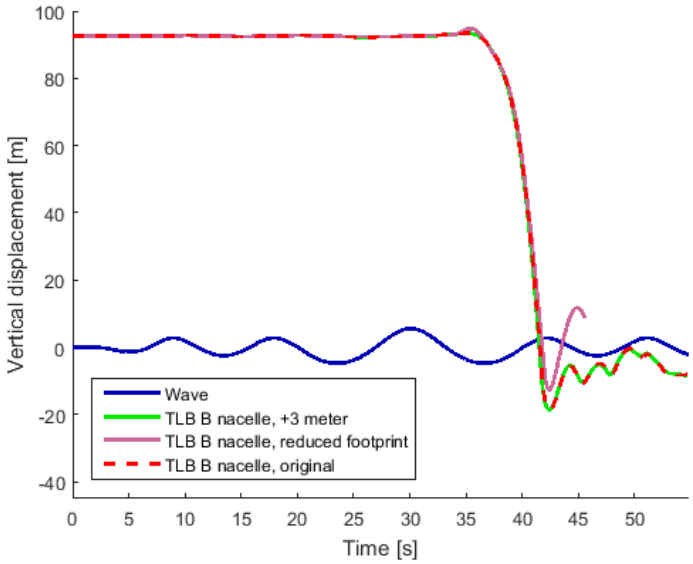

Figure 8.15: Comparison of nacelle displacement, with different lower mooring line configuration, and lower lee-side mooring line fracture.

It is seen that moving the fractured mooring line upwards make no difference with regards to capsizing. Reducing the radius of the lower mooring footprint, does however reduce the extend of the vertical displacement, but it does not prevent capsizing in this analysis.

8.5.2 Mooring line force results

As with the dynamic response the mooring line forces does not change by moving the fractured mooring lines 3m upwards nor 10m downwards, however it does cause a slight increase and decrease respectively in lower mooring line forces. These results are not shown here, but can be seen on the digital copy. Reducing the lower mooring line footprint did make a difference in dynamic response, which can be seen of Figure 8.16

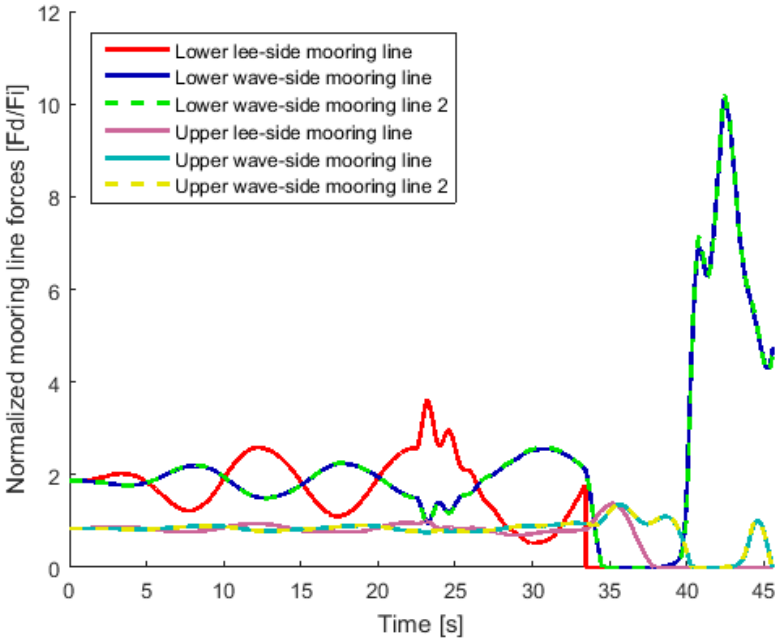

Figure 8.16: Mooring line forces with reduced mooring line footprint after fracture of lower lee-side mooring line.

The mooring lines becomes slack, however after five seconds tension reappear in the lower wave-side mooring lines. This is at the same time as the vertical displacement of the nacelle start to slow down, indicating that reducing mooring radius might reduce the chance of capsizing. An additional side effect though is the added mooring forces in the wave-side mooring lines as a result of the effort to counteract the capsizing.

8.5.3 Further analysis of reduced mooring line footprint

Since an improved dynamic response was achieved with fracturing the lee-side lower mooring line after reduction of mooring line footprint, the same geometry is analyzed with fracture of the upper lee-side mooring line. The vertical displacements can be seen on Figure 8.17

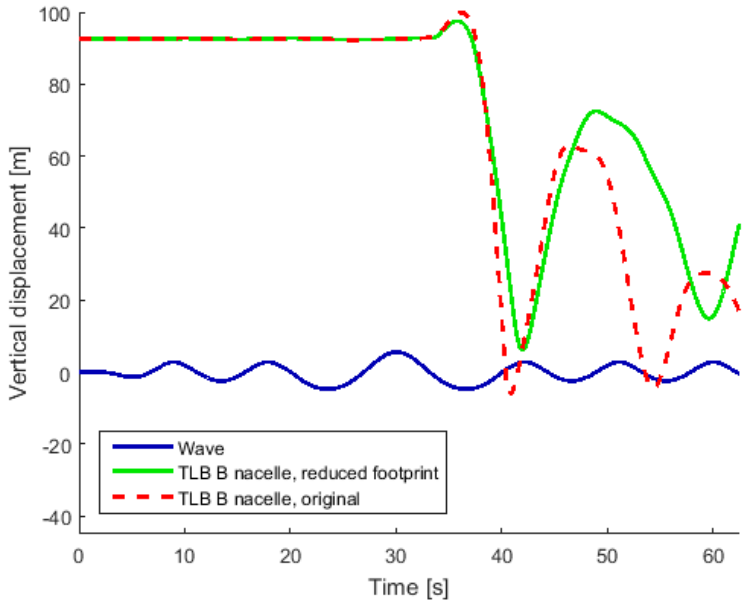

Figure 8.17: Comparison of nacelle displacement, with reduced mooring line footprint of lower mooring lines, and upper lee-side mooring line fracture.

It can be seen that the nacelle does not reach the water surface, and thus does not capsize. A comparison of horizontal displacement and rotation can be seen on Figure 8.18 and 8.19

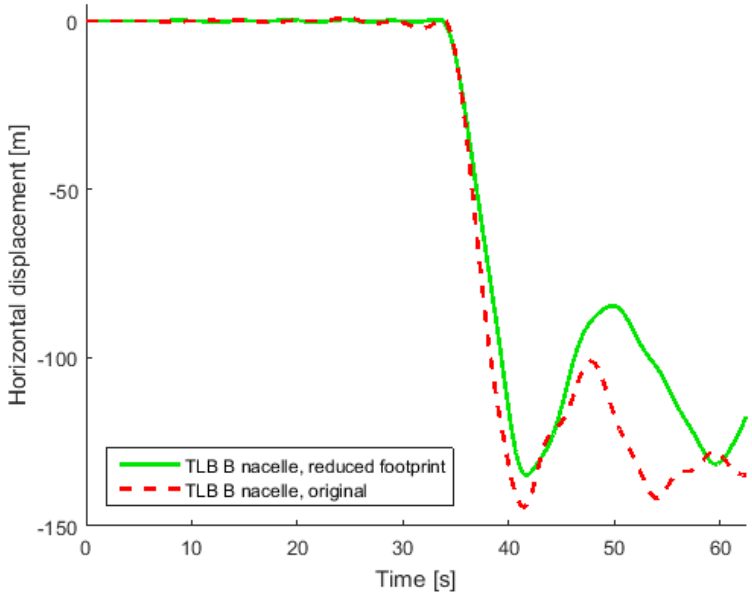

Figure 8.18: Comparison of nacelle displacement, with reduced mooring line footprint of lower mooring lines, and upper lee-side mooring line fracture.

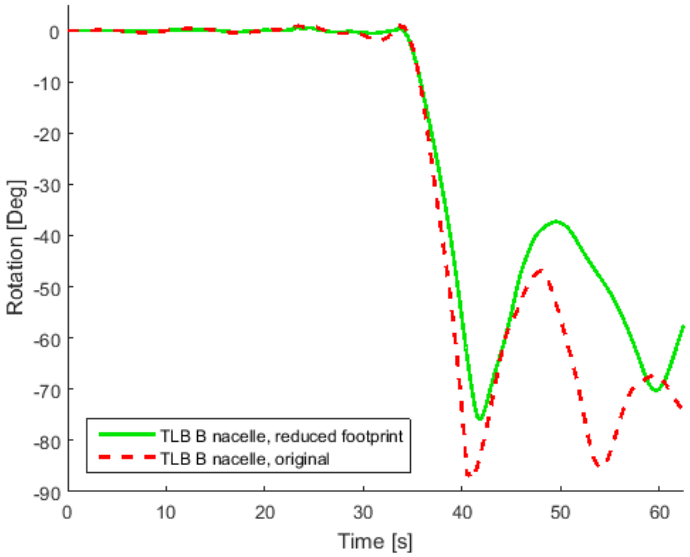

Figure 8.19: Comparison of nacelle rotation, with reduces mooring line footprint of lower mooring lines, and upper lee-side mooring line fracture.

It is clear that all displacements and rotations of the nacelle is reduced. Next the mooring line forces seen on Figure 8.20 are evaluated.

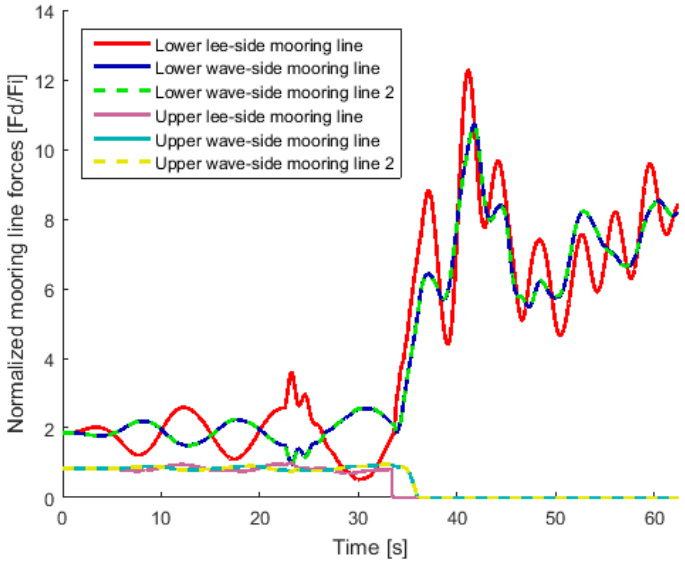

Figure 8.20: Mooring line forces with reduced mooring line footprint after fracture of upper lee-side mooring line.

The dynamic response is similar to Figure 8.9 where the mooring line footprint was not reduced, however the normalized amplification in the lower mooring lines are more equally distributed. This is due to the added vertical positioning of lower mooring lines, which for this scenario reduce the chance of slack line events.

The dynamic response can be seen illustrated through Figure 8.21

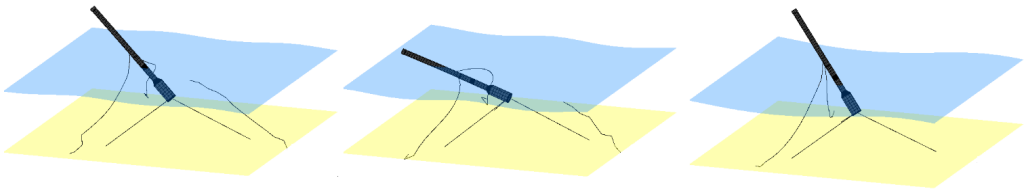

Figure 8.21: Development of upper lee-side mooring line fracture with lower mooring line footprint. To the left, the initial response just after mooring line fracture. In the middle, lowest positioning of the nacelle, which is above MSL. To the right, the new equilibrium position.

8.5.4 Conclusion of parametric study

Different configurations of the mooring line setup either increased or decreased mooring line forces, but in all cases the mooring line forces significantly increased as a result of the mooring line fracture.
As seen on Figure 8.15 capsizing could not be avoided in this extreme wave scenario, when the lower mooring line fractured. Figure 8.17 however, show that reducing the lower mooring line footprint to a radius of 100m resulted in capsizing being avoided for fracturing the upper mooring line. For this reason, further analysis of the reduced lower mooring line footprint design will be made.

8.6 Optimized mooring configuration analysis

Before it can be concluded that a better mooring line configuration is achieved, the dynamic response of the reduced lower mooring line footprint model must be analyzed without mooring line fracture. A comparison of the dynamic responses can bee seen on Figure 8.22 and 8.23. All numerical settings are reset to those used for model testing in chapter 6.

Wave case

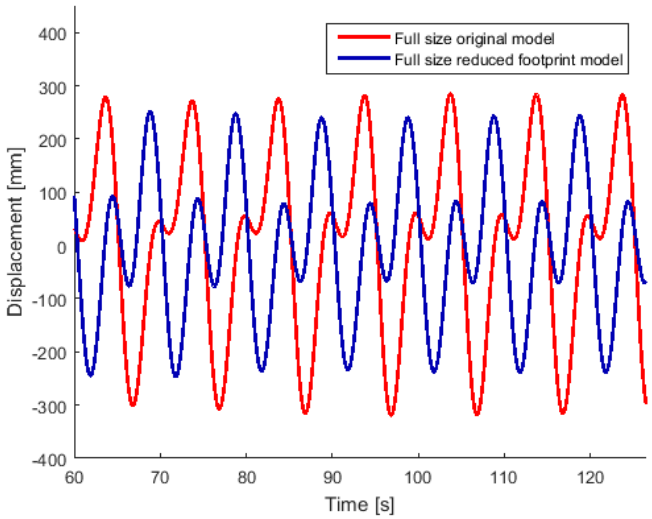

Figure 8.22: Comparison of surge displacements between original test model and test model with reduced mooring line footprint.

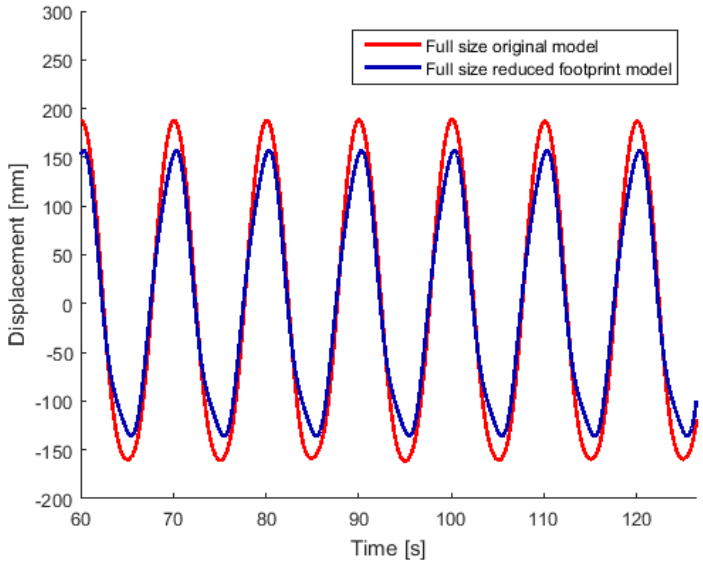

Figure 8.23: Comparison of heave displacements between original test model and test model with reduced mooring line footprint.

Both figures show that maximum amplitudes are reduced using the reduced footprint for the lower mooring lines, which is a positive development. Unfortunately the surge displacements experience larger secondary amplitudes, which may have unfortunate consequences, like larger fatigue damage to the mechanical parts of the nacelle. It can also indicate larger fatigue damage in the mooring lines, which will be evaluated from the new mooring line forces in Figure 8.24

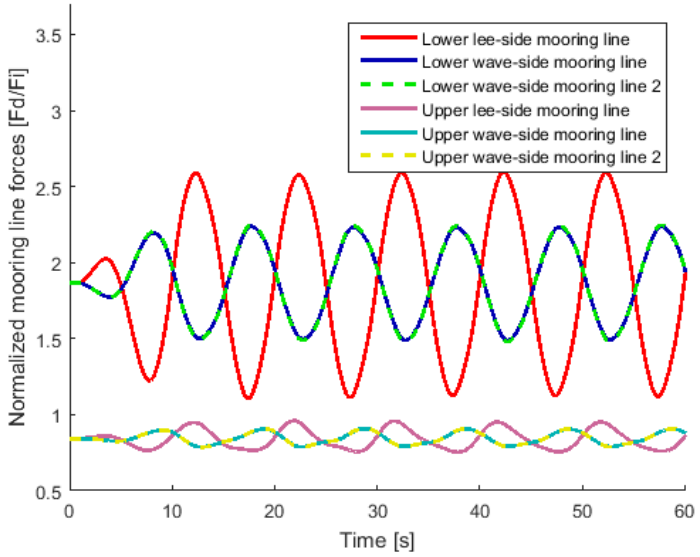

Figure 8.24: Mooring line forces with reduced lower mooring line footprint analyzed through load case 9.

As a result of the new mooring line configuration, the normal forces in the mooring lines are changed. As seen in Figure 8.24 the initial forces in the upper and lower mooring lines

have decreased by 16% and increased by 87% respectively. The maximum force amplitudes have decreased 14% and increased 47% respectively. The force variation increased for both by 9% and 6% respectively.

Decay test

The change of eigenfrequency is also of interest. Decay tests, similar to those previously performed, were made on the reduced footprint concept, and the results can be seen on Figures 8.25 and 8.26.

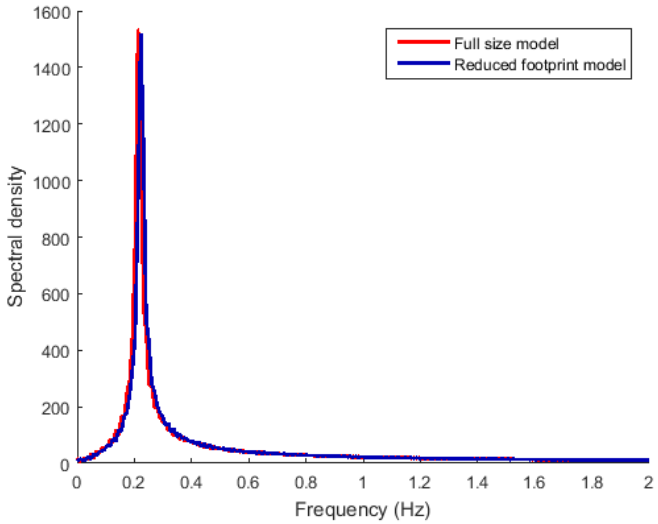

Figure 8.25: Comparison of surge FFT between original test model (0.21 Hz) and test model with reduced mooring line footprint (0.22 Hz).

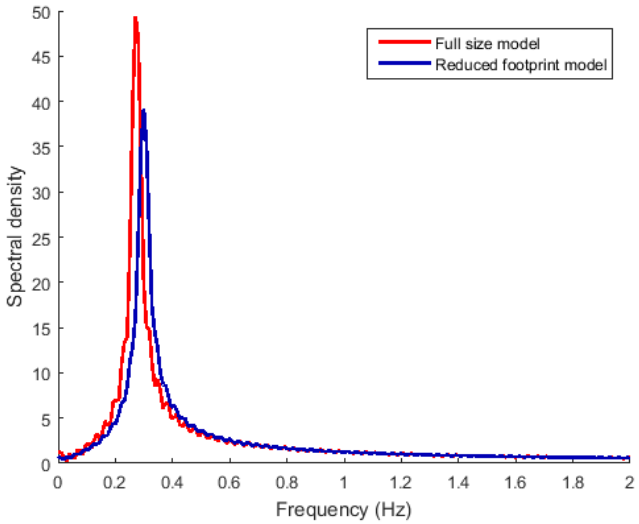

Figure 8.26: Comparison of heave FFT between original test model (0.27 Hz) and test model with reduced mooring line footprint (0.30 Hz).

The FFT shows next to no difference in the change of surge eigenfrequency, but both the heave spectral density and eigenperiods change. An increase in spectral density means that

the amplitudes of the decay test are larger, meaning that the decay test dampens slower with the reduced mooring line footprint model. In comparison to the critical excitation range, which was 0.115-0.220 Hz as well as 0.345-0.660 Hz, the reduced mooring line footprint model has a better surge eigenfrequency. It is however, still close to the critical excitation range.

8.6.1 Conclusion on mooring optimization

The analyzes show that the reduced lower mooring line footprint creates a more stable geometry, with smaller deflections in surge and heave. In addition the eigenfrequencies are improved in regard to the wind turbine blade excitation ranges. However, in relation to fatigue, the variation in amplitudes increase for most exposed mooring lines, meaning the new geometry may be more susceptible to fatigue damage.

9
Discussion

Due to the extent of the thesis, and the complexity of the conducted numerical analyzes, certain areas of the project may need further study. These will be commented on here.

Excitation at mooring line connections: Since the mooring lines are connected at the surface of the structure, and not at the center as modeled in SOFIA, the effect of excitation is lost. This may have a significant influence, with regards to the displacements and rotations of the TLB B in the mooring line fracture analyzes.

Pretension error: The pretension in both TLB were both numerically determined by calibrating the model to the correct equilibrium position. This created tension forces in the mooring lines, which for the lower mooring lines were inconsistent with those given in the model tests. [39] recognize that errors were made in determination of mooring line stiffness, and that complications in the form of model collapse occurred during the process of correcting these errors. [39] conclude that the test results can still be used for numerical validation, as was shown for the TLB B.

Lack of convergence study: Since a very fine element discretization was used for both TLB, a convergence study was not conducted.

Blades missing in fracture analyzes: The blades were not included in the fracture analyzes, since the upscaled test model geometry was kept. In addition to influencing the displacements, the blades will likely reach the wave crest before the nacelle, which mean less displacements are allowed before capsizing occur.

Divergence from hydrodynamic intervals in DNV: The hydrodynamic coefficient were chosen on the basis of fitting model tests, and in the process, these exceeded the intervals specified by DNV.

10
Conclusion

A validation of the in-house hydro-elastic routine SOFIA was achieved numerically through ANSYS Inc., and for the first time through physical model tests, using the TLB B concept. In addition, the stream function wave theory was implemented as an add-in to SOFIA, so that every regular wave case could be analyzed.
Through the validation process, the hydro dynamic coefficients in the relative version of the Morison equation was analyzed through a parameter study, and determined for the TLB B. As a result further analyzes could be made, which accurately depicted the dynamic response of the TLB B.
In order to further extend the applicability of the numerical TLB B test model results, the Froude scaling method was utilized to create a full size TLB B model. The full size model was numerically validated in SOFIA, meaning that a hydro dynamically accurate full size simulation could be made of the TLB B in SOFIA.

As aforementioned, the primary goal of this thesis was to optimize a TLB with regards to stabilization failure. This was achieved through a mooring line fracture analysis of the TLB B in SOFIA.
Analyzes were made using an embedded extreme wave scenario, based on statistical data. The upper and lower placed mooring lines most likely to fracture were determined, and the original TLB B design was analyzed on the bases that capsizing should be avoided when a mooring line fractured. This was done through evaluation of the displacements and the normal forces in the mooring lines.
The original TLB B capsized with fracture of either mooring line, and therefore a different configuration of the TLB B mooring lines were needed. Four different configurations were analyzed and one proved to be sufficiently stable to avoid capsizing, when the upper mooring line fractured. This was the configuration where the lower mooring line footprint was reduced to a radius of 100m.
It was shown that reducing the radius of the lower mooring line footprint resulted in smaller deflections and rotations, in addition to avoidance of capsizing. The added stability was achieved due to the lower mooring lines ability to keep the bottom of the TLB B sufficiently submerged, which suggest that adding additional factors to this goal, like an additional mooring line placed vertically between TLB B bottom and the sea bed, could further improve stability. In addition, the eigenfrequencies were improved in that the deviations from the critical excitation range of the Academic Wind Turbine 5MW were increased.
It should be noted that the added stiffness of the reduced footprint also had the negative consequence of reducing fatigue life of the most critically loaded mooring lines.

Bibliography

[1] Andersen, T. L., Frigaard, P., Burcharth, H. F. (2014). "Water Wave Mechanics". *Aalborg University.*

[2] Andersen, T. L., Frigaard, P. (2014). "Analysis of Waves Technical Documentation for WaveLab 3". *Aalborg University.*

[3] Andersen, L. T. (2015) "WaveLab 3.66".*Aalborg University*

[4] ANSYS Inc. (2014). "ANSYS Manual - 12.8.6 Morison". *ANSYS*

[5] A. P. Institute (2000). "Recommended Practice for Planning, Designing and Constructing Fixed Offshore Platforms". *API.*

[6] A. P. Institute(2000). "Recommended Practice for Planning, Designing and Constructing Offshore Platforms - Working Stress Design". *API, Washington*

[7] Berg, J. M. (2013) "Experimental and Computational Study of Tension Leg Buoy Concepts for Floating Wind Turbines". *Norwegian University of Life Sciences*

[8] Bachynski, E. (2014). "Design and Analysis of Tension Leg Platform Wind Turbines". *Norwegian University of Science and Technology.*

[9] Blue H Engineering (2007). `http://www.bluehengineering.com/historical-development.html`. Downloaded: 28/9/2015.

[10] Brorsen, M. (2007). "Non-linear Waves". *Aalborg University.*

[11] Bunschoten, J., Bosma, T. (2014) "Electrifying the future", *DNV GL.*

[12] Burcharth F. H. (2002). "Strøm of Bølgekræfter på stive legemer, 2. udgave". *Laboratoriet for Hydraulik og Havnebygning, AUC, Aalborg*

[13] Butterfield, S., Musial, W., Jonkman, J., Sclavounos, P., (2007) "Engineering Challanges for Floating Offshore Wind Turbines".*National Renewable Energy Laboratory*

[14] Chakrabarti, K. S. (1987). "Hydrodynamics of Offshore Structures". *CBI Industries Inc..*

[15] Chakrabarti K. S. (2005). "Handbook of Offshore Engineering: Texte Imprimé, 1st edition" *Elsevier*

[16] Cook, D. R. et al. (2001) "Concept and Applications of Finite Element Analysis, 4th edition". *Wiley.*

[17] Chrolenko, M. O. (2013). "Dynamic Analysis and Design of Mooring Lines". *Norwegian University of Science and Technology.*

[18] Damgaard M., Bayat L., Andersen V. L., Ibsen B. L. (2014). "Assessment of the dynamic behaviour of saturated soil subjected to cyclic loading from offshore monopile wind turbine foundations" *Elsevier*

[19] DNV GL (2014) "Design of Offshore Wind Turbine Structure(DNV-OS-J101". *Det Norske Veritas*

[20] DNV GL (2014) "Design of Floating Wind Turbine Structures (DNV-OS-J103)". *Det Norske Veritas*

[21] Engebretsen, E. (2012). "Wave Conditions for Offshore Wind Turbine Foundations in Intermediate Water Depths". *Norwegian University of Science and Technology.*

[22] Energy.gov (2014). http://energy.gov/articles/top-10-things-you-didn-t-know-about-offshore-wind-energy. Downloaded: 6/6/2016.

[23] epd, WindFloat Project (2000). http://ec.europa.eu/maritimeaffairs/policy/sea_basins/atlantic_ocean/atlanticforum/events/brest/presentations/forum_brest_maciel_en.pdf. Downloaded: 28/9/2015.

[24] European Commision (2014) European "Energy Security Strategy, Brussels". *Cummunication from the commission to the European Parliament and The Council.*

[25] EWEA, Deep Water (2013). http://www.ewea.org/fileadmin/files/library/publications/reports/Deep_Water.pdf. Downloaded: 6/6/2016.

[26] Goda, Y. (2009). "Random Seas and Design of Maritime Structures, 3rd edition". *World Scientific.*

[27] Hughes, S. A.(1993). Physical Models and Laboratory Techniques in Coastal Engineering. Advanced Series on Ocean Eng. (Vol. 7), World Scientific.

[28] IEC (2008) "IEC 1400-3 Ed.1: Wind turbines - part 3: Design requirements for offshore wind turbines".*International electrotechnical commission*

[29] Jonkman, J., Butterfield S., Musial W., Scott G. (2009). "Definition of a 5-MW Reference Wind Turbine for Offshore System Development". *National Renewable Energy Laboratory*

[30] Journée, J.M.J.; Massie, W.W. (2001) "Offshore Hydromechanics, 1st edition". *Delft University of Technology.*

[31] Kjemperud S., Professor Larsen M. C. (Supervisor) (2011). "Hydrodynamic Coefficients for Wellhead Structures, 1st edition" *NTNU*

[32] Krenk, Steen (2009) "Non-linear Modeling and Analysis of Solids and Structures".*Cambridge University.*

[33] Liu, Z., Frigaard, P. (2001). "Generation and Analysis of Random Waves, 3rd edition". *Aalborg University.*

[34] Matha, D. (2009). "Model Development and Loads Analysis of an Offshore Wind Turbine Tension Leg Platform, whith a Comparison to other Floating Turbine Concepts". *University of Colorado.*

[35] Van Der Meulen, M. B., Ashuri, G. J., Van Bussel, W., Molenaar, D. P. (2015). "Influence of Nonlinear Irregular Waves on the Fatigue of an Offshore Wind Turbine". *Siemens Wind Power.*

[36] Munson, B. R., Okiishi, T. H., Huebsch, W. W. (2013). "Fundamentals of Fluid Mechanics, 7th edition". *Wiley.*

[37] Myhr, A., Bjerkseter, C., Ågotnes, A., Nygaard, T. A. (2014). "Levelised costs of energy for offshore floating wind turbines in a life cycle perspective". *Norwegian University of Life Sciences.*

[38] Myhr, A., Nygaard, T. (2015). "Comparison of Experimental and Computational Tension-Leg-Buoy Offshore Wind Turbines". *The International Society of Offshore and Polar Engineers.*

[39] Myhr, A., Nygaard, T. (2014). "Experimental Results for Tension-Leg-Buoy Offshore Wind Turbine Plateforms". *The International Society of Offshore and Polar Engineers.*

[40] Ningsu, Luo, Yolanda, Vidal, Leonardo, Acho (2015). "Wind Turbine Control and Monitoring" *Springer, Spain*

[41] T. A., Nygaard, et al. (2013) "Wave tank testing of Tension-Leg-Buoy (TLB) offshore wind power platforms".*Institute of Energy Technology, Norway*

[42] Pedersen, Andersen, Aage (2008). "Grundlæggende Skibs-og Offshoreteknik, 8. udgave". *Department of mehanical engineering, DTU*

[43] Rainey, J. P., Camp R. T. (2007) "Constrained non-linear waves for offshore wind turbine design". *Garrad Hassan & Partners, Bristol UK*

[44] Rottinger M. (1999). `http://www.iue.tuwien.ac.at/phd/rottinger/node33.html`. Downloaded: 6/6/2016.

[45] Sclavounos, P., Lee, S., DiPietro, J., Musial, W. (2010). "Floating Offshore Wind Turbines: Tension Leg Platform and Taught Leg Buoy Concepts Supporting 3-5MW Wind Turbines". *European Wind Energy Conference, Warsaw.*

[46] Sehovic E., Hansen, U. R., Trolle J., Kantharaja S., Rasmussen B. (2015) "Analysis of a Slip Joint Connection on a Monopile Foundation for Offshore Windturbines". *Aalborg University*

[47] Statoil Hywind (2012). `http://www.statoil.com/en/TechnologyInnovation/NewEnergy/RenewablePowerProduction/Offshore/Hywind/Downloads/Hywind_nov_2012.pdf`. Downloaded: 28/9/2015.

[48] Technip (2009) "Hywind substructure project Offshore Norway". `http://www.sidetp.org/espace_ingenieurs/professions/Petrole/TechnipHywind.pdf`. Downloaded: 28/9/2015.

[49] Tracy, C. (2007). "Parametric Design of Floating Wind Turbines". *Massachusetts Institure of Technology* .

[50] Techet, A. H. (2005). `http://ocw.mit.edu/courses/mechanical-engineering/2-016-hydrodynamics-13-012-fall-2005/readings/2005reading6.pdf`. Downloaded: 6/6/2016.

[51] Wayman, E., Sclavounos, P., Butterfield, S., Jonkman, J., Musial, W. (2006). "Coupled dynamic modeling of floating wind turbine systems". *National Renewable Energy Laboratory.*

[52] Wehmeyer, C. (2014) "A Floaing Offshore Wind Turbine in Extreme Wave Conditions". *Aalborg Universitet.* Ph.D-thesis ISBN 978-87-93237-40-7 (e-book).

[53] Wehmeyer, C. (2013). "Extreme analysis of wind". *Aalborg University.*

[54] Wehmeyer, C., Ferri, F., Skourup, J., Frigaard, P. B. (2013). "Experimental Study of an Offshore Wind Turbine TLP in ULS Conditions". *Aalborg University.*

[55] Z. Qi, X. Kong, G. Wang (2015) "Identifying Critical Loads of Frame Structures with Equilibrium Equations in Rate Form". Downloaded: 6/6/2016.

[56] Aalborg University (2015). "Lecture 9: Theory for waves with finite height". *Aalborg University.*

A

Appendix

A.1 Academic Wind Turbine 5MW

Design of offshore wind turbine foundations, even if they are floating or fixed to the seabed, is depending on the loads it has to withstand. Wind loads will be transferred through the wind turbine and applied at the foundation in terms of interface loads. It is therefore important to specify the exact dimension of the wind turbine to include all effects. The wind turbine that will be modelled in this project will be based on the 5MW wind turbine, designed by the National Renewable Laboratories. The wind turbine is based on published documents from wind turbine manufactures, but since most detailed data is secret, NREL has mixed available data with data from conceptual models [29]. The general wind turbine specifications are stated in the table below.

Wind Turbine Dimensions	**Unit**	
Rating	$[MW]$	5
Rotor orientation	$[-]$	Upwind, 3 Blades
Control	$[-]$	Variable speed, Collective pitch
Drivetrain	$[-]$	High speed, Multiple-stage gearbox
Rotor, Hub diameter	$[m], [m]$	126.3
Hub height	$[m]$	90
Cut-in, Rated, Cut-out (Wind speed)	$[\frac{m}{s}], [\frac{m}{s}], [\frac{m}{s}]$	3, 11.4, 25
Cut-in, Rated (rotor speed)	[rpm], [rpm]	6.9, 12.1
Rated tip speed	$[\frac{m}{s}]$	80
Overhang, Shaft tilt, Procone	$[m]$, [deg], [deg]	5, 5, 2.5
Tower-top mass	$[kg]$	110000
Nacelle mass	$[kg]$	240000
Tower mass	$[kg]$	225540
Coordinate location of overall COG	$[m]$	(-0.2, 0.0, 64.0)
Density of tower	$[[\frac{kg}{m^m}]]$	8500
Young's modulus	$[MPa]$	210000
Shear modulus	$[MPa]$	80800

Table A.1: Properties of the NREL 5MW wind turbine [29]

B

Appendix

Following Appendix covers appendices connected to chapter 3.

B.1 Irregular Sea State

Modeling a realistic representation of wind generated waves and swells, requires an introduction of irregular waves. Irregular waves are based on linear wave theory known from regular waves, but instead arranged in a probabilistic setup, in order to describe that the sea by nature is random and never produce the same elevation history twice.The multidirectional irregular wave surface is described from the energy spectrum and the directional spreading function [2].

Through previous research it has been proved that a more detailed description of the surface history can be established with basis nonlinear irregular waves [35]. As a result it should be possible to lower the safety factors that have to be added to the linear irregular waves and therefore make an offshore design that is less conservative.

B.1.1 Wave spectra and linear time realizations

In the description of irregular waves it is very often assumed that waves are fully wind generated, which causes that two different theories of establishing the energy spectrum can be used

- Pierson-Moskowitz spectrum (PM)
- Joint North Sea Wave Project (JONSWAP)

The PM spectrum is used in describing fully developed waves, which is the result, if a wind has been blowing steadily for a long time period. Investigation of the waves in the North Sea has shown that the waves never fully develop, but instead continue their development through a nonlinear wave-wave interaction. The JONSWAP is thus a modification of the PM spectrum with an artificial factor (peak enhancement factor) multiplied in order to make a better fit of the waves in the North Sea. Since it is assumed to focus of FOWT in the North Sea, the JONSWAP spectrum is used for describing irregular waves.

$$S_\eta(f) = \alpha(H_{m0})^2 {f_p}^{-5} \exp(\frac{5}{4}(\frac{f_p}{f})^4)\gamma^\beta \tag{B.1}$$

where α is a factor given by

$$\alpha = \frac{0.0624}{0.230 + 0.0336\gamma - (\frac{0.185}{1.0+\gamma})} \tag{B.2}$$

and β is a factor given by:

$$\beta = \exp(-\frac{f - f_p}{2\sigma^2 {f_p}^2}) \tag{B.3}$$

where σ is the spectral width parameter, 0.7 for $f < f_p$ and 0.9 for $f > f_p$. In SOFIA for simulating floating offshore structures the peak enhancement factor can be chosen from 0 to 7, where 0 produces linear regular waves and 3.3 is the preferred peak enhancement factor for irregular waves in the North Sea [2].

As mentioned, establishment of the multidirectional wave spectrum requires the introduction of a spreading function, which describes the directional spreading of the waves. According to calculation input parameters, different types of spreading functions can be chosen. In SOFIA, the spreading function proposed by Lonquet-Higgins are used [33]

$$D(\theta) = \frac{2^{2s-1}}{\pi} \frac{\Gamma^2(s+1)}{\Gamma(2s+1)} \cos^2(\frac{\theta - \theta 0}{2}) \tag{B.4}$$

The variable s is called the spreading parameter. The multidirectional spectrum is finally given by multiplication of the spreading function and the energy spectrum, which in this case is the JONSWAP spectrum [33]

Estimation of the spreading parameter

The directional wave spreading is greatly affected by refraction and diffraction, which means that the spreading parameter is very dependent on site conditions at the site location. Observations have shown that following relation to the wind speed can be set up.

$$s_{max} = 11.5(\frac{2\pi f_p U}{g}) \tag{B.5}$$

Utilization of eq. (B.5) makes it possible to relate s_{max} with $\frac{H}{L}$ for deep water scenarios, which leads to following recommendation spreading parameters:

$$s_{max} = \begin{cases} \text{Wind Waves} \\ \text{Swell with short decay distances} \\ \text{Swell with long decay distances} \end{cases}$$

Due to the interest of investigating cases of intermediate- and shallow water depths, the just mentioned spreading parameters is not reliable. When waves propagate towards the shore, the length of the crests tends to increase which is associated with the decrease of directional spreading of wave energy. Therefore also the directional wave spectrum has transformed. The transformation depends of the bathymetry of the seabed and in areas where the topography of the seabed is represented by straight contour lines. Figure B.1 can be used for estimation of the spreading parameter [26].

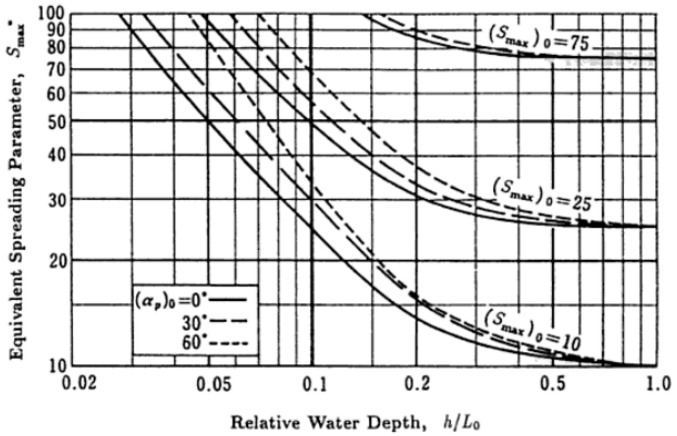

Figure B.1: Estimation of spreading parameter in shallow- and intermediate water [26].

After estimation of the spreading parameter a representation of the multidirectional spectrum can be generated. The figure below shows an example of a multidirectional wave spectrum, for the case: $H_S = 9m$, $T_P = 10s$, and $s = 10$

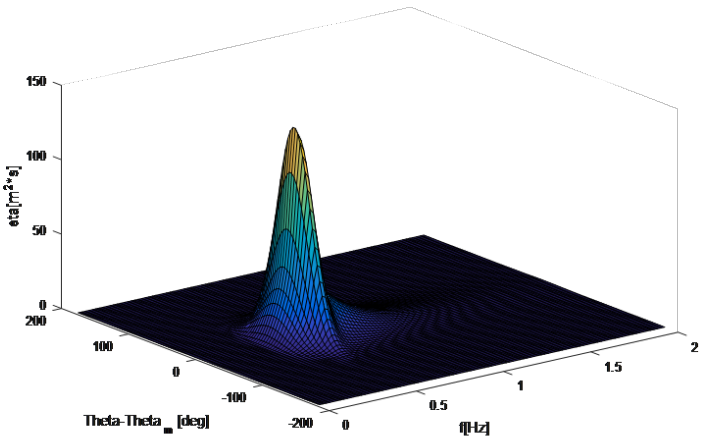

Figure B.2: Multidirectional spectrum

Generation of multidirectional linear waves

From the multi-directional spectrum it is possible to perform an inverse spectrum analysis, by defining the spectral density as [1],

$$S(f|\theta) = \frac{\frac{1}{2}a^2}{\Delta f \Delta \theta} \tag{B.6}$$

where a is the amplitude, Δf is the frequency band and $\Delta\theta$ is the spreading band. From eq. (B.6) it is possible to solve the amplitude,

$$a_{m,n} = \sqrt{2S_\eta(f|\theta)\Delta f \Delta\theta} \tag{B.7}$$

The surface elevation η can then be determined from,

$$\eta = \sum\sum a_{m,n}\cos(k_m x\cos(\theta_n) + k_m y\sin(\theta_n) - 2\pi f_m t + \varepsilon_{m,n} \tag{B.8}$$

B.2 Validation of the Stream Function Routine

The stream function add-in utilized in the project is developed for the purpose of conducting simulations of FOWT, in areas where waves need a more realistic description than the linear theory. Furthermore it will increase the increase the coverage of SOFIA.

This appendix is considering the validation of the raw stream function routine before implementation in the SOFIA and an initial validation of the stream function wave add-in implemented in SOFIA.

The focus of the validation is to ensure the reliability of the Newton-Raphson solver, and the particle kinematics. The particle kinematics are validated through example considering a monopile structure.

B.2.1 Validation of the Newton-Raphson Solver

The theoretical background behind the Newton Raphson solver is found in the main report, chapter 3, and is therefore not considered in this appendix. To validate the Newton-Raphson solver, 9 different load cases are simulated.

Table B.1: Wave Load Cases

Hydrodynamic Load Case (L)	H $[m]$	Current $[\frac{m}{s}]$	T $[s]$	Depth $[m]$	Required Wave Theory	Order of Stream Function (N)
L1	2.5	0	55	500	Stream Function	3
L2	4.5	0	25	30	Stream Function	7
L3	9	0	10	37.5	Stream Function	7
L4	13	0	10	30	Stream Function	15
L5	8	0	10	12	Stream Function	35
L6	10	0	40	16.7	Stream Function	50
L7	12.5	0	42	16.7	Stream Function	70
L8	13	2	10	30	Stokes 5th order	15
L9	13	-2	10	30	Stokes 5th order	15

The wave load cases are ranging from deep water to very shallow water, in order to ensure that the stream function routine is able to describe all wave theories as expected. The required wave theory is determined by use of the applicability diagram in chapter 3.

The validation is performed with respect to the commercial in-house software WaveLab [3] and the results are listed in Table B.1.

		Cr	Ca	B1	B2	Eta1	Eta2	Eta3	Q	R	L
L1											
	Stream	62.281	62.281	-107.449	-0.176	1.254	-0.005	-1.245	-31140.697	1939.507	3425.490
	Wavelab	62.266	62.266	-107.405	-0.176	1.255	-0.005	-1.245	-31132.775	1938.519	3424.620
	Difference(%)	0.024	0.024	0.041	0.000	0.080	0.000	0.000	0.025	0.051	0.025
L2											
	Stream	16.877	16.877	-82.682	-12.081	2.882	2.285	1.023	-504.895	142.746	421.930
	Wavelab	16.873	16.873	-82.651	-12.073	2.882	2.285	1.023	-504.783	142.683	421.830
	Difference(%)	0.024	0.024	0.038	0.066	0.000	0.000	0.000	0.022	0.044	0.024
L3											
	Stream	14.983	14.983	-69.303	-2.164	5.122	4.339	2.486	-555.279	112.576	149.827
	Wavelab	14.978	14.978	-69.275	-2.162	5.122	4.339	2.486	-555.107	112.506	149.780
	Difference(%)	0.032	0.032	0.040	0.093	0.000	0.000	0.002	0.031	0.062	0.032
L4											
	Stream	14.933	14.933	-93.743	-8.667	8.291	7.759	6.446	-434.927	112.570	149.331
	Wavelab	14.929	14.929	-93.705	-8.661	8.291	7.759	6.446	-434.805	112.507	149.290
	Difference(%)	0.027	0.027	0.041	0.070	0.001	0.002	0.003	0.028	0.056	0.027
L5											
	Stream	11.373	11.373	-43.016	-11.050	6.250	5.818	5.044	-131.575	65.709	113.734
	Wavelab	11.371	11.371	-43.022	-11.052	6.249	5.822	5.049	-131.544	65.684	113.710
	Difference(%)	0.021	0.021	0.014	0.015	0.016	0.061	0.085	0.023	0.039	0.021
L6											
	Stream	15.150	15.150	-107.216	-48.578	9.179	8.334	6.579	-249.706	115.582	606.009
	Wavelab	15.147	15.147	-107.191	-48.565	9.179	8.335	6.580	-249.652	115.533	605.880
	Difference(%)	0.021	0.021	0.023	0.027	0.002	0.002	0.009	0.022	0.043	0.021
L7											
	Stream	15.646	15.646	-108.446	-50.402	11.722	10.173	8.001	-257.581	123.220	657.140
	Wavelab	15.643	15.643	-108.421	-50.389	11.722	10.173	8.001	-257.525	123.166	657.000
	Difference(%)	0.020	0.020	0.023	0.026	0.001	0.002	0.008	0.022	0.043	0.021
L8											
	Stream	15.523	17.523	-105.331	-11.785	8.366	7.842	6.523	-453.084	121.816	175.226
	Wavelab	15.519	17.519	-105.292	-11.778	8.366	7.842	6.522	-452.966	121.752	175.190
	Difference(%)	0.023	0.020	0.037	0.063	0.003	0.003	0.002	0.026	0.052	0.020
L9											
	Stream	14.130	12.130	-79.508	-6.079	8.367	7.711	6.253	-410.401	100.519	121.296
	Wavelab	14.125	12.125	-79.468	-6.075	8.367	7.711	6.252	-410.273	100.456	121.250
	Difference(%)	0.033	0.038	0.051	0.068	0.003	0.003	0.010	0.031	0.062	0.038

Figure B.3: Comparison of coefficients iterated by the Newton-Raphson solver

By investigating the iterated coefficients from the stream function routine, with respect to coefficients determined by WaveLab [3], it is seen that the deviation for all 9 load cases are very low. A difference <1% concludes the programmed Newton-Raphson solver is reliable.

B.2.2 Estimation of Morison loads

A validation of the particle kinematics is performed by setting up a monopile example, where wave loads are determined by use of the Morison equation.

$$F = \rho C_m V dotu + \frac{1}{2}\rho C_d A u|u| \tag{B.9}$$

The standard form of the Morison equation is stated in eq. B.10 and implemented in the raw stream function routine and is due to its simplicity, only able to handle bottom fixed structures exposed to small displacements, such as a monopile. Since ANSYS Inc. and the SOFIA are prepared to handle floating structures, the relative form of the Morison equation is implanted in those routines.

$$F = \rho V dotu + \rho C_a V(\dot{u} - \dot{v} + \frac{1}{2}\rho C_d A u - v|u - v| \tag{B.10}$$

For the following examples considering the monopile, the structural motions are small and the added mass is neglected, which implies that the relative form of the Morison equation turns in to the normal Morison equation.

B.2.2.1 Validation model

In order to reduce the sources of error in the validation of the stream function routine, a simple monopile model with cylindrical shape and constant cross section is chosen. The model is illustrated with outer dimensions and wave properties in Figure B.4.

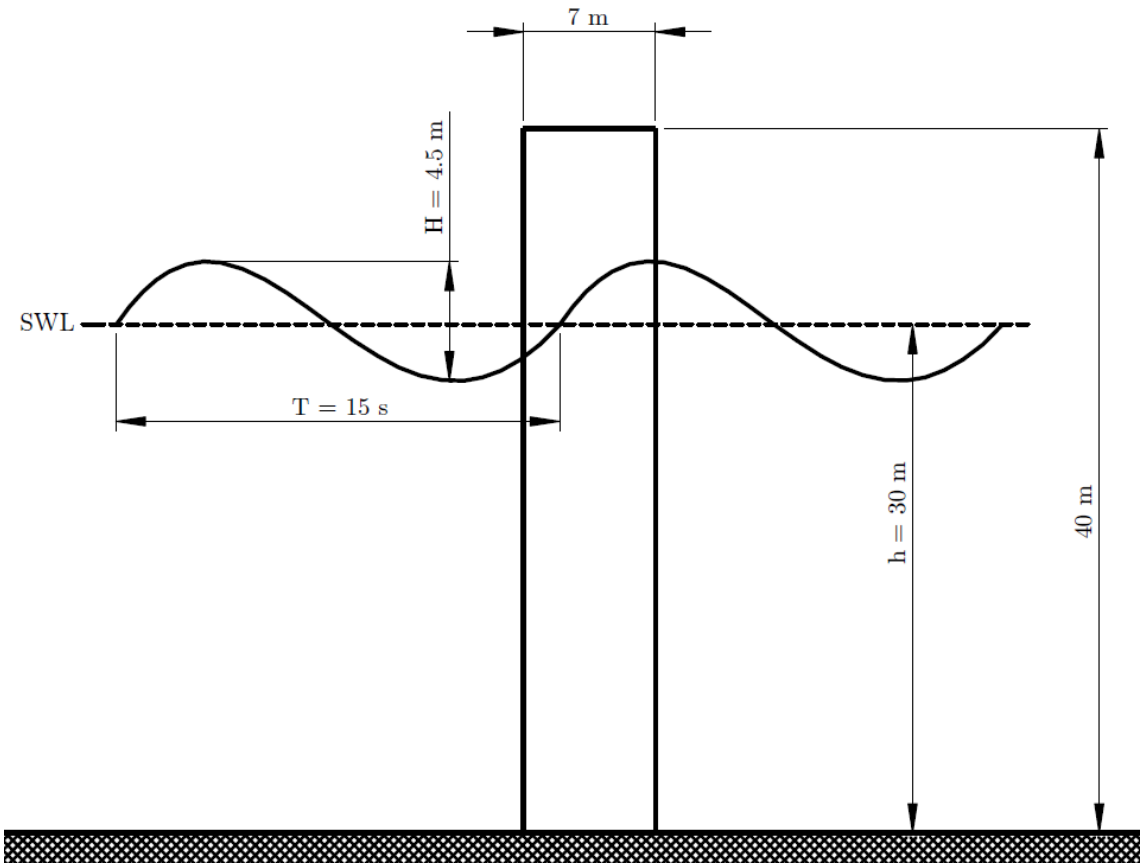

Figure B.4: Comparison of coefficients iterated by the Newton-Raphson solver

The monopile model is used as reference geometry for all example setups during the validation of the stream function routine routine and wave add-in. In Table B.4, is listed settings used in the validations.

	Unit	Validation settings
Outer diameter	$[m]$	7
Inner diameter	$[m]$	6.5
Length	$[m]$	40
Number of elements	$[-]$	21
Structural density	$[\frac{kg}{m^3}]$	7850
Water density	$[\frac{kg}{m^3}]$	1025
Drag coefficient, CD	$[-]$	1
Inertia coefficient, Cm	$[-]$	2

Table B.2: Validation settings

During the validation process three different wave load cases are used. The wave properties stated in Figure B.4 are used for the validation of the stream function routine before it is

implemented in SOFIA as a wave add-in (Example 1). Here is 2nd order wave theory or better is required, to describe the wave load case.

B.2.3 Example 1 - Validation of particle kinematics before implementation in SOFIA

For the given wave load case, the stream function routine is compared to Ocean Commands ANSYS Inc. and a programmed 5th order wave routine. In both the stream function and ANSYS, it should be mentioned that the wave are simulated by use of a stream function order of N = 7, In ANSYS it is not possible to plot Morison loads directly, but since the structure is only exposed the wave loads the reaction force in the direction of the wave propagation, with opposite sign, is used.

To refine the load plots, the initial noise caused by the numerical approach is removed.

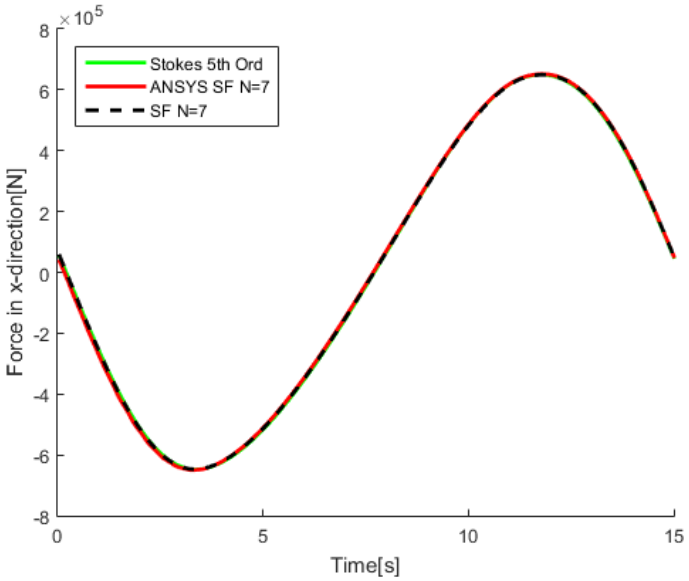

Figure B.5: Load comparison between following programs: Stream function routine, ANSYS and 5th order routine

By investigating the comparison it is shown that the loads determined in ANSYS, the Stream Function routine and in the 5th order routine has a very close fit.

B.2.4 Example 2 - Validation of particle kinematics after implementation in SOFA

Validation of the wave add-in is finally conducted in the general validation of SOFIA, while this validation is an initial validation of the wave add-in to ensure the particle kinematics and the solver is implemented correct.

The geometry and system settings is there found in section B.2.2.1, but the wave realization is changed to a 1st order problem.

Table B.3: Validation settings

	Unit	Wave properties
Wave height, H	$[m]$	0.2
Wave period, T	$[s]$	10
Water depth, h	$[m]$	30

The reason for the choice of a first order problem is due to that, it is interesting to compare the stream function wave add-in, to as many other routines as possible. In this case the stream function add-in is again compared to Ocean Commands in ANSYS Inc. (Setup simulate a first order wave by use of the stream function and 1st order theory), The programmed 5th order wave routine, the standard wave add-in and the stream function routine unaffected from SOFIA. In the stream function routine the order is set to N = 5.

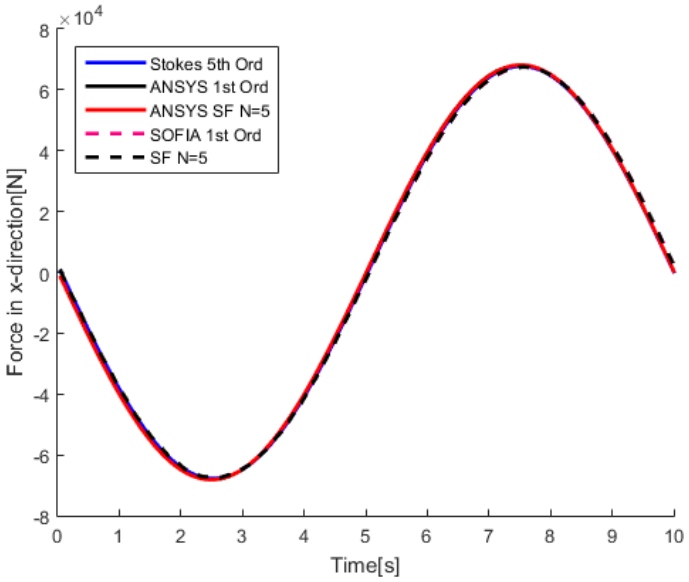

Figure B.6: Comparison of wave loads after implementation in SOFIA

As in ANSYS, then the Morison load in SOFIA is found as a reaction forces. By investigating the comparison, it is shown that all the routines are located very close to each other. The slightly difference is presumably due to small differences in the numerical routines.

Furthermore a comparison between ANSYS (stream function N = 7) and the stream function add-in, is performed for a 2nd order wave problem. The 2nd order wave load case is the same as shown in Figure B.4.

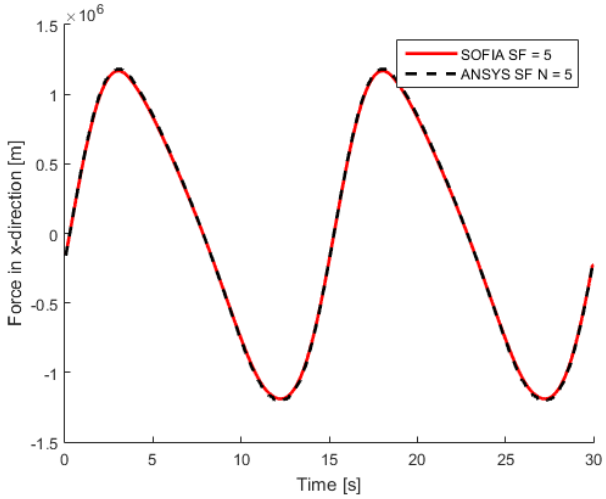

Figure B.7: Comparison of 2nd order wave loads

Also for this wave load case is the results located very close.

Through the implementation of the stream function routine in the SOFIA, the coordinates along the x-axis is included in the determination of the wave parameters, such as the particle kinematics. This is due to the handling of floating structures. So in order to verify the ability of the wave add-in, to handle floating structures, the 2nd order wave load case from Table B.4 is used. Geometry and setting are shown in Figure B.4 and in Table B.4. The cylinder is constrained such it is only able to float sideways.

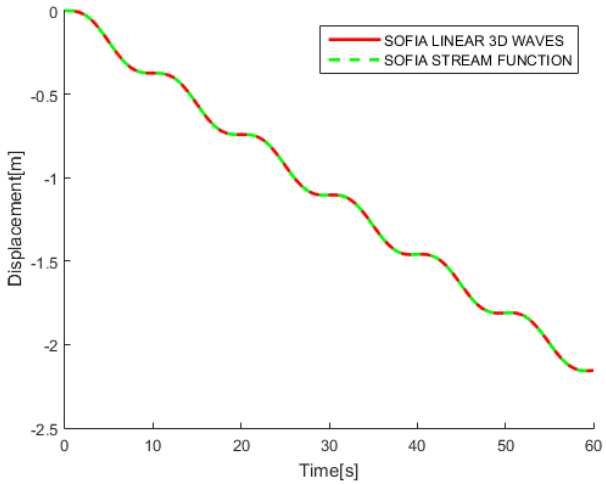

Figure B.8: Comparison of displacements

In Figure B.8 is shown the displacement of the floating cylinder with waves applied through the standard wave add-in in SOFIA and the stream function wave add-in.

B.2.5 Example 3 - Validation of the implemented stream function add-in with current and wave loads applied

By using the stream function wave theory is possible to conduct simulations with a uniform current applied. To validate the stream function add-ins ability to simulate higher order waves and include a uniform current, following wave load case is investigated.

Table B.4: Validation settings

	Unit	Wave properties
Wave height, H	$[m]$	13
Wave period, T	$[s]$	10
Water depth, h	$[m]$	13
Water depth, h	$[m]$	1

The wave properties produce a 5th order wave with a uniform current at 1 m/s applied. In order to produce variation, an example of waves with co-current and countercurrent are investigated. Once again the monopile geometry and setup from section B.2.2.1 are used.

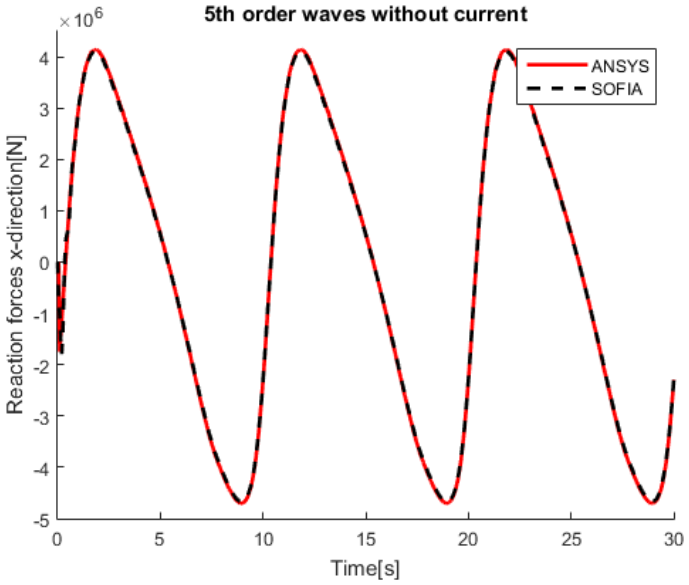

Figure B.9: 5th order waves without current

Before establishing a comparison between ANSYS and MATLAB with a current applied, the wave load case with, only a 5th order wave exposed to the monopile is compared. As shown in Figure B.9 a very a close fit occurs. The first example with current applied is the case with a co-current flow on 1m/s.

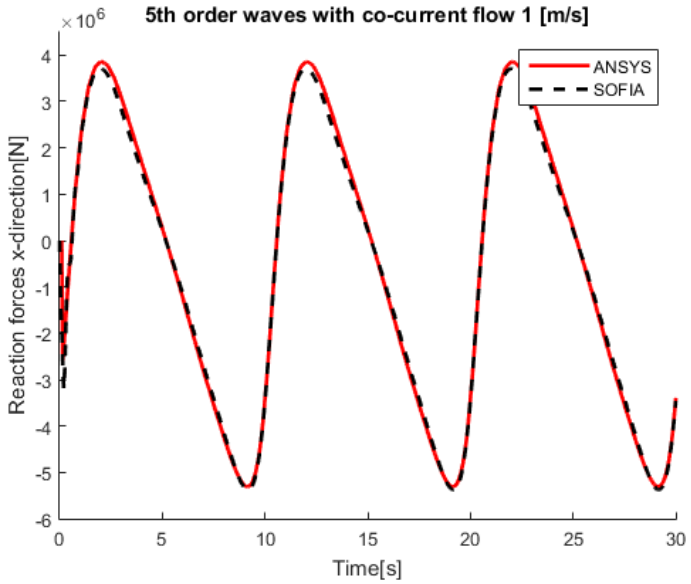

Figure B.10: 5th order waves with co-current flow 1 [m/s]

It is seen that the loads in the amplitudes estimated by SOFIA varies slightly from the ANSYS model, which could indicate small numerical differences in the model setup. In the following case the current is switched 180°, such a countercurrent is produced according to the waves.

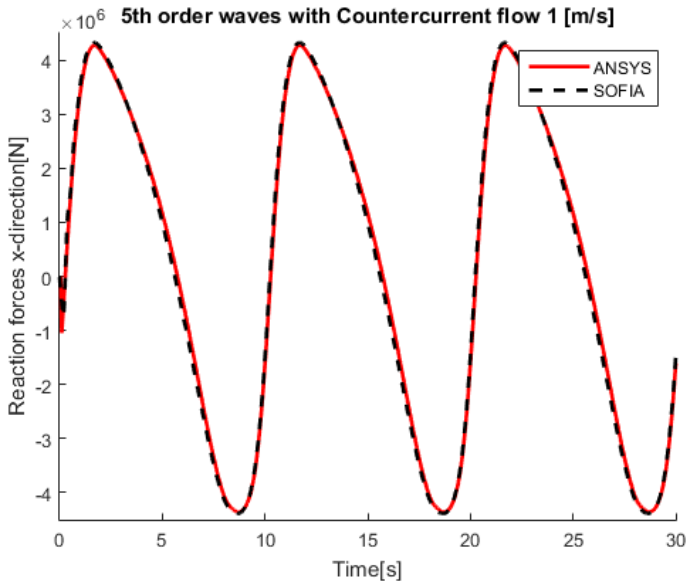

Figure B.11: 5th order waves with countercurrent flow 1 [m/s]

For this case the variation between SOFIA and the ANSYS model not represented.

B.2.6 Comments on the validation

Through this validation the raw stream function routine has been validated, as well as an initial validation of the stream function add-in has been conducted. Results have shown that the stream function routine is modeled correct and it is able to iterate correct stream function parameters. Likewise it is shown that the routine is able to estimate particle kinematics that matches those estimated in other routines.

C

Appendix

This appendix is dedicated to further explain the theory behind the corotational beam theory and the non-linear Newmark solver.

C.1 Corotational beam theory

Unlike regular beam theories where deformations and rotations are defined with reference to the global coordinate system, the corotational beam theory uses element based local coordinate systems. The deformations and rotations of each element is a sum of the rigid body motions of the element based local reference coordinate system and the local deformations of each beam element within the local reference coordinate system, as illustrated in Figure C.1. **(1)** is the undeformed element. **(2)** shows the element after rigid body translations and rotations. Note that the local reference coordinate system is always located with equal distance to the element ends A and B. **(3)** illustrates the local deformations of the element in the local reference coordinate system. These deformations are the strain inducing deformations. [32].

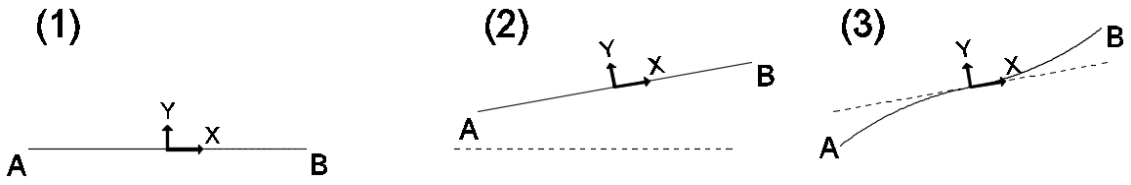

Figure C.1: Deformation and rotation concept of the corotational beam theory, shown in 2D for illustrative simplicity. [32]

Since the resulting deformations and rotations are analyzed in two parts, it would be natural to think the number of required motion components needed in the corotational beam theory should be double that of regular beam theories. However this is not necessary. The corotational beam theory can depend on just 12 motion components, like regular beam theories. Six of the components are related to the rigid body motions. These are three directional translations (x, y, z), and three rotations at the point of the local reference coordinate system. The other six components are responsible for the strain inducing local deformations, and these are expressed through the six natural deformation modes seen on Figure C.2

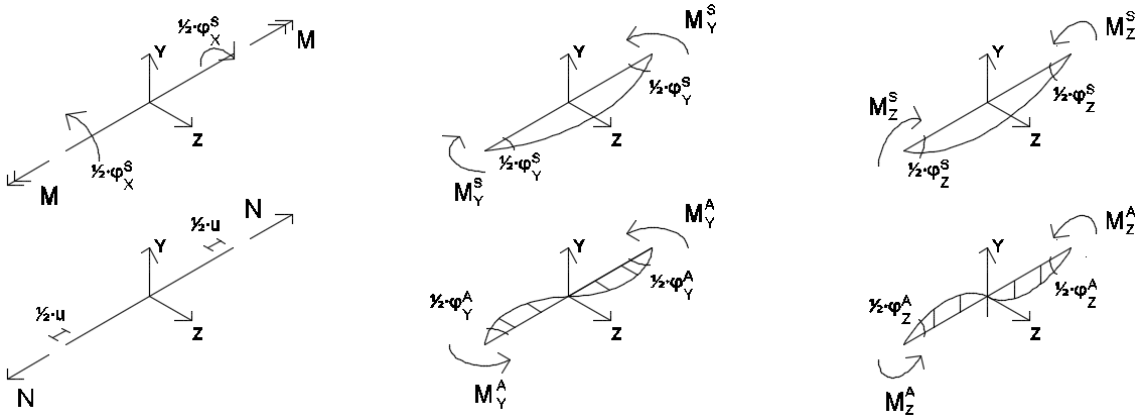

Figure C.2: Natural deformation modes of symmetric beam elements. The first row shows the three modes with constant moment and the second row shows the three modes with internal force. Note that ϕ and u denotes angles and elongations, and not the deflections acting on the beams. [32]

These six natural deformation modes can be used to determine the twelve element forces through the transformation matrix $[S]$. Construction of the transformation matrix requires the implementation of three unit vectors n_x, n_y, and n_z. These unit vectors are [1 0 0], [0 1 0], and [0 0 1] respectively in the local coordinate system. [32]

$$\underset{12\times 1}{\begin{bmatrix} f_A \\ m_A \\ f_B \\ m_B \end{bmatrix}} = \underset{12\times 6}{\begin{bmatrix} 0 & 0 & 0 & -n_x & -2n_z/L & 2n_y/L \\ -n_x & -n_y & -n_z & 0 & n_y & n_z \\ 0 & 0 & 0 & n_x & 2n_z/L & -2n_y/L \\ n_x & n_y & n_z & 0 & n_y & n_z \end{bmatrix}} \underset{6\times 1}{\begin{bmatrix} M \\ M_y^s \\ M_z^s \\ N \\ M_y^a \\ M_z^a \end{bmatrix}} \tag{C.1}$$

C.1.1 Element stiffness

Using the twelve element forces and the six natural deformation modes, the element stiffness can be found. The element stiffness matrix consists of input from two different kinds of stiffnesses. One is the stiffness responsible for the change of length and the rigid body motions. This is called the rotation stiffness matrix $[K_r]$. The other is the stiffness responsible for bending and torsion of the beam, and is a combination of the constitutive stiffness and the geometric stiffness. This stiffness is called the deformation stiffness $[K_d]$. Adding the rotation stiffness and the deformation stiffness as shown in eq. (C.2) gives the element stiffness.

$$[K_e] = [K_r] + [S][K_d][S]^T \tag{C.2}$$

The element stiffness is expressed through a 12×12 matrix and so is the rotation stiffness. The deformation stiffness is 6×6 matric since its properties are similar to those of regular beam theories. For the sake of simplicity and understanding it is convenient to express these matrices as consisting of 3×3 sub matrices as seen in eq. (C.3).

$$[K_r] = \begin{bmatrix} [K_{11}^r] & [K_{12}^r] & [K_{13}^r] & [K_{14}^r] \\ [K_{21}^r] & [K_{22}^r] & [K_{23}^r] & [K_{24}^r] \\ [K_{31}^r] & [K_{32}^r] & [K_{33}^r] & [K_{34}^r] \\ [K_{41}^r] & [K_{42}^r] & [K_{43}^r] & [K_{44}^r] \end{bmatrix} \qquad [K_d] = \begin{bmatrix} [K_1^d] & [K_2^d] \\ [K_3^d] & [K_4^d] \end{bmatrix} \tag{C.3}$$

Initially the rotation matrix is derived using the principle of virtual work. Since rigid body motions only satisfy equilibrium when considering the total forces and moments on the whole body, the force and moment components used to describe the rotational stiffness for each element results in non-symmetry, which is inconvenient computationally. However this lack of equilibrium in forces and moments for the individual element does not satisfy the corotational formulation where the rotation of both beam ends is the same. This means that element deformations can occur, and to counteract this, components of the deformation stiffness is used. Conveniently, the stiffness components needed to counteract these element deformations can be added so that the rotation stiffness becomes symmetric. The way of adding the deformation stiffness is shown in the equation below. With the deformation stiffness components the rotation matrix is called co-rotation matrix.

$$[K_r] = \begin{bmatrix} [K_{11}^r] & [K_{12}^r] + [K_1^d] & [K_{13}^r] & [K_{14}^r] - [K_1^d] \\ [K_{21}^r] & [K_{22}^r] + [K_2^d] & [K_{23}^r] & [K_{24}^r] - [K_2^d] \\ [K_{31}^r] & [K_{32}^r] + [K_3^d] & [K_{33}^r] & [K_{34}^r] - [K_3^d] \\ [K_{41}^r] & [K_{42}^r] + [K_4^d] & [K_{43}^r] & [K_{44}^r] - [K_4^d] \end{bmatrix} \tag{C.4}$$

The constitutive part of the deformation matrix can be determined from the usual parameters needed in regular beam theories, as seen in eq. C.5.

$$[K_{d,c}] = \begin{bmatrix} GJ & & & & & & \\ & EI_y & & & & & \\ & & EI_z & & & & \\ & & & EA & & & \\ & & & & 3\psi_y^a EI_y & & \\ & & & & & 3\psi_z^a EI_z & \end{bmatrix} \tag{C.5}$$

GJ is the St. Vernant torsion stiffness, EA the axial stiffness, EI representing stiffness of symmetric bending in y-, and z-direction, and $3\psi EI$ is the anti-symmetric bending modes in y-, and z-direction. The shear components ψ can be determined as seen in eq. (C.6) and eq. (C.7).

$$\psi_y^a = \frac{1}{1+\Phi_y}, \qquad \Phi_y = \frac{12EI_y}{L^2GA_z} \tag{C.6}$$

$$\psi_z^a = \frac{1}{1+\Phi_z}, \qquad \Phi_z = \frac{12EI_z}{L^2GA_y} \tag{C.7}$$

Where A is the effective area of the respective directional shear force.
The geometric stiffness component is in the corotational formulation expressed through the natural deformation modes as seen in eq. (C.8).

$$[K_{d,g}] = \begin{bmatrix} \delta\overline{\varphi}_s & \delta\overline{\varphi}_a \end{bmatrix} \begin{bmatrix} \frac{1}{12}L[N] & \frac{1}{4}\overline{M} \\ \frac{1}{4}\overline{M} & \frac{1}{20}L[N] \end{bmatrix} \begin{bmatrix} \delta\overline{\varphi}_s \\ \delta\overline{\varphi}_a \end{bmatrix} \tag{C.8}$$

Where $\overline{\varphi}$ are vectors representing the incremental rotation of the natural beam mode, $[N]$ is a matrix containing contribution from internal forces, and $\overline{M}$ is a matrix containing contribution from moments. These rotations, forces and moments are all seen Figure C.2 With the stiffness matrices determined, the element stiffness of each individual element can be found. The simplest way to illustrate the element stiffness is by using 3×3 sub matrices.

$$[K_e] = \begin{bmatrix} [K_{11}^e] & [K_{12}^e] & [K_{13}^e] & [K_{14}^e] \\ [K_{21}^e] & [K_{22}^e] & [K_{23}^e] & [K_{24}^e] \\ [K_{31}^e] & [K_{32}^e] & [K_{33}^e] & [K_{34}^e] \\ [K_{41}^e] & [K_{42}^e] & [K_{43}^e] & [K_{44}^e] \end{bmatrix} \tag{C.9}$$

The sub matrices can be seen here.

$$[K_{11}^e] = [K_{33}^e] = -[K_{13}^e] = -[K_{31}^e] = \begin{bmatrix} EAL^2 & -\frac{Q_y}{L} & -\frac{Q_z}{L} \\ -\frac{Q_y}{L} & 12\psi_z^a EI_z + \frac{6}{5}\frac{N}{L} & 0 \\ -\frac{Q_z}{L} & 0 & 12\psi_y^a EI_y + \frac{6}{5}\frac{N}{L} \end{bmatrix} \tag{C.10}$$

$$[K_{12}^e] = -[K_{32}^e] = \begin{bmatrix} 0 & 0 & 0 \\ \frac{m_y^A}{L} & \frac{M}{L} & \frac{6\psi_z^a EI_z}{L^2} + \frac{N}{10} \\ \frac{m_z^A}{L} & -\frac{6\psi_y^a EI_y}{L^2} - \frac{N}{10} & \frac{M}{L} \end{bmatrix} \tag{C.11}$$

$$[K_{21}^e] = -[K_{23}^e] = \begin{bmatrix} 0 & \frac{m_y^A}{L} & \frac{m_z^A}{L} \\ 0 & \frac{M}{L} & -\frac{6\psi_z^a EI_z}{L^2} - \frac{N}{10} \\ 0 & \frac{6\psi_y^a EI_y}{L^2} + \frac{N}{10} & \frac{M}{L} \end{bmatrix} \tag{C.12}$$

$$[K_{24}^e] = \begin{bmatrix} -\frac{GJ}{L} & \frac{LQ_y}{6} & \frac{LQ_z}{6} \\ \frac{LQ_y}{6} & \frac{(3\psi_y^a - 1)EI_y}{L} - \frac{LN}{30} & \frac{M}{2} \\ \frac{LQ_z}{6} & -\frac{M}{2} & \frac{(3\psi_z^a - 1)EI_z}{L} - \frac{LN}{30} \end{bmatrix} \tag{C.13}$$

$$[K_{42}^e] = \begin{bmatrix} -\frac{GJ}{L} & \frac{LQ_y}{6} & \frac{LQ_z}{6} \\ \frac{LQ_y}{6} & \frac{(3\psi_y^a - 1)EI_y}{L} - \frac{LN}{30} & -\frac{M}{2} \\ \frac{LQ_z}{6} & \frac{M}{2} & \frac{(3\psi_z^a - 1)EI_z}{L} - \frac{LN}{30} \end{bmatrix} \tag{C.14}$$

$$[K_{22}^e] = \begin{bmatrix} \frac{GJ}{L} & \frac{m_z^B - 2m_z^A}{6} & \frac{2m_y^A - m_y^B}{6} \\ \frac{m_z^B - 2m_z^A}{6} & \frac{(3\psi_y^a + 1)EI_y}{L} + \frac{2NL}{15} & 0 \\ \frac{2m_y^A - m_y^B}{6} & 0 & \frac{(3\psi_z^a + 1)EI_z}{L} + \frac{2NL}{15} \end{bmatrix} \tag{C.15}$$

$$[K_{44}^e] = \begin{bmatrix} \frac{GJ}{L} & \frac{m_z^A - 2m_z^B}{6} & \frac{2m_y^B - m_y^A}{6} \\ \frac{m_z^A - 2m_z^B}{6} & \frac{(3\psi_y^a + 1)EI_y}{L} + \frac{2NL}{15} & 0 \\ \frac{2m_y^B - m_y^A}{6} & 0 & \frac{(3\psi_z^a + 1)EI_z}{L} + \frac{2NL}{15} \end{bmatrix} \tag{C.16}$$

Where N is the internal normal force, M is the internal torsional moments, and Q_y and Q_z are internal shear forces that can be expressed through the external bending moments at the nodes. [32]

$$Q_y = \frac{(m_z^A + m_z^B)}{L}, \qquad Q_z = \frac{(m_y^A + m_y^B)}{L} \tag{C.17}$$

C.1.2 Global stiffness

As for regular beam theory, the global stiffness matrix is made by assembling the local element stiffness matrices in relation to their respective DOF, which has been converted to fit the global coordinate system. The conversion to the global coordinate system can be seen done through eq. (C.18).

$$[K_{e,R}] = [R_e][K_e][R_e]^T = \begin{bmatrix} [R] & 0 & 0 & 0 \\ 0 & [R] & 0 & 0 \\ 0 & 0 & [R] & 0 \\ 0 & 0 & 0 & [R] \end{bmatrix} \tag{C.18}$$

Where $[R]$ is a 3×3 matrix that can be described in two different ways, dependent on whether the incremental formulation or the total formulation is used. The incremental formulation assumes the rotation of each time step can be described linearly, which will be true with sufficiently small time steps. These incremental rotations are used to redefine two of the three unit vectors, as shown in eq. (C.19)

$$\begin{bmatrix} n_y & n_z \end{bmatrix} = \begin{bmatrix} n_y & n_z \end{bmatrix} \begin{bmatrix} cos(d\varphi_x^a) & -sin(d\varphi_x^a) \\ sin(d\varphi_x^a) & cos(d\varphi_x^a) \end{bmatrix} \tag{C.19}$$

The advantage of this method is that it is simple to describe mathematically and that no knowledge of the accumulated nodal rotation is needed. However, having knowledge about the accumulated nodal rotation is essential in the total formulation. In the total formulation the accumulated nodal rotation is described through quaternions, which are updated through differentiation. The updated quaternions describe the mean rotation of each element $(r, \mathbf{r})$ as well as the difference between the mean rotation and the rotation of each element end. The mean rotation is then used in an initial step to redefine the three unit vectors, as seen in (C.20)

$$\begin{bmatrix} n_x & n_y & n_z \end{bmatrix} = R(r, \mathbf{r}) \begin{bmatrix} n_x^0 & n_y^0 & n_z^0 \end{bmatrix} \tag{C.20}$$

After the unit vectors have been redefined, both formulations use the same method to find R, which is done with the help of the unit vectors n and $\Delta x/L$. n can be seen calculated

through the following equation, and $\Delta x/L$ is the unit vector n_x which has the smallest angle to the element.

$$\mathbf{n} = n_x + \Delta x/L \tag{C.21}$$

Now the R can be found [32]

$$R = (I - 2\mathbf{n}\mathbf{n}^T)\begin{bmatrix} -n_x & n_y & n_z \end{bmatrix} \tag{C.22}$$

C.1.3 Consistent mass

The mass in the corotational beam theory is the same as regular beam theories consistent mass. It is obtained by integrating the deformation matrix, which contains the shape functions.

$$[M] = \int_0^L [N]^T [N] \rho A dx \tag{C.23}$$

This is then rotated and assembled to the global mass matrix like the stiffness matrix. [16]

C.2 Non-linear Newmark integration

As for the linear Newmark beta-method, the non-linear Newmark integration is an implicit method, where the motion of the beam elements are calculated through the mass $[M]$, stiffness $[K]$, and damping $[C]$, the degrees of forward weighting (β, γ), and the forces acting on the beam. Because the non-linear effects are deformation related it is preferable to find the initial deformation through the equation of motion, and make predictions of the initial acceleration and velocities. Since the equation of motion is satisfied in the time increments, the forces on the beam elements can be found through.

$$f_{n+1} = [M]\ddot{u}_{n+1} + g(u_{n+1}, \dot{u}_{n+1}) \tag{C.24}$$

Where $[M]\ddot{u}_{n+1}$ represents inertia forces, and $g(u_{n+1}, \dot{u}_{n+1})$ is an expression for the internal forces. These are all the forces present in the non-linear motion equations, however to solve these non-linear equations the Newton-Raphson's iterative linear approximation method is used.

C.2.1 Newton-Raphson method

When encountering non-linear dynamics, it is in many cases appropriate to consider an iterative linear approximation. Such an approximation can be obtained using the Newton-Raphson method. It works by applying the desired loads incrementally, and solves the equilibrium equations in each iteration, which can be done by using a linearized set of equations as seen on Figure C.3.

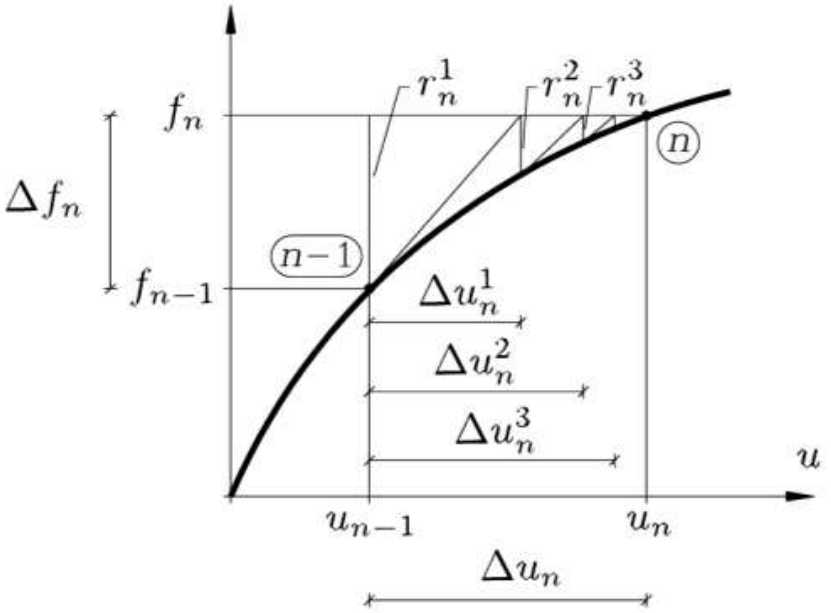

Figure C.3: Illustration of the approximation method used in the Newton-Raphson method. [32]

The linear approximation of the force results in a deviation in the force compared to the deformation, and this deviation is called the residual force.

$$r = f_{n+1} - [M]\ddot{u}_{n+1} - g(u_{n+1}, \dot{u}_{n+1}) \tag{C.25}$$

In each iteration it becomes smaller until a limit is reached and the iterations stop.
There are different versions of the Newton-Raphson method, but common problems are numerical inefficiency and the risk of infinite iterations, even with a limit on the residual.

C.2.2 Determination of motion components

In each iteration the linear increment of the physical forces are found and this can be expressed through the derivative of the residual force.

$$\delta r = \frac{dr}{du}\delta u = \left(\frac{\partial r}{\partial u} + \frac{\gamma \Delta t}{\beta \Delta t^2}\frac{\partial r}{\partial \dot{u}} + \frac{1}{\beta \Delta t^2}\frac{\partial r}{\partial \ddot{u}}\right)\delta u \tag{C.26}$$

As seen in eq. (C.25) the residual force contains contributions from internal forces, which are related to the stiffness and the damping. This relation can be expressed in terms of the derivative of the residual force.

$$[K] = \frac{\partial g}{\partial u}, \qquad [C] = \frac{\partial g}{\partial \dot{u}} \tag{C.27}$$

Since the total derivative of the residual force with respect to the deformation is equal to the modified tangent stiffness matrix in the Newmark integration, this contribution can now be determined.

$$[K_{eff}] = -\frac{dr}{du} = [K] + \frac{\gamma}{\beta\Delta t}[C] + \frac{1}{\beta\Delta t^2}[M] \tag{C.28}$$

This iterative determination of the modified tangent stiffness matrix is necessary to determine the displacement increment in each iteration, which is done by rearranging eq. (C.26).

$$\delta u = [K_{eff}]^{-1}\delta r \tag{C.29}$$

With the displacement increment determined, new motion component can be calculated through eq. (C.30) - (C.32)

$$u_{n+1} = u_{n+1} + \delta u \tag{C.30}$$

$$\dot{u}_{n+1} = \dot{u}_{n+1} + \frac{\gamma}{\beta\Delta t}\delta u \tag{C.31}$$

$$\ddot{u}_{n+1} = \ddot{u}_{n+1} + \frac{1}{\beta\Delta t^2}\delta u \tag{C.32}$$

These are the new motion components to be used in the next time step, unless the residual is determined to be too large. Then the new motion components are used to again in equation C.25 in a new Newton-Raphson iteration until a sufficiently small residual is achieved.

C.2.3 Step-by-step summery of the non-linear Newmark intergraion process

1. Determine initial conditions $(u_0, \dot{u}_0, \ddot{u}_0)$ using the motion equation.
2. Formulate prediction steps $(u_{n+1}, \dot{u}_{n+1}, \ddot{u}_{n+1})$
3. Estimate the residual from eq. (C.25)
4. Determine the modified tangent stiffness matrix using eq. (C.28)
5. Calculate the displacement increment with eq. (C.29)
6. With the displacement increment, new motion components can be defined through eq. (C.30) - (C.32)
7. Evaluate the new residual and deformation increment. If they are beyond their limits, start a new iteration with the same forces. If they are within their limits, proceed to the next time step. [32]

D
Appendix

This appendix contains the validation of the corotational beam formulation, the Newmark-integration, and the Newton-Raphson method used for iterative approximation.

D.1 Validation of large rotations in the corotational beam formulation

The ability to handle large rotations is demonstrated through the following example concerning roll-up of a cantilever beam. [32]

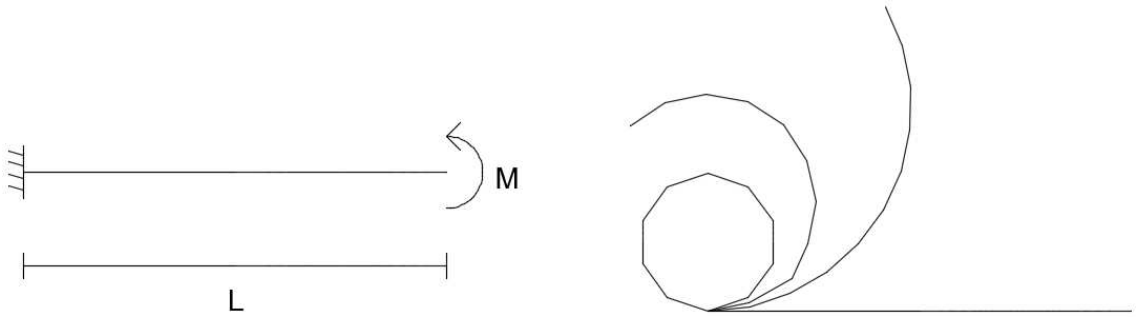

Figure D.1: Roll-up of a cantilever beam.

The point of the example is that a cantilever beam with a constant moment at the end will have a curvature of:

$$\kappa = \frac{1}{R} = \frac{M}{EI} \tag{D.1}$$

Meaning that the beam end will have rotated 360° in such a way that it resembles a polygon with the two beam ends meeting as seen on Figure D.1, when the moment is equal to:

$$M = \frac{2\pi EI}{L} \tag{D.2}$$

Since the applied moment is dependent on the beam dimensions and properties, the same result should be achieved every time, however only beam theories which can handle large rotations will be able to model such a phenomenon. A model, consisting of 10 elements, was made both in SOFIA and in ANSYS Workbench. The result can be seen on Figure D.2.
It can be seen that the result from SOFIA seems to be correct, and the example show that SOFIA is capable of handling large rotations. It should however be noted that the

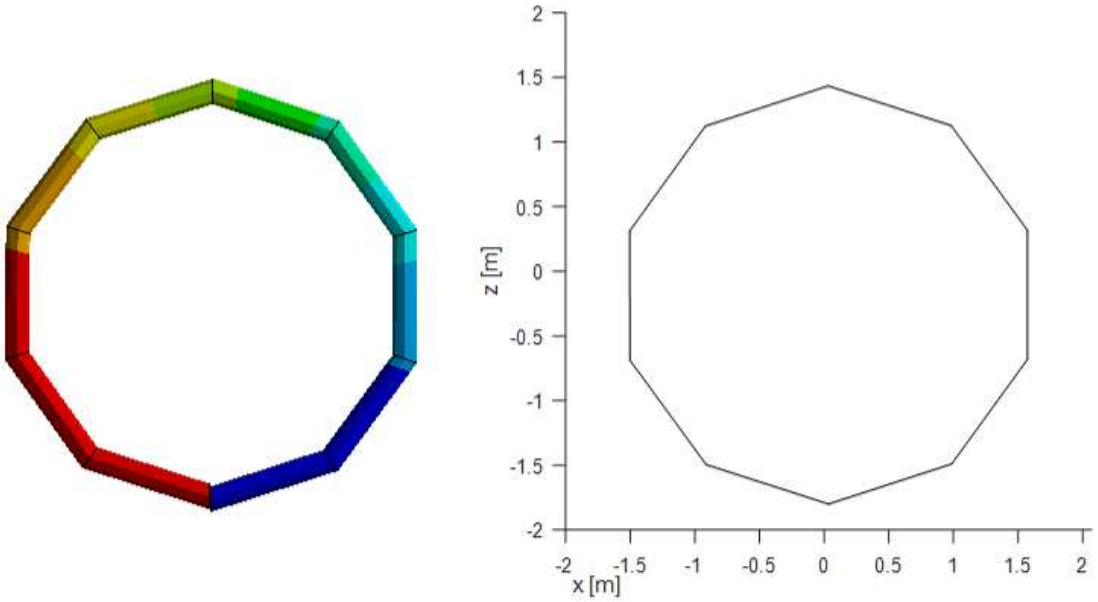

Figure D.2: Result from numeric analysis of roll-up of cantilever beam. Left is from ANSYS Workbench and right is from SOFIA.

example require a static solving method, which is approximated in SOFIA dynamic solver by incrementally increasing the moment over a sufficient amount of time so the dynamic effects are neglected. As for the ANSYS solution it is solved by a static solver, but does not quite reach the correct result.

D.2 Validation of large deformations and the geometric stiffness in the corotational beam formulation

The ability to handle large deformations is illustrated in the following example. [32]

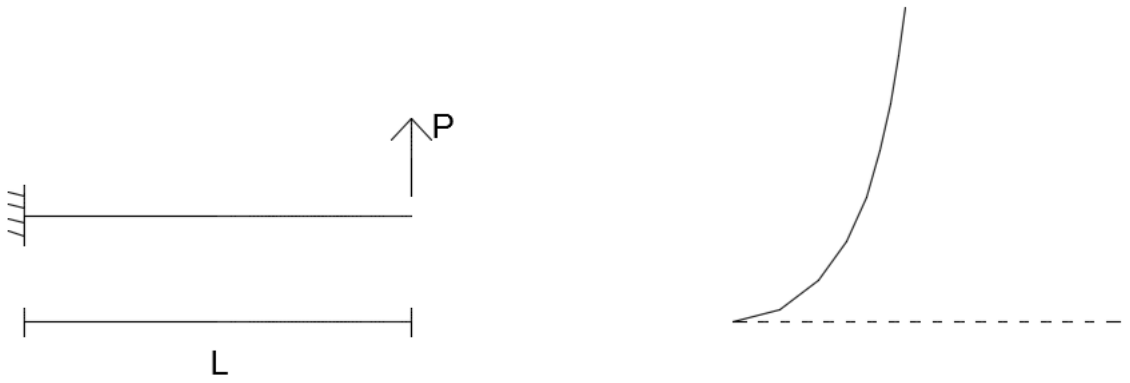

Figure D.3: Large deformation of a cantilever beam.

Where the force is equal to:

$$P = \frac{10EI}{L^2} \tag{D.3}$$

If the beam theory is correct then the vertical deformation over the length u/L should be approximate -0.555, the horizontal deformation over the length v/L approximate 0.81061 and the rotation at the end from the initial position Φ approximate 1.43029 rad. In

the case that the geometric stiffness is omitted, convergence would fail around half the specified load. The results from ANSYS Workbench and SOFIA can be seen in Table D.1.

Table D.1: Dimensionless vertical and horizontal deformation, and rotation at beam end in ANSYS Workbench.

Number of elements	-u/L	v/L	Φ[rad]
2	0.55275	0.80870	1.4263
4	0.55534	0.81109	1.4304
6	0.55553	0.81133	1.4306
8	0.55556	0.81136	1.4306
300	0.55558	0.81136	1.4307

Table D.2: Dimensionless vertical and horizontal deformation, and rotation at beam end in SOFIA.

Number of elements	-u/L	v/L	Φ[rad]
2	0.56762	0.84806	1.4777
4	0.55572	0.81910	1.4405
6	0.55506	0.81432	1.4347
8	0.55498	0.81278	1.4328
300	0.55499	0.81093	1.4304

The table shows that SOFIA is almost exact with 300 elements, with the solution becoming ever more precise with a larger number of elements. This is however not the case for the solution in ANSYS Workbench.

D.3 Validation of the Newmark-integration, rigid body motions, and the ocean environment

To validate the time integration method, the use of rigid body motions and the ocean environment set up in SOFIA, a free floating beam system is analyzed. Free floating means that no restraints of the DOF are used and displacements can go towards infinity. The beam system is 30 meter long with a circular cross section with radius 6000 mm. A figure of the beam system can be seen on Figure D.4.

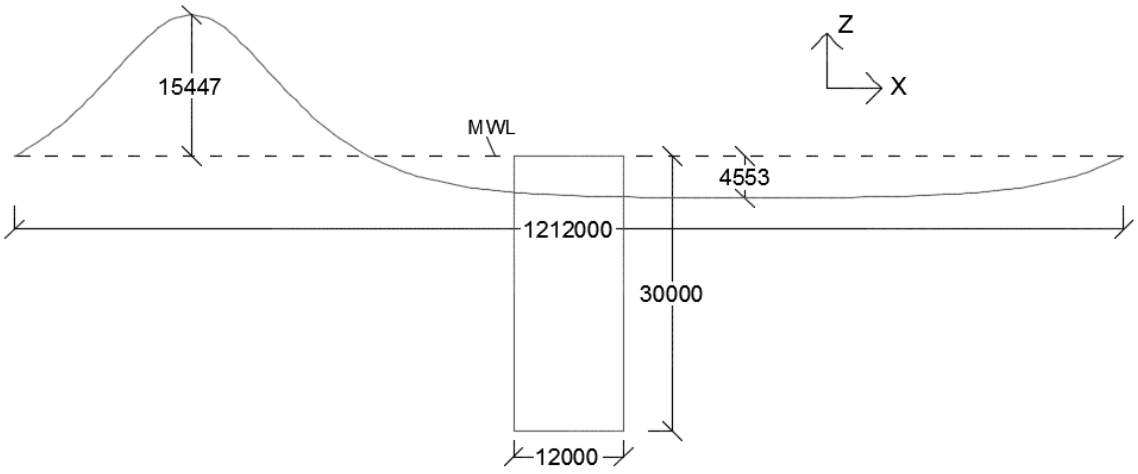

Figure D.4: Validation model in mm. Note that the wave length is 1,012 km, which for the sake of illustration has been reduced 1:10.

D.3.1 Program settings

To simulate the waves and the current working on the structure in ANSYS, the add-on *Ocean Environment* was used. To make sure almost every wave scenario can be analyzed the stream function is used, and the forces on the beam system is found through Morison's equation. Table D.3 shows the settings necessary in the numerical analyzes.

Table D.3: Ocean settings in ANSYS Workbench and SOFIA.

Parameter	**Value**
Wave height	20 m
Initial wave height	20 m
Peak period	40 s
Mean wave direction (x-direction)	0°
Current velocity $\left[horizontal, \quad vertical\right]$	$\left[0.2\frac{m}{s}, \quad 0\right]$
Current direction	90°
Water depth	60 m
Stream function order	10
Initializing error	1
Tolerance	10^{-5}
Added mass coefficient	1
Buoyancy force ratio	1
Normal drag coefficient	1
Tangential drag coefficient	1
Inertia mass coefficient	2
Vertical direction	z
Number of extraction points along elements	1
Acceleration limit	50 $\frac{m}{s^2}$
Ramping	0

The dimensions of the beam system and the ocean environment result yields a Keulegan-Carpenter number of approximately 23, meaning drag and inertia forces are equally rep-

resented.
The solving method being used is the Newmark beta-method, which requires the following parameters to be determined.

Table D.4: Newmark solver settings in ANSYS Workbench and SOFIA.

Parameter	**Value**
Mass proportional damping coefficient	0
Stiffness proportional coefficient	0
Numerical damping coefficient	0.01
Newmark beta-method integration parameter (γ)	0.51
Newmark beta-method integration parameter (β)	0.255025
Initial displacement	0
Initial velocity	0
Time step	0.01

SOFIA is only capable of analyzing isotropic material, and the reference material used is steel.

Table D.5: Material settings in ANSYS Workbench and SOFIA.

Parameter	**Value**
Young's modulus	$2 \cdot 10^{11} Pa$
Poisson's ratio	0.3
Shear modulus	$7.6923 \cdot 10^{10} Pa$
Density	$1027 \ \frac{kg}{m^3}$
Timoshenko shear coefficients	0
Number of element divisions	30

D.3.2 Results

The result of the analyzes can be seen on Figure D.5 to Figure D.10.

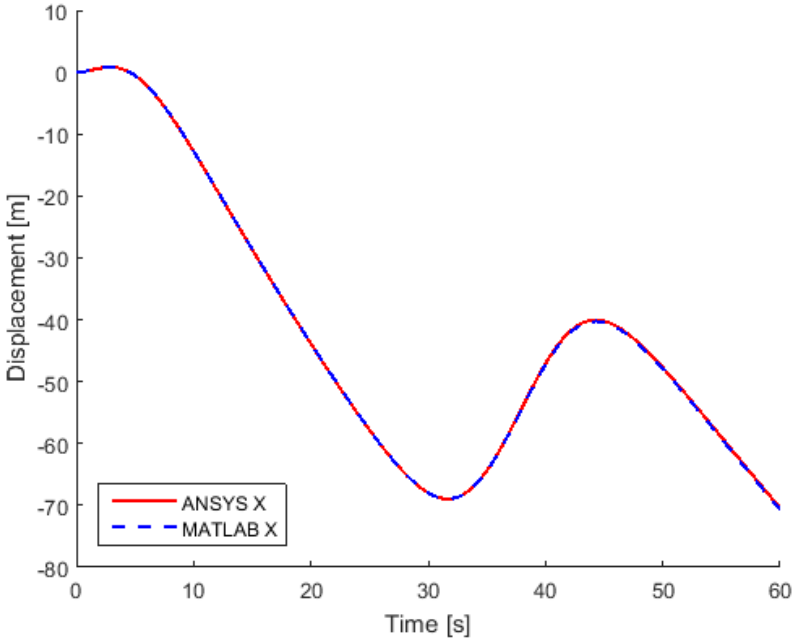

Figure D.5: Horizontal x-directional displacements (surge) modeled in both ANSYS and SOFIA.

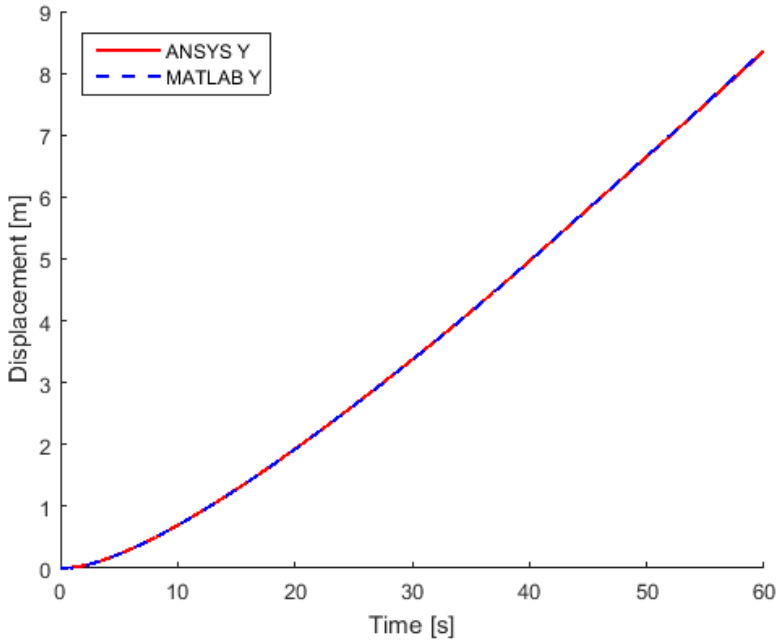

Figure D.6: Horizontal y-directional displacements (sway) modeled in both ANSYS and SOFIA.

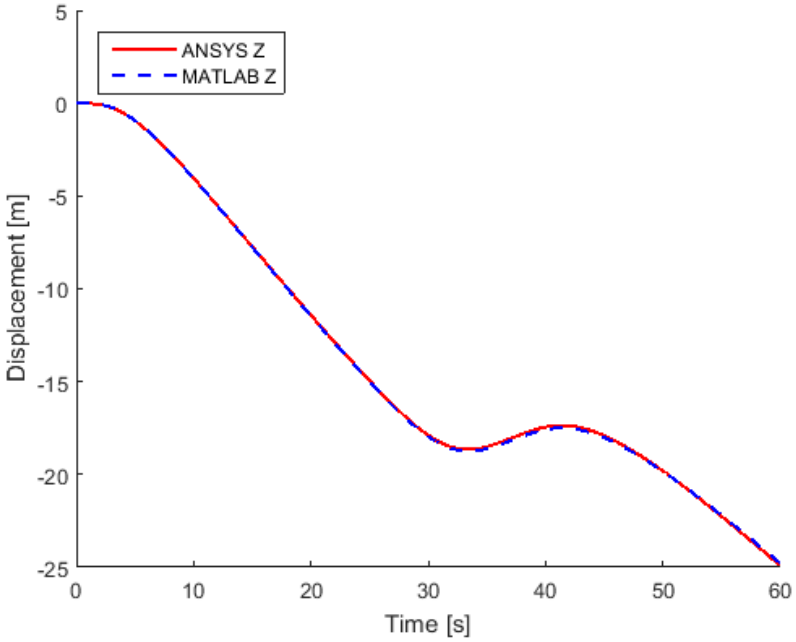

Figure D.7: Vertical z-directional displacements (heave) modeled in both ANSYS and SOFIA.

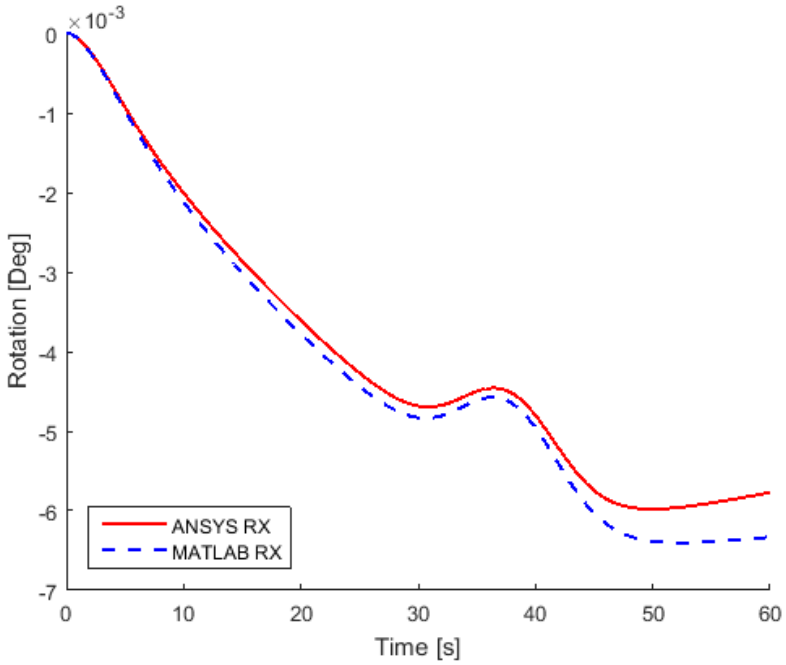

Figure D.8: Rotation about the x-axis (pitch) modeled in both ANSYS and SOFIA.

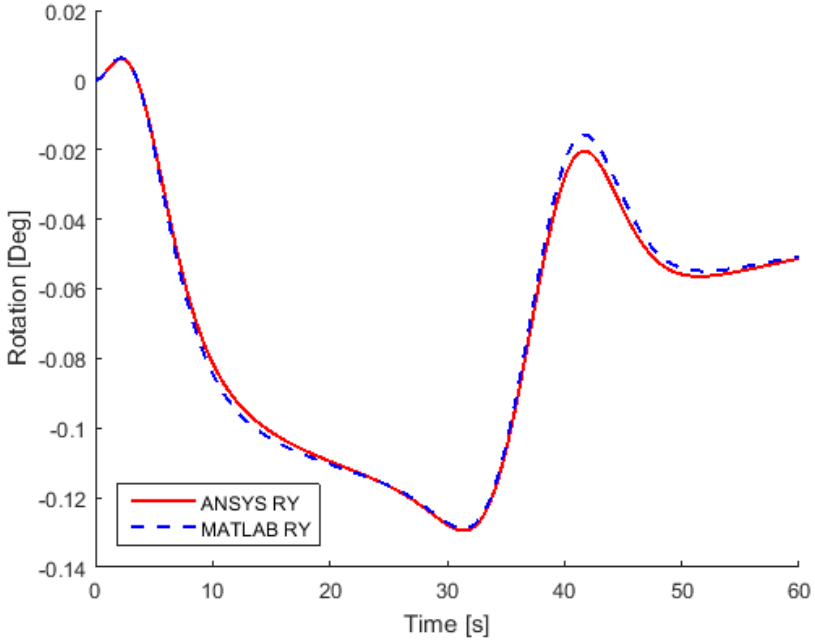

Figure D.9: Rotation about the y-axis (roll) modeled in both ANSYS and SOFIA.

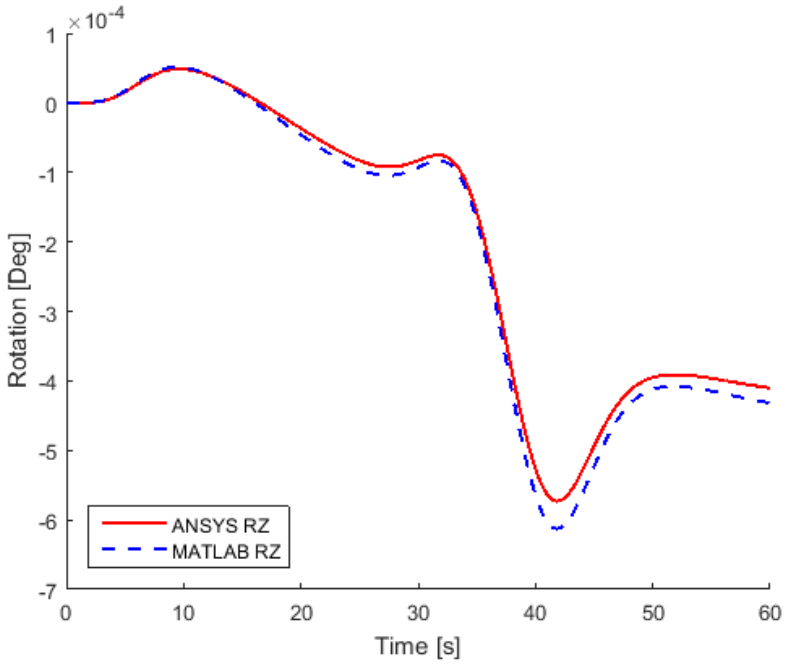

Figure D.10: Rotation about the z-axis (yaw) modeled in both ANSYS and SOFIA.

As seen in the figures, the results from SOFIA are nearly exactly the same as found in ANSYS. Only the rotations deviate a little, which may be because the rotations are so small.

D.4 Validation of submerged mooring line and tube models using corotational beam elements

With the beam theory validated, the application of the theory in different geometric configurations should be investigated, such as the ability to model mooring lines and tubes. Mooring lines, like bars, lack the ability to withstand bending, and in addition mooring lines cannot withstand compression. Tubes are like beams, however whether the elements flood with water must be taken into consideration. In order to validate SOFIAs ability to model such configurations, a simulation of the configuration seen in Figure D.11 was made in both ANSYS and SOFIA

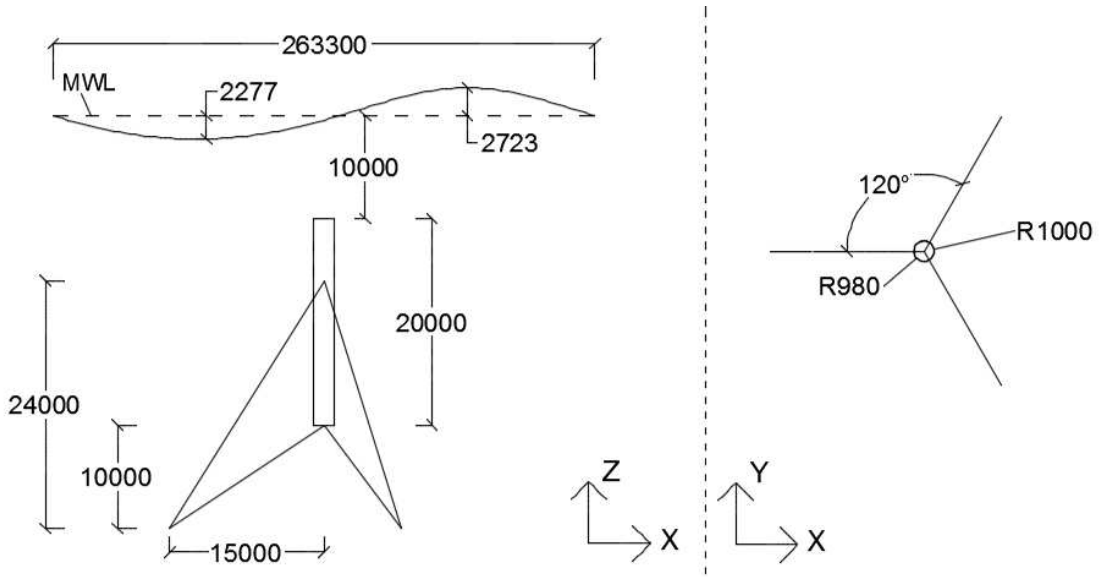

Figure D.11: Validation model in mm. Note that the wave length is 263.3 m, which for the sake of illustration has been reduced 1:5.

For ANSYS to model mooring lines, an APDL command is used. The command is written as followed.

ET,*Element Number*,LINK180
SECTYPE,*Element Number*,LINK
SECDATA,*Cross Section Areal*

LINK180 is a reference to a bar element, which has implemented stress stiffening and large deflection effects, which makes it similar to the corotational beam elements used in SOFIA. It also has the ability to only withstand tension or compression, however this function is not used, since such a feature is not included in SOFIA.

To simulate a mooring line in SOFIA, the usual corotational beam elements are used, except that the moment of inertia about the cross sectional plane is set to be zero.

Tubes are made in ANSYS the same way beams are made, except a hollow circular cross section is used, instead of a solid cross section, and the *Line Body Model Type* is set to *Pipe* instead of *Beam*. This cause ANSYS to use the PIPE288 element, which is a Timoshenko beam element, which include shear deformation, stress stiffening, and large deflection ef-

fects, as does the corotational beam elements in SOFIA. It is best suited for slender to moderately thick pipe structures, which means it is well suited for offshore structures. In combination with the ANSYS add-on *Ocean Environment* this element also has the ability to be flooded, however this function is not used in this validation.

In SOFIA, tubes are made by using a hollow cross section. The flooding ability is not implemented in the program.

In both program the mooring lines and tubes are not connected by sharing the same DOF in a node, since this is not the conventional way to make mooring line supported structures. Instead the rotational DOF are kept independent in the node. In ANSYS this is done by separating the *Line Bodies* using the *Slice* function, and then connecting them again using a *spherical body-body connection*. In SOFIA it is done by adding the 3 DOF to the system, using the matrix named *HiElem*. The 3 added DOF represents rotations in a node of the element chosen, which in this case is the element belonging to the mooring line, which become independent of the rotations in any element it is connected to.

D.4.1 Program settings

As with the free floating cylinder the add-on *Ocean Environment* was used in ANSYS. The stream function is used to simulate waves, and the forces on the beam system is found through Morison's equation. Table D.6 shows the settings necessary in the numerical analyzes.

Table D.6: Ocean settings in ANSYS Workbench and SOFIA.

Parameter	**Value**					
Wave height	5 m					
Initial wave height	5 m					
Peak period	15 s					
Mean wave direction (x-direction)	0°					
Current velocity $[horizontal, \quad vertical]$	$[0, \quad 0]$					
Water depth	40 m					
Stream function order	5					
Initializing error	1					
Tolerance	10^{-5}					
Added mass coefficient	1					
Buoyancy force ratio	1					
Normal drag coefficient	1					
Tangential drag coefficient	1					
Inertia mass coefficient	2					
Vertical direction	z					
Number of extraction points along elements	1					
Acceleration limit	1 $\frac{m}{s^2}$					
Ramping (SOFIA)	0					
Ramping (ANSYS)	Δt	$1s$	$1s$	$1s$	$1s$	$41s$
	H	$0.1m$	$1m$	$2m$	$3.5m$	$5m$

The dimensions of the beam system and the ocean environment result yields a Keulegan-

Carpenter number of approximately 12, meaning drag and inertia forces are equally represented.
The solving method being used is the Newmark beta-method, which requires the following parameters to be determined.

Table D.7: Newmark solver settings in ANSYS Workbench and SOFIA.

Parameter	**Value**
Mass proportional damping coefficient	0
Stiffness proportional coefficient	0
Numerical damping coefficient	0.1
Newmark beta-method integration parameter (γ)	0.6
Newmark beta-method integration parameter (β)	0.3025
Initial displacement	0
Initial velocity	0
Time step (SOFIA)	0.0015
Time step (ANSYS)	0.01

SOFIA is only capable of analyzing isotropic material, and the reference material used is steel for both tube and mooring lines. However due to instability problems the density of the mooring lines are lowered.

Table D.8: Material settings in ANSYS Workbench and SOFIA.

Parameter	**Value**
Young's modulus	$2 \cdot 10^{11} Pa$
Poisson's ratio	0.3
Shear modulus	$7.6923 \cdot 10^{10} Pa$
Tube density	7850 $\frac{kg}{m^3}$
Mooring line density	1200 $\frac{kg}{m^3}$
Timoshenko shear coefficients	0
Number of element divisions (Tube)	30
Number of element divisions (Mooring lines)	20

D.4.2 Results

The result of the analyzes can be seen on Figure D.12 to Figure D.17.

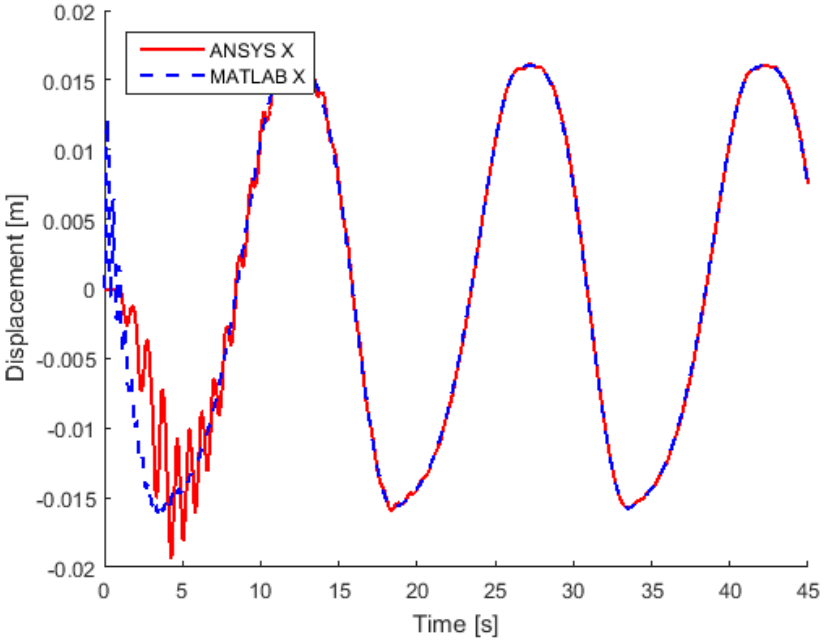

Figure D.12: Horizontal x-directional displacements (surge) modeled in both ANSYS and SOFIA.

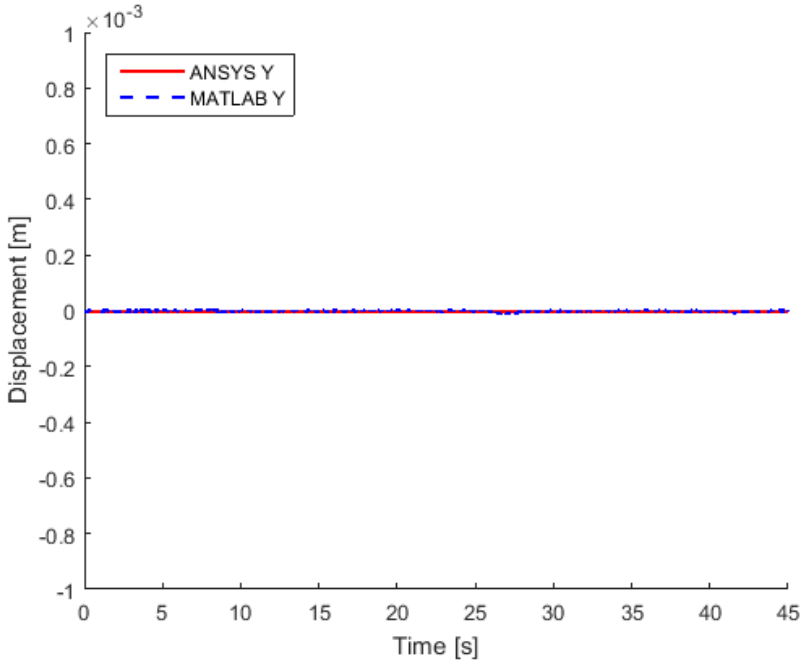

Figure D.13: Horizontal y-directional displacements (sway) modeled in both ANSYS and SOFIA.

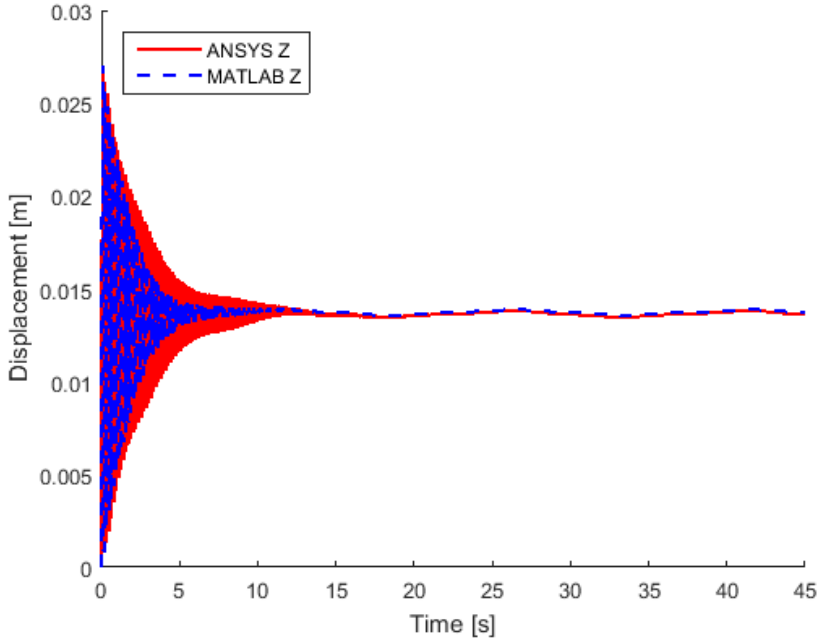

Figure D.14: Vertical z-directional displacements (heave) modeled in both ANSYS and SOFIA.

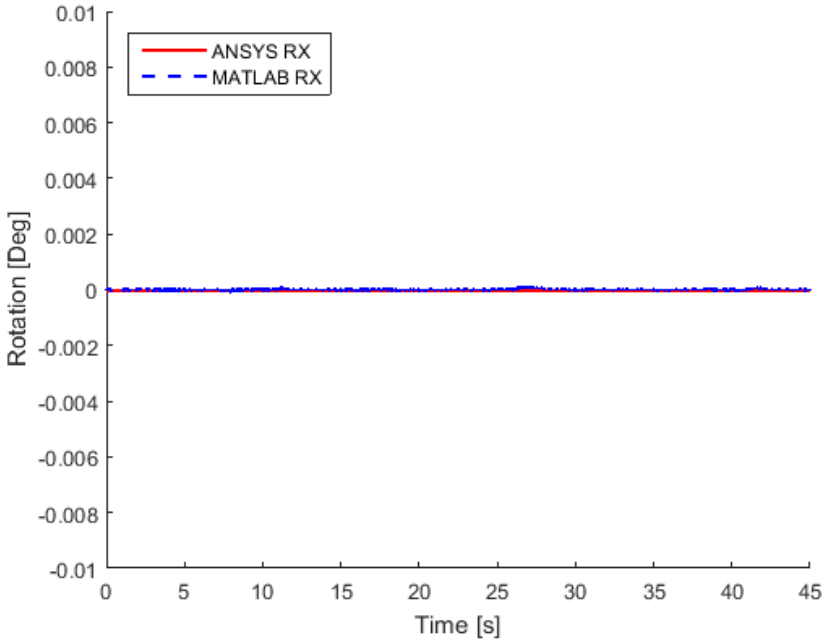

Figure D.15: Rotation about the x-axis (pitch) modeled in both ANSYS and SOFIA.

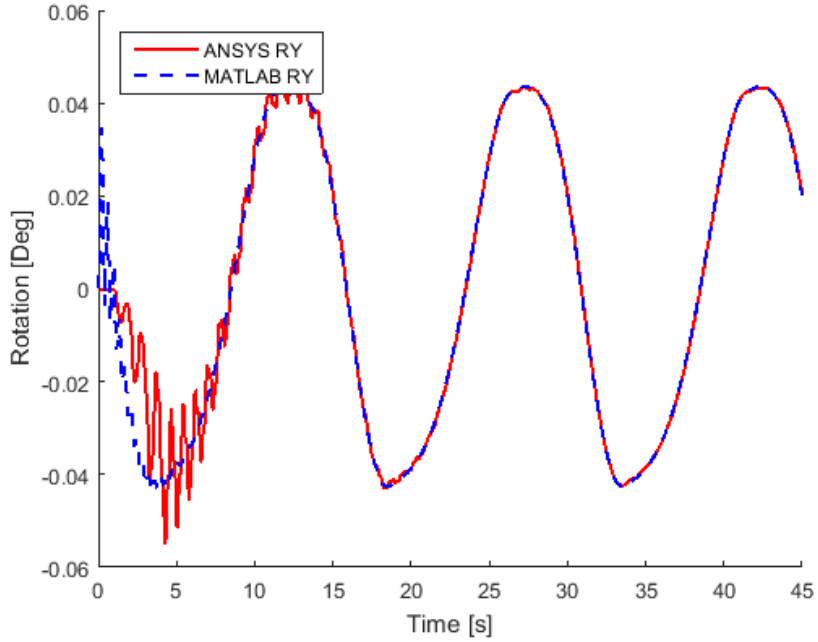

Figure D.16: Rotation about the y-axis (roll) modeled in both ANSYS and SOFIA.

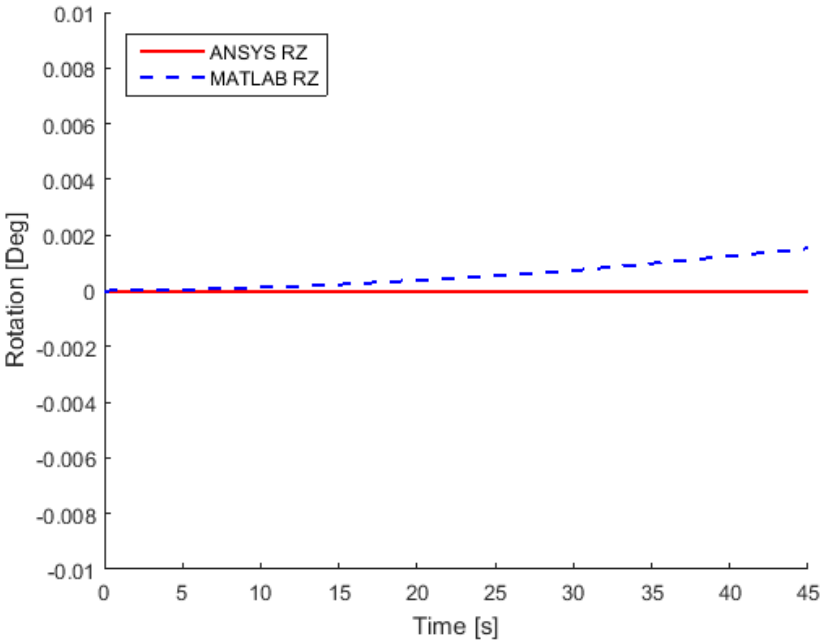

Figure D.17: Rotation about the z-axis (yaw) modeled in both ANSYS and SOFIA.

As seen in the figures, the results from the MATLAB code are nearly exactly the same as found in ANSYS. Only yaw deviate a little, however this may again be because the rotations are so small.